Li, Zhibo (2015) *Plasmonic nano apertures for molecular sensing and colour displays.* PhD thesis.

http://theses.gla.ac.uk/6986/

Copyright and moral rights for this thesis are retained by the author

A copy can be downloaded for personal non-commercial research or study

This thesis cannot be reproduced or quoted extensively from without first obtaining permission in writing from the Author

The content must not be changed in any way or sold commercially in any format or medium without the formal permission of the Author

When referring to this work, full bibliographic details including the author, title, awarding institution and date of the thesis must be given

Glasgow Theses Service
http://theses.gla.ac.uk/
theses@gla.ac.uk

Plasmonic Nano Apertures for Molecular Sensing and Colour Displays

Zhibo Li

A Thesis submitted to

School of Engineering

University of Glasgow

In fulfilment of the requirements for the degree of

Doctor of Philosophy (Ph.D)

September 2015

Abstract

The discovery of extraordinary optical transmissions through metallic periodical subwavelength apertures has seen promising applications in filtering and sensing. Such a unique optical property is due to the excitation of surface plasmon resonance. Through accurate control of the aperture's geometrical shape and dimension, the optical resonance of such nanostructure can be tuned in a wide range from the visible to near infrared. In addition, the highly confined resonant electromagnetic field supported by such a nanostructure can be utilised in surface enhanced Raman spectroscopy.

This thesis studied metallic nano aperture arrays for the application of molecular sensing and colour displays. The development of nanofabrication processes for making complex metallic nano apertures was the foundation of this research. Gold was chosen as the appropriate material for sensing mainly due to its stable chemical and physical properties. Aluminium was selected for making colour pixels because its optical resonant frequency can be tuned over the whole visible range.

One aspect of this research relating to surface enhanced Raman spectroscopy considered symmetrical gold nano apertures: annular aperture arrays and circular aperture arrays. Comparisons between two annular aperture arrays and between one annular aperture array and one circular aperture array were carried out. The asymmetrical gold nanostructures studied were split-ring shaped aperture arrays. One structure can be used to generate two polarisation dependent resonances in which one of them was able to match the laser in the Raman spectrometer for molecular interrogation and the other was not. The other aspect related to dual-colour pixels. Aluminium cross-shaped aperture arrays were fabricated. By varying the structural dimensions and incident polarisation, colours could be tuned over the whole visible range. Polarisation controlled chromatic displays were demonstrated by employing these pixels.

Publications

Journal Papers

Zhibo Li, Alasdair W. Clark, Jonathan M. Cooper, "Annular nanoplasmonic void arrays as tunable surface enhanced Raman spectroscopy substrates", Applied Physics Letters, 105(3), 033115, 2014.

Zhibo Li, Alasdair W. Clark, Jonathan M. Cooper, "Dual Colour Plasmonic Pixels Create a Polarisation Controlled Nano Colour Palette", ACS Nano, 10.1021/acsnano.5b05411, 2015.

Conference Papers

Zhibo Li, Alasdair W. Clark, Jonathan M. Cooper, "Annular Nanoplasmonic Void Arrays as Programmable Molecular Sensors", Photon14, London, 2014.

Zhibo Li, Jonathan M. Cooper, Alasdair W. Clark, "Dual-colour Nano-Pixels for image switching beyond the diffraction limit", The European Conference on Lasers and Electro-Optics (CLEO/Europe), Munich, 2015.

Alasdair W. Clark, Esmaeil Heydari, Zhibo Li, Jonathan M. Cooper, "Polarization switchable two-color plasmonic nano-pixels for creating optical surfaces encoded with dual information states", SPIE Photonics West, San Francisco, 2016.

Poster

Zhibo Li, Alasdair W. Clark, Jonathan M. Cooper, "Annular Nanoplasmonic Void Arrays for Surface Enhanced Raman Spectroscopy", SU2P Photonic Sensing the Environment, Glasgow, 2014.

Contents

List of Figures

Acknowledgement

First and foremost, I would like to thank my supervisor, Prof. Jon Cooper, for giving me the opportunity to carry out an exciting and challenging research project in his interdisciplinary group and for being a constant source of inspiration and enthusiasm toward the research. Many thanks also go to my second supervisor, Dr. Alasdair Clark. He gave me initial experimental trainings on my research and numerous helpful comments on my scientific writings. His insightful guidance and continuous support ensured a successful completion of my studies. Also, I want to give my thanks to all the lovely members in the Biomedical Engineering Group.

I would like to extend my appreciation to Dr. Haiping Zhou, Dr. Lianping Hou, and Dr. Ying Ding for their assistance and discussions on device fabrication and characterisation issues.

My sincere gratitude also goes to all the staff in the James Watt Nanofabrication Centre. Without their dedications in operating and maintaining the facilities, my research would have been impossible to be completed.

My deepest thanks also go to my friend Bruce MacKenzie and his family. I would also like to acknowledge China Scholarship Council (CSC) for the financial support to my studies.

Finally, I would like to express my special thanks to my parents and relatives. Their love, support and encouragement give me strength to overcome the difficulties during my studies.

Author's Declaration

The research presented in this thesis is the result of the author's own work and has not been submitted for any other degree at the University of Glasgow or any other institution.

Chapter 1 - Introduction and Theory

Abstract

This chapter describes the theoretical basis for the light-metal interactions which underpin the technology described in this thesis, namely, localized surface plasmon resonance (LSPR), surface plasmon resonance (SPR), and the extraordinary optical transmission through periodical metallic nano-apertures. The applications of such nanostructures related to the research in this thesis are presented, followed by theoretical descriptions of the Raman scattering process and surface enhanced Raman spectroscopy. A brief introduction to the research chapters of this thesis is also presented.

1.1 Interaction of light with metal at the nanoscale

When an electromagnetic wave interacts with bulk metal, its frequency determines the response from the metal. At lower frequencies, such as microwave and radio wave ranges, metals are good conductors with real and fixed finite conductivity. Such properties enable metals to be used traditionally in various applications such as waveguides, resonators and antennas, because only a tiny proportion of the electromagnetic wave penetrates into the metal. At higher frequencies, such as the near-infrared and visible range, metals become a loss-medium and the corresponding dielectric constant becomes complex. Although energy dissipation becomes more and more significant with increasing field penetrations, metals are still highly reflective because the electron oscillations in the metal still keep the pace with the incident fields. [1] Some metals such as gold [2] and copper [3] exhibit specific colours because they can absorb certain colours due to the electronic interband transition at visible range. Finally, with the frequency increasing to the ultraviolent range, most metals become transparent because the electrons cannot give such a fast response toward the external field, and are thus unable to reflect it. [1, 4] The theoretical explanations of light-metal interactions at optical frequencies and the plasmonic effect are discussed in the following sections.

1.1.1 Dielectric functions of metal at optical frequencies

The light-metal interactions and dielectric functions of metal at optical frequencies can be studied based on the classical Maxwell's equations. These are four equations: firstly, Gauss's law for magnetism; secondly, Gauss's law; thirdly, the Faraday law of induction and fourthly, the Ampere circuital law. Maxwell's equations describe the reciprocal interactions between electric and magnetic fields by charges and currents. The macroscopic differential forms of the Maxwell equations in vacuum are given by:

$$\nabla \cdot \mathbf{B} = 0 \qquad \textbf{(1.1a)}$$

$$\nabla \cdot \mathbf{D} = \rho_{ext} \qquad \textbf{(1.1b)}$$

$$\nabla \times \mathbf{E} = -\frac{\partial \mathbf{B}}{\partial t} \qquad \textbf{(1.1c)}$$

$$\nabla \times \mathbf{H} = \mathbf{J}_{ext} + \frac{\partial \mathbf{B}}{\partial t} \qquad \textbf{(1.1d)}$$

where, **B** is the magnetic induction, **D** is the electric displacement, **E** is the electric field, **H** is the magnetic field, ρ_{ext} is the external or free charge density, and $\mathbf{J}_{ext}$ is the external or free current density. The total current density equals the external current density ($\mathbf{J}_{ext}$) plus the internal current density (**J**). [5, 6] For a linear and homogeneous medium, the electric displacement, magnetic induction and internal current density can be defined by the constitutive relations:

$$\mathbf{D} = \epsilon_0 \epsilon_r \mathbf{E} = \epsilon_0 \mathbf{E} + \mathbf{P} \qquad \textbf{(1.2)}$$

$$\mathbf{B} = \mu_0 \mu_r \mathbf{H} \qquad \textbf{(1.3)}$$

$$\mathbf{J} = \sigma \mathbf{E} \qquad \textbf{(1.4)}$$

where, **P** is polarisation, which describes the electric dipole moment per unit volume inside the materials, ε_0 and μ_0 are the electric permittivity and magnetic permeability of a vacuum, ε_r and μ_r are relative permittivity and permeability of

the material, and σ is the conductivity of the material. The relative permeability μ_r of non-magnetic metals is 1. [1, 6]

At optical frequencies, metals can be seen as plasmas which are comprised of free negative charged electrons and fixed positive charged atomic nuclei, which from a macroscopic point of view still maintain the electrically neutral state. When a harmonic external electric field $\mathbf{E}(t) = \mathbf{E_0}e^{-i\omega t}$ with frequency ω interacts with free electrons inside metal, it causes an electron oscillation $\mathbf{x}(t) = \mathbf{x_0}e^{-i\omega t}$ which has the same frequency as the incident electric field. The motion of one free electron is driven by the electric force:

$$m\frac{d^2\mathbf{x}}{d^2t} + m\frac{d\mathbf{x}}{dt}\frac{1}{\tau} = -e\mathbf{E} \qquad \textbf{(1.5)}$$

where, e is the electric charge, m is the effective mass of the electron, and τ is the relaxation time of the free electrons. Therefore, the electron oscillation **x** can be expressed in relation to **E** as:

$$\mathbf{x}(t) = \frac{e}{m(\omega^2 + i\omega\tau^{-1})}\mathbf{E}(t) \qquad \textbf{(1.6)}$$

As a consequence of the displacement of the electrons, the macroscopic polarisation can be expressed as $\mathbf{P} = -ne\mathbf{x}$, which is:

$$\mathbf{P} = -\frac{ne^2}{m(\omega^2 + i\omega\tau^{-1})}\mathbf{E} \qquad \textbf{(1.7)}$$

where, n is the number of electrons. Substituting **equation (1.7)** into **equation (1.2)** yields the electric displacement:

$$\mathbf{D}=\epsilon_0\left(1 - \frac{ne^2}{\varepsilon_0 m(\omega^2 + i\omega\tau^{-1})}\right)\mathbf{E} \qquad \textbf{(1.8)}$$

Identifying plasma frequency of free electrons as $\omega_p^2 = \frac{ne^2}{\varepsilon_0 m}$ and comparing equation **(1.8)** with **equation (1.2)**, the relative permittivity of metal can be rewritten as:

$$\varepsilon_r = 1 - \frac{\omega_p^2}{\omega^2 + i\omega\tau^{-1}} \quad \textbf{(1.9)}$$

It shows that the relative permittivity of metal at optical frequencies becomes the complex form $\varepsilon_r = \varepsilon_1 + i\epsilon_2$, and the real and imaginary parts can be written as:

$$\varepsilon_1 = 1 - \frac{\omega_p^2\tau^2}{1 + \omega^2\tau^2} \quad \textbf{(1.10a)}$$

$$\varepsilon_2 = \frac{\omega_p^2\tau^2}{\omega(1 + \omega^2\tau^2)} \quad \textbf{(1.10b)}$$

where, ε_1 describes the polarisation of the metal by the external electric field, and ε_2 determines the energy losses in the metal due to absorption and ohmic losses. When ω approaches to ω_p, $\omega\tau >> 1$, **equation (1.9)** can be written as [1, 6]:

$$\varepsilon_r = 1 - \frac{\omega_p^2}{\omega^2} \quad \textbf{(1.11)}$$

To understand the dielectric response of the metal toward an external field with different frequencies, the condition of wave propagation in the medium needs to be explained first. The wave equations of a propagating wave are:

$$\nabla^2\mathbf{E} - \frac{\epsilon_r}{c^2}\frac{\partial^2\mathbf{E}}{\partial t^2} = 0 \quad \textbf{(1.12a)}$$

$$\nabla^2\mathbf{H} - \frac{\epsilon_r}{c^2}\frac{\partial^2\mathbf{H}}{\partial t^2} = 0 \quad \textbf{(1.12b)}$$

where, $c = \frac{1}{\sqrt{\varepsilon_0 \mu_0}}$ is the light speed in a vacuum. If the external field is a harmonic wave with $\mathbf{E}(t) = \mathbf{E_0} e^{-i\omega t}$, **equation (1.12a)** can be rewritten as:

$$\nabla^2 \mathbf{E} + k^2 \mathbf{E} = 0 \qquad \textbf{(1.13)}$$

where, k is defined as the wave vector of the propagating wave. The magnitude of wave vector describes the number of waves that exist per unit distance and its direction shows the direction of wave propagation. It can be expressed as:

$$k = \frac{2\pi}{\lambda} = \frac{\omega}{v} = \frac{\omega}{c}\sqrt{\epsilon_r} \qquad \textbf{(1.14)}$$

where, λ is the wavelength in the medium and v is the light speed in the medium. The wave vector of an electromagnetic wave in a vacuum is $k_0 = \frac{\omega}{c}$. [1, 6] For a dispersive medium, k exhibits frequency dependent features, thus the relation between k and ω is termed the dispersion relation. Inserting **equation (1.11)** into **equation (1.14)**, the wave vector of the propagating wave in the metal can be described as:

$$k(\omega) = \frac{1}{c}\sqrt{\omega^2 - \omega_p^2} \qquad \textbf{(1.15)}$$

If the frequency of incident field larger than ω_p, $k(\omega)$ approaches ω/c, which means the wave is able to propagate and penetrate through the metal, and at such frequencies, metal becomes transparent. If the incident frequency is lower than ω_p, $k(\omega)$ becomes imaginary, and this means that wave is prohibited from propagating through the metal. Only a small fraction of wave penetrates into the metal and decays exponentially. At such frequencies, metal becomes reflective. When the frequency ω equals ω_p, $k(\omega)$ is zero, it means the electromagnetic wave is cut off at this frequency and any wave with its frequency lower than the cut off frequency attenuates, rather than propagates. [1, 5, 6]

1.1.2 Plasmonics

Surface plasmons are charge density oscillations or surface electromagnetic resonances experienced at the interface between a dielectric and a conductor (normally metals) due to the coupling of an external electromagnetic field with free electron oscillation in the metals. The oscillation strength or resonance intensity attenuates rapidly away from the interface into the dielectric or metal region. [7] There are two fundamental forms of plasmon resonance: localized surface plasmon resonance (LSPR) and surface plasmon resonance (SPR). LSPR is the resonances at nanoscale metal structures and particles, where the dimensions of the particle are basically comparable or smaller than the excitation wavelength.[8] SPR, on the other hand, is a dispersive and propagating wave along the metal/dielectric interface of a bulk metal material, exhibiting evanescent decay perpendicular to this interface. [9, 10]

1.1.2.1 Localized surface plasmon resonance

When incident light interacts with a metallic nanoparticle, the oscillating electromagnetic field is able to penetrate into the nanoparticle and lead to collective oscillation of the free electrons in the conduction band of the metal. Therefore, the nanoparticle can be seen as an oscillating dipole in which electromagnetic resonance occurs. The displacement of the free electron generates a dipole momentum **P** in which the magnitude is proportional to the strength of the applied electromagnetic field **E**, with the relation $\mathbf{P} = \alpha\mathbf{E}$ Where α is defined as polarisability, which is used to describe how the nanoparticle is polarised by the external field, and can be written as: [1]

$$\alpha = 4\pi a^3 \frac{\varepsilon_d - \varepsilon_m}{\varepsilon_d + 2\varepsilon_m} \qquad \textbf{(1.16)}$$

where, a is the radius of the particle, ε_d is the dielectric constant of the surrounding medium, and ε_m is the complex dielectric function of the metal. **Figure 1.1** shows the schematic of free electron oscillation in presence of an electromagnetic wave. [11]

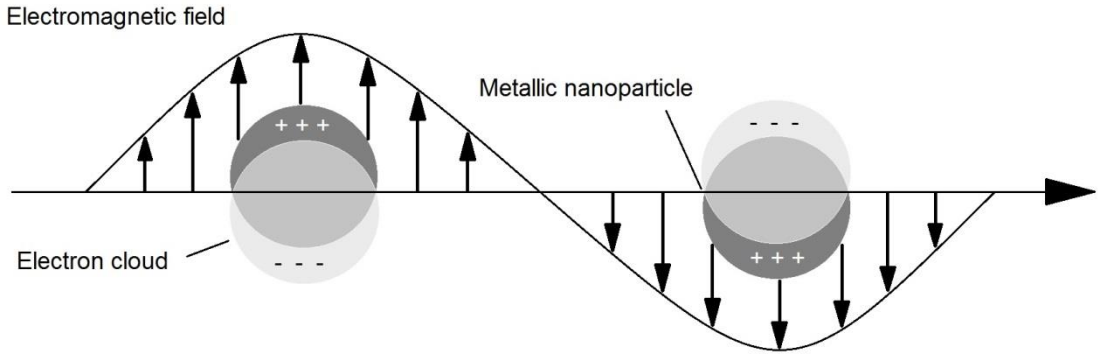

Figure 1.1, Schematic of interaction between metallic nanoparticle and external fields. Free electron displacement relative to nuclei is excited by an oscillating electromagnetic field.

The excited resonance is confined to the nanoparticle and results in strong light scattering and absorption as well as localized electromagnetic field enhancement. The resonance frequencies can be manipulated by varying the particle's shape and size, the surrounding medium, and by using different metals. [11] The LSPR of some noble metals (such as gold or silver) falls into the visible range and this optical property brings metallic nanoparticles composed of these materials real applications. For example, because of the various colours produced by colloidal gold or silver nanoparticles, ancient cultures have for centuries utilised those features for making stained glass and decorations. In addition, highly confined fields generated by the metallic nanoparticles have also been employed to enhance spectroscopy in areas such as fluorescence and Raman scattering in biosensing applications. [8, 12-15]

1.1.2.2 Surface plasmon resonance

A single flat metal/dielectric interface is the simplest geometry supporting surface plasmon resonance. **Figure 1.2** shows the diagram of a single interface between metal and a dielectric, where the SPR propagates along x-axis, the region $z>0$ represents the dielectric and the region $z<0$ represents the metal.

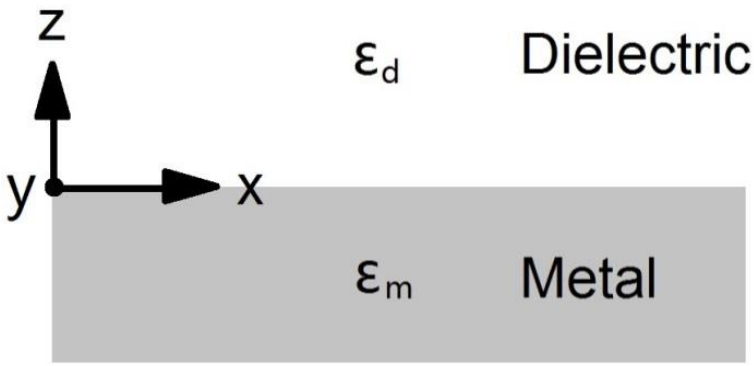

Figure 1.2, Diagram of the dielectric/metal interface in which the SPR propagates.

For a harmonic incident wave with TE (transverse electric) mode (s-polarisation), the electric component in y-axis E_y, the magnetic component in z-axis H_z and in the wave propagation direction x-axis H_x are nonzero. The corresponding TE wave equation can be described as:

$$\frac{\partial^2 E_y}{\partial z^2} + \left(k_0^2 \epsilon_0 \epsilon_r - k_x^2\right) E_y = 0 \qquad \textbf{(1.17)}$$

In the dielectric region where z>0:

$$E_y = E e^{i(k_x x - k_d z)} \qquad \textbf{(1.18a)}$$

$$H_x = -H \frac{k_d}{\omega \mu_0} e^{i(k_x x - k_d z)} \qquad \textbf{(1.18b)}$$

$$H_z = H \frac{k_x}{\omega \mu_0} e^{i(k_x x - k_d z)} \qquad \textbf{(1.18c)}$$

In the metal region where z<0:

$$E_y = E e^{i(k_x x + k_m z)} \qquad \textbf{(1.19a)}$$

$$H_x = H \frac{k_m}{\omega \mu_0} e^{i(k_x x + k_m z)} \qquad \textbf{(1.19b)}$$

$$H_z = H \frac{k_x}{\omega \mu_0} e^{i(k_x x + k_m z)} \qquad \textbf{(1.19c)}$$

Where, k_x is the wave vector in wave propagation along the x-axis, and k_d and k_m are the wave vectors along the z-axis in dielectric and metal regions respectively. To sustain the SPR propagating along the interface, the boundary condition requires the continuity of field components at the interface, thus resulting in:

$$E(k_m + k_d) = 0 \quad \textbf{(1.20)}$$

This condition can be satisfied only when electric field E=0, thus giving a zero magnetic field as well, therefore, the TE mode cannot exist in SPR.

Similarity, for a harmonic incident wave with TM (transverse magnetic) mode (p-polarisation), the magnetic component in y-axis H_y, the electric component in z-axis E_z and in the wave propagation direction x-axis E_x are nonzero. The corresponding TM wave equation can be described as:

$$\frac{\partial^2 H_y}{\partial z^2} + \left(k_0^2 \epsilon_0 \epsilon_r - k_x^2\right) H_y = 0 \quad \textbf{(1.21)}$$

In the dielectric region where z>0:

$$H_y = He^{i(k_x x - k_d z)} \quad \textbf{(1.22a)}$$

$$E_x = E\frac{k_d}{\omega \epsilon_0 \epsilon_d} e^{i(k_x x - k_d z)} \quad \textbf{(1.22b)}$$

$$E_z = -E\frac{k_x}{\omega \epsilon_0 \epsilon_d} e^{i(k_x x - k_d z)} \quad \textbf{(1.22c)}$$

In the metal region where z<0:

$$H_y = He^{i(k_x x + k_m z)} \quad \textbf{(1.23a)}$$

$$E_x = -E\frac{k_m}{\omega \epsilon_0 \epsilon_m} e^{i(k_x x + k_m z)} \quad \textbf{(1.23b)}$$

$$E_z = -E\frac{k_x}{\omega\epsilon_0\epsilon_m}e^{i(k_x x + k_m z)} \quad \textbf{(1.23c)}$$

To sustain the SPR propagating along the interface, the boundary condition requires the continuity of field components at the interface, thus giving the relationship of k_d and k_m in terms of ε_d and ε_m:

$$\frac{k_d}{k_m} = -\frac{\epsilon_d}{\epsilon_m} \quad \textbf{(1.24)}$$

Also, inserting the H_y expressions (at metal and dielectric regions) into the wave **equation (1.17)** yields:

$$k_d^2 = k_x^2 - k_0^2\epsilon_d \quad \textbf{(1.25a)}$$

$$k_m^2 = k_x^2 - k_0^2\epsilon_m \quad \textbf{(1.25b)}$$

Dividing **equation (1.25a)** by **equation (1.25b)** and using the relationship of k_d and k_m yields the wave vector of surface plasmon resonance:

$$k_{sp} = k_x = k_0\sqrt{\frac{\epsilon_d\epsilon_m}{\epsilon_d + \epsilon_m}} \quad \textbf{(1.26)}$$

Equation (1.26) has demonstrated that the resonance with TM mode is permitted to propagate along the metal/dielectric interface. Therefore, only TM mode can exist in surface plasmon resonance. [1, 16] If replacing ε_m in **equation (1.26)** by a frequency dependence expression as shown in **equation (1.11)**, this yields the dispersion relation of surface plasmon resonance as:

$$k_{sp} = k_0\sqrt{\frac{\omega_d(\omega^2 - \omega_p^2)}{(\omega_d + 1)\omega^2 - \omega_p^2}} \quad \textbf{(1.27)}$$

When the SPR frequency ω_{sp} approaches to $\omega_p/\sqrt{\varepsilon_d + 1}$, k_{sp} approaches infinity, and as ω_{sp} approaches to 0, k_{sp} approaches to $k_0\sqrt{\varepsilon_d}$, which is the so-called dielectric light line. **Figure 1.3** shows the dispersion relation of surface plasmon resonance with frequency ω_{sp} between 0 and $\omega_p/\sqrt{\varepsilon_d + 1}$.

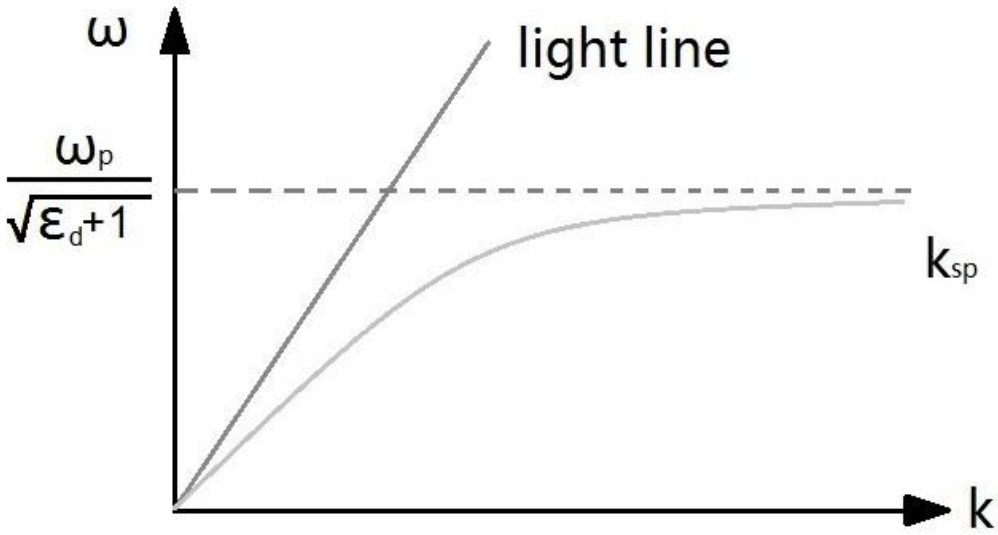

Figure 1.3, Dispersion curve of surface plasmon resonance. ω_p is the plasma frequency of the free electrons in the metal.

As can be seen from the SPR dispersion curve, for frequencies where $\omega_{sp} < \omega_p/\sqrt{\varepsilon_d + 1}$, the wave vector of light in the dielectric region is always smaller than the wave vector of SPR even at grazing incidence, thus preventing the momentum-matching between light and SPR, therefore, it's impossible to get SPR coupling just by shining a light toward the metal/dielectric interface. This coupling excitation of SPR can be achieved by a prism coupler. [1, 17] When the light propagates in the high refractive index prism, its wave vector can be expressed as:

$$k_{prism} = k\sqrt{\epsilon_{prism}}\ \sin\theta \qquad \textbf{(1.28)}$$

Where, k_{prism} is the wave vector at the metal interface, k is the wave vector of light in the prism, ε is the refractive index of the prism, and θ is the light incident angle. When the resonant condition (as **equation (1.28)**) is established at certain incident angle, SPR can be excited at the interface between the metal and the dielectric with lower refractive index (e.g. air). There are two possible

configurations for this coupling: the Kretschmann configuration [18] in which a thin layer of metal is evaporated on the prism, and Otto configuration [19] in which a thin air gap is inserted between the metal and the prism. **Figure 1.4** shows the schematic of these two configurations.

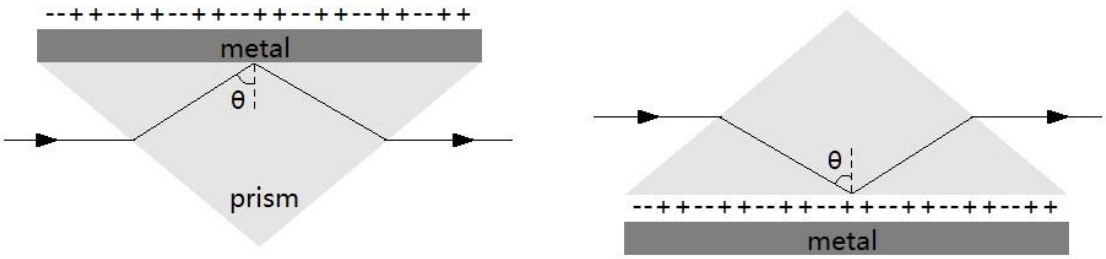

Figure 1.4, Prism couplers for surface plasmon resonance excitation. Left: the Kretschmann configuration. Right: the Otto configuration.

Except for prism coupling, when the light with wave vector k and incident angle θ illuminates a grating, the surface plasmon resonance can also be excited in case of the satisfaction of the following resonant condition:

$$k_{sp} = k \sin\theta + G \qquad \textbf{(1.29)}$$

Where, $k \sin\theta$ represents the wave vector component of incident light is parallel with the metal/dielectric interface, and G represents the reciprocal vector of the grating. [1] A periodical aperture array as a two-dimensional grating is able to excite surface plasmon resonance at normal incidence as well. Detailed discussions about periodical aperture arrays and corresponding optical properties are in **Section 1.2**.

1.1.3 Appropriate metals and beyond

Equation (1.24) has shown that only the sign of the permittivity (real part) for two materials must be opposite in order to realize the surface plasmon resonance excitation at their interface. The permittivity of most dielectrics is a real and positive constant over a wide frequency range. However, thanks to the numerous free electrons in the conduction band, metals possess a complex permittivity with negative real part in the optical frequency range, as well as a high plasma frequency, normally in ultraviolent range. [1, 7] Therefore, metals

are the best material choice to provide SPR coupling by light with the wavelength from ultraviolent to visible and even to near-infrared.

Silver with the lowest losses in visible range has been reported to make plasmonic structures for various applications. However, the biggest disadvantage is that silver is oxidized and corroded easily by a lot of chemicals such as oxygen, sulphide and chloride in its surrounding environment. [20, 21] Gold is another candidate for plasmonic materials, although gold is the more expensive metal, the chemical and physical stability of gold enables it to be the ideal material for plasmonic biosensors. Nevertheless, the significant optical loss below 600 nm wavelength limits the efficient SPR coupling at green and blue light range. [2, 22] Aluminium exhibits superior surface plasmon excitation in the blue and ultraviolent range over silver and gold. Therefore, nanoengineered aluminium surfaces have been reported for enhancing Raman scattering by ultraviolent light. However, a thin oxidation layer over the aluminium results in a red-shift in the SPR. [23-25] Except for pure metals, heavily doped semiconductors such as ITO (indium tin oxide), [26, 27] ZnO (zinc oxide), [28, 29] TiN (titanium nitride), [30, 31] as well as graphene [32, 33] have recently been reported very often to be promising plasmonic materials in future. In this thesis, gold was chosen to make the plasmonic platforms for surface enhanced Raman spectroscopy as biosensing applications, and aluminium was chosen to make the plasmonic nano pixels for novel displays.

1.2 Extraordinary optical transmission (EOT)

1.2.1 Extraordinary optical transmission of nano hole arrays

When free space light encounters a subwavelength aperture perforated in an optically opaque and perfectly conducted metal thin film, diffraction occurs at the aperture's edges. Even at the aperture of the simplest geometry: a circular hole, the diffraction process is still very complicated. From the classical theory, the optical transmission T through a circular hole is promotional to the ratio of r to λ as the power of four: [34]

$$T \propto \left(\frac{r}{\lambda}\right)^4 \qquad \textbf{(1.30)}$$

where, r is the radius of the hole and λ is the incident wavelength. **Equation (1.30)** implies that the optical transmission through a subwavelength circular hole is very weak, since the transmission attenuates very fast as the wavelength increases, even approaching to 0.

However, at optical frequencies, metals cannot be treated as the perfect conductors and exhibit dispersive features as discussed before. The first experiment of optical transmissions through circular nano hole arrays in silver thin film has demonstrated that metallic subwavelength hole arrays are able to allow light transmission and the transmittance per unit hole is much higher than the value predicted by classical diffraction theory, even up to several orders of magnitude. Such enhanced transmission is called extraordinary optical transmission (EOT). [35] Numerous explorations have shown that the presence of surface plasmon resonance and constructive interference result in the EOT phenomenon. [36-39] In this case, classical aperture theory is inappropriate to treat situations in which the surface mode becomes involved in the transmission process.

A periodic subwavelength hole array acting as grating coupler can provide the extra necessary momentum G (shown in **equation (1.29)**) to excite surface plasmon resonance. However, at normal incidence, such extra momentum provided by a square lattice array can be expressed as $G=iG_x+jG_y$, G_x and G_y are the grating momentum vectors associated with two periodicities of the array, i and j are integers indicating the scattering order. [16, 35] When the light encounters a periodic subwavelength hole array, surface plasmon resonance occurs at the incident interface, thus generating an enhanced resonant field confined to the structural surface. At normal incidence, such propagating surface waves not only tunnel through the nano aperture vertically but also travel laterally along the interfaces, causing interference at the rear side, and these waves finally decay to radiant photons. Therefore, each aperture can be treated as a light scatter where the aperture dimension determines the coupling wavelength and array period determines constructive or destructive interferences of the emitted light, thus resulting in the extraordinary optical transmission in the far field. [40-45] **Figure 1.5** shows the diagram of the light-SPR coupling and resulting EOT by a nano hole array.

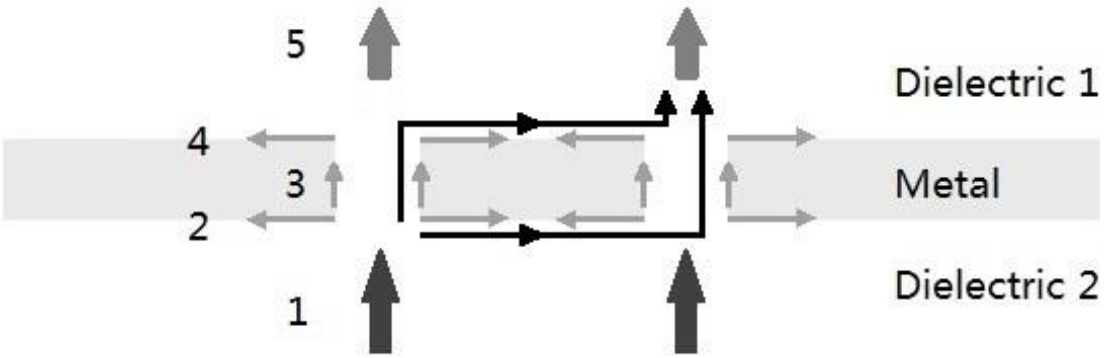

Figure 1.5, Diagram of the light-SPR coupling and EOT. (1) Incident light. (2) Propagating SPR at the incident interface of the nano hole array. (3) SPR tunnelling through the nano hole apertures. (4) Propagating SPR at the rear interface of the nano hole array. (5) Radiant light from the decaying of the SPR. The black lines indicate the interference of laterally propagated surface waves at the neighbouring aperture. In this case, array period affects the wavelength of transmitted light.

However, due to the fact that the EOT phenomenon is a collective effect of various complex processes, it is difficult to give an analytical predication of the resonant wavelength, especially when the geometrical shape of the hole becomes more complicated (rather than a circular hole). Therefore, numerical calculation methods based on FDTD (finite-difference time-domain) or FEM (finite element method) algorithms are commonly employed for the simulation of transmission spectra and the resonant field distributions. [46, 47]

1.2.2 Extraordinary optical transmission of other nano aperture structures

Except for the subwavelength circular hole arrays, other types of nano aperture arrays have been shown to exhibit EOT as well. As a further development of the circular holes, a number of investigations have focused on arrays consisting of annular apertures which can be considered as inserting a cylinder into the hole aperture. Such a geometrical configuration has been reported to achieve EOT both in experiment and simulation. [48-51] With the increase in complexity of geometry, the process of EOT becomes even more complicated. The EOT from the annular aperture array is attributed to the planar surface plasmon (PSP) and the cylinder surface plasmon (CSP). The PSP mainly depends on the periodicity of the surface and the CSP is strongly related to the annular shape. [52-54] In addition to the arrays consisting of symmetric apertures aforementioned, several asymmetric nano aperture arrays like subwavelength rectangular-shaped [55-57]

and elliptical-shaped aperture arrays [58-60] have been investigated for their EOT properties. It needs to be pointed out that the optical transmission of such asymmetric aperture arrays are not only determined by the geometrical dimensions but are highly dependent on the polarisation of the incident light. In asymmetric aperture arrays, one single structure is able to excite different resonant wavelengths by changing the incident polarisation.

Apart from such two dimensional periodical nano apertures, even one single subwavelength circular aperture flanked with shallow grooves can also provide momentum-matching which achieves SPR coupling from incident light, thus yielding a large optical transmission enhancement. Such grooves can be patterned either on the light input side or on the output side, or on both sides. However, only the grooves on the input side contribute to the enhanced transmission, and even a small number of grooves are able to generate a significant transmission. [61, 62] In addition to the surface mode excited by the periodic grooves, many experimental and numerical studies have demonstrated that such enhanced transmission is also a consequence of the aperture waveguide mode. [63] Therefore, geometric shapes and dimensions of the aperture still have an effect on the transmission spectra. More interestingly, if patterning such grooves on the output side, the radiant light can be controlled producing a highly directional emission with narrow angular divergence. [64, 65]

1.3 Applications of nano aperture arrays

There are many applications for metallic nano aperture arrays. However, according to the experimental work described in this thesis, only two applications, the plasmonic biosensor and plasmonic filter are briefly introduced.

1.3.1 Plasmonic biosensor

A biosensor is typically referred to as an analytical device which is able to qualitatively or quantitatively detect biological or chemical molecules by converting the responses of the analyte to readable electronic or optical signals. [66, 67] The samples range from simple chemical molecules to complex biological proteins or nucleic acids. Plasmonic bio/chemical sensors are based on the unique optical properties of various metallic nanostructures. Specifically,

resonant extraordinary optical transmission enables metallic nano aperture arrays to be employed in bio/chemical sensing applications. Generally, there are two mechanisms which are used to achieve molecular sensing based on metallic nano aperture configurations. In one case, when molecules are modified on the structural surface, refractive index change of the surroundings is sufficient to cause a detectable shift in the transmission peak by measuring the transmission spectra before and after molecular modification, thus indicating the presence of certain molecules. [68-71] In another case, highly confined resonant electric fields supported by the nano apertures are able to enhance spectroscopic techniques such as fluorescence [72-75] or Raman scattering. [76-79] For the details of the Raman scattering effect and enhancing methods refer to **Section 1.4**.

1.3.2 Plasmonic filter

A metal thin film perforated with periodical subwavelength holes can generate the extraordinary optical transmission due to the assistance of surface plasmon resonance. Therefore, perhaps the most straightforward application of metallic nano aperture arrays is as a filter. As mentioned before, the resonant frequency associated with the transmission peak can be tuned by varying shape and size of the apertures. Such metallic nanostructures are commonly reported as colour filters [80-82] and mid-infrared (3-8 μm) or terahertz (0.03-3 mm) filters [83, 84] by controlling the holes' shape and dimensions. Meanwhile, some wide band-gap semiconductors, (such as SiC) showing their low-loss properties, have been reported to give enhanced transmission in the mid-infrared range, [85] which broadens the application field of such nanostructures. Nevertheless, when compared to other types of filters such as the interference filter, the relatively low transmission efficiency and broad spectral width of these plasmonic filters need to be significantly improved in order to have real applications.

1.4 Raman spectroscopy

1.4.1 Raman scattering effect

When light is scattered by a particle or molecule, generally there are two types of scattering: Rayleigh scattering which is an elastic scattering process in which

the scattered photons have the same frequency or energy as the incident photons, and Raman scattering which is an inelastic scattering process in which the frequency or energy of scattered photons are either higher or lower than that of the incident photons. Such inelastic scattering of light is named after C. V. Raman, who discovered this phenomenon in liquid. [86] Afterwards, the Raman scattering effect in crystals and gases were observed and recorded. [87, 88] However, in nature, most of the scattered photons belong to Rayleigh scattering, and the Raman scattering effect is typically very weak with approximately 1 in 10 million photons involved. [89]

The interaction between the incident photon and molecule result in an oscillating polarisation inside the molecule. This polarisation is due to the electron cloud displacement relative to the nuclei and reflects the ability of the molecule to interact with incident photon. The consequence of the molecular polarisation is to excite the oscillating electron into a higher energy level which does not really exist and is unstable, therefore, such an energy state is always referred to as a virtual energy level and the electrons excited to this state are going to decay to radiant photons. If the energy of polarisation does not couple to molecular vibration, the scattered photon has the same frequency and energy as the incident photon. This is referred to as Rayleigh scattering. However, if the polarisation couples to molecular vibration in which the electron energy level differs from the state as it is originally, the frequency and energy of scattered photon is different from that of the incident photon. This is referred to as Raman scattering. Therefore, the molecular polarisation generated by external excitation (such as by a laser beam) is necessary for a molecule to exhibit Raman scattering; however, this scattering effect is independent of incident wavelength, and the intensity is proportional to the polarisation energy.

There two types of Raman scattering: Stokes and Anti-Stokes scattering. During the interaction between a molecule and an incident photon, if the electron inside the molecule is excited to the virtual energy state from the ground state (the lowest energy state), and then it returns to the first vibration energy level (which has higher energy level than that of ground state), thus emitting a photon with lower energy (longer wavelength and lower frequency) than that of incident photon. This is referred to as Stokes scattering. The molecule absorbs energy

from the photon and is excited to a vibrational energy state. However, if the electron is excited to the virtual energy state from the first vibration energy level, and returns back to the ground state, the scattered photon has more energy than that of the incident photon, thus resulting in emitted light with a shorter wavelength and a higher frequency than that of the incident light. This is referred to as Anti-Stokes scattering. In this case, the molecule loses energy and returns to the lowest energy state. The intensities of these two scatterings depend on the population of initial state of the molecule. According to thermodynamic equilibrium, the proportion of molecules in different energy states is determined by the temperature. At room temperature, the number of molecules in the ground state is much greater than those in the vibrational energy level. [89] Therefore, Stokes scattering appears to be much stronger than that of Anti-Stokes scattering. **Figure 1.6** shows the electronic energy level diagram of the Rayleigh scattering and Raman scattering processes.

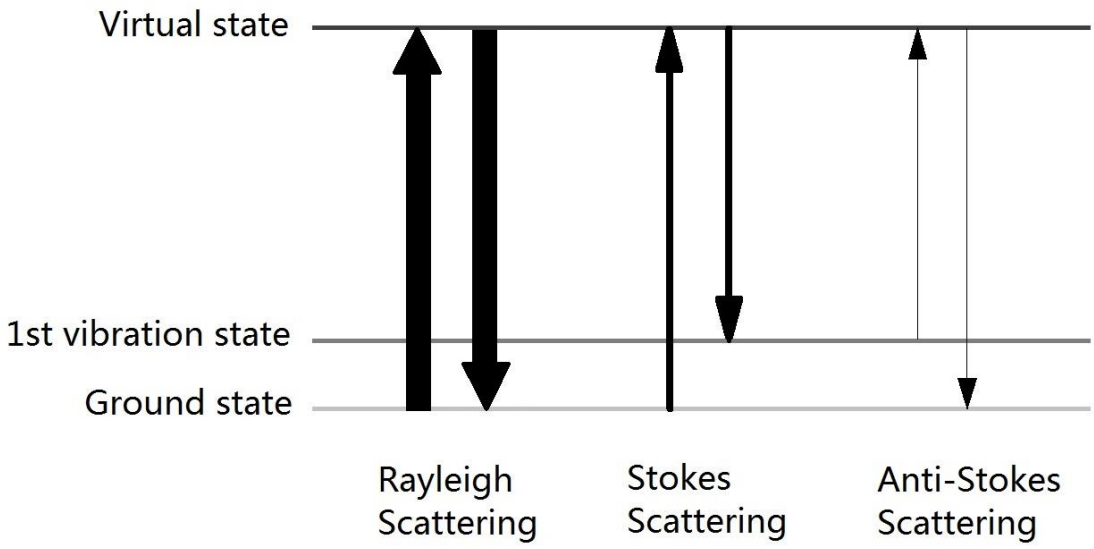

Figure 1.6, Diagram of Rayleigh scattering and Raman scattering. For Raleigh scattering, there is no change in the energy of incident photon and scattered photon. For Raman scattering, the emitted photon has either lower energy (Stokes scattering) or higher energy (Anti-Stokes scattering) than the incident photon's. The line width roughly indicates the proportion of these scatterings occurring at room temperature.

1.4.2 Molecular vibration and Raman spectroscopy

For a molecule in a 3-dimensional space coordinated with x-, y-, and z-axes, degree of freedom is introduced to fully describe the motion of the molecule,

which includes translation, rotation, and vibration. A molecule consisting of N atoms has 3N degrees of freedom, in which three of them correspond to the translational motion (movement along each axis). Another three degrees of freedom correspond to rotational motion for a nonlinear molecule respective to each axis. For a linear molecule, there are only two rational degrees of freedom because the position of atom does not change when rotational motion is along the bond axis of the molecule. The rest of freedoms are all belong to molecular vibrational motions. Therefore, a nonlinear molecule has 3N-6 vibration modes and a linear molecule has 3N-5 vibration modes.

The vibrational motion describes the positional change of the atoms in the molecule. Therefore, the atomic structure of a molecule in space can be determined by examining all the vibrational information of such a molecule. This means the chemical composition can be determined from the molecular structure. Raman spectroscopy is a spectroscopic technique used to obtain the vibrational information of the molecule. The Raman shift of a sample is plotted in the spectral graph showing the intensity of Raman scattering as a function of the wavenumber (in which the unit is expressed as inverse of the wavelength, e.g. cm^{-1}). In fact, wavenumber describes the frequency or wavelength difference relative to that of the incident light, as defined by:

$$\Delta\omega = \frac{1}{\lambda_i} - \frac{1}{\lambda_s} \qquad \textbf{(1.31)}$$

Where, $\Delta\omega$ is the Raman shift expressed in wavenumber format, λ_i is the wavelength of incident excitation light, and λ_s is the wavelength of Raman scattered light. The Raman spectrum is independent of the wavelength of incident light.

Generally, in Raman spectra, the 0 cm^{-1} position represents the excitation light (Rayleigh band), the other peak positions indicate the vibration energy levels corresponding to the different chemical compositions or functional groups. The Raman spectrum is very specific, and inherently sharp and isolated peaks enable this spectroscopic technique to give straightforward qualitative information of the test sample. By comparing the tested Raman spectra with Raman spectral

database which has already been established, it is easy to achieve chemical identification and verification. In addition, Raman spectroscopy is a non-destructive analysis technique because it requires almost no sample preparation and there is no need for contacting the sample during measurement. Raman scattering from water is very weak, thus enabling Raman spectra to be acquired not just from solid and gaseous samples but also from the species dissolved in aqueous solution. Commonly used sampling containers or holders made of glass or transparent polymers are also compatible with this technique. Usually, the sampling time varies from one second to several minutes, thus providing a flexible timescale for the measurement.

1.4.3 Surface enhanced Raman spectroscopy

The surface enhanced Raman scattering effect was first observed in the 1970s when people studied the Raman spectroscopy of pyridine absorbed on an electrochemically roughened silver surface. [90] By modifying the molecules on the surface of nanoscale roughened or artificial nanoengineered metal surfaces usually made of gold or silver, the inherently weak Raman scattering is able to be significantly amplified with the enhancement factor about 10^{10} to 10^{11}, which is sufficient to allow even single molecule detection. [91-94] This sensitive spectroscopic technique is referred to as surface enhanced Raman spectroscopy (SERS).

The mechanism of the SERS effect is still under debate, and the well-developed theoretical explanation is based on electromagnetic theory. The increment in the electric field provided by a particular surface contributed to the significant enhancement of the Raman scattering intensity for the molecules absorbed on such a surface. The excitation of the (localized) plasmonic resonance by the incident laser results in the highly confined resonant electric field. When the frequency (wavelength) of the incident light is in resonance with the plasmonic resonant frequency of the nanostructure, the local field is maximized, thus resulting in the strongest Raman scattering. However, if the frequency of incident light is not matched to the surface plasmonic frequency, the Raman scattering cannot be significantly enhanced. The Raman signal from the molecules absorbed on the metallic nanoengineered surface is proportional to

the fourth power of the resonant electric field provided by such a surface. [95] In contrast to this physical explanation, a chemical interpretation states that the electron transfer involved between some specific molecules and the metallic surface results in the formation of a new electronic state inside the molecules, thus enabling the enhancement in Raman scattering. Compared to the electromagnetic explanation, this chemical mechanism can be applied in some particular cases. [96, 97]

Although the electrochemically roughened gold or silver surfaces have been demonstrated as an effective way for enhancing Raman scattering, [98-101] it is very difficult to predict the intensity, location and excitation frequency of the resonant electric field because of the random scattering caused by such irregular surface topography. With the development of various micro/nano fabrication techniques, metallic nanoparticles [102-104] or nano apertures [76, 105, 106] can be patterned on the substrate surface in a more uniform arrangement. By accurately controlling the geometrical dimensions, the plasmonic resonance of such nanostructures can be tuned to a specific wavelength to match the excitation laser in order to obtain the strongest resonant electric field. Gold and silver are commonly employed as making SERS substrates, because the plasmon frequencies of these metals lie in visible to near infrared range, therefore, commercial lasers with wavelength at such range can be applied as the excitation source. For some metals with a higher plasma frequency, SERS can also be obtained by using ultraviolent (UV) excitation. [24, 107, 108] However, UV SERS is not widely used in biosensing because the UV light can cause the damage of some biomolecules. In addition, several new types of surfaces, such as nanopillars, [109-111] nanowires [112-114] or graphene sheets, [115-117] are reported to enhance Raman scattering as well.

1.5 Research work described herein

The experimental work presented herein concentrates on the exploration of the novel optical properties of periodical metallic nano apertures and their relative applications. The research can be divided into two major areas:

1. By utilising highly confined and enhanced resonant electric field, novel gold nano aperture arrays are fabricated and tested for surface enhanced Raman spectroscopy (SERS) as a prototype platform of molecular sensing.

2. Based on extraordinary optical transmission effect, aluminium nano aperture arrays are proposed as polarisation dependent dual-colour nano pixels and several microscopic chromatic patterns are fabricated by employing such pixels to show the possibility of colour changing and image switching.

Chapter 2 - Materials and Methods

Abstract

This chapter details the materials and experimental methods used in the research. Included in this chapter is an explanation of the simulation techniques used to mathematically model the electromagnetic response of the experimental devices. Also included are working principles for the equipment used in the research and the general experimental methods for the device fabrication, characterisation, and subsequent sensing applications.

2.1 Introduction

Plasmonic nano aperture arrays with their unique optical properties can be used for molecular sensing and novel imaging applications. The nanostructures described in this work were fabricated and characterised by various techniques. The surface enhanced Raman spectroscopic technique was employed for sensing after molecular surface modification on the sample surface. Optical microscopy was used to obtain the images for polarisation dependent micro-image generation. Simulations were used to refine the structural design. All the fabrications were carried out in the James Watt Nanofabrication Centre (JWNC) at the University of Glasgow.

2.2 Materials

Pyrex glass 4 inch wafers, 500 μm thick, were obtained from University Wafer, Inc. (Boston, USA). Metals used for electron beam evaporation such as gold (Au) and aluminium (Al) were obtained from Pi-Kem, Ltd. (Tamworth, UK) Hydrogen silsesquioxane (HSQ) FOX 16 Flowable Oxide was purchased from Dow Corning, Co. ZEP520A was purchased from ZEON, Ltd. Polymethyl Methacrylate (PMMA) was purchased from Lucite International Inc. Tetramethylammonium hydroxide (TMAH) 25% was purchased from Chestech, Ltd. O-xylene, methanol and Isopropanol (IPA) were purchased from Sigma-Aldrich, Co. Acetone was purchased from Fisher-Scientific, Inc. Alcohol and Hydrofluoric (HF) acid were purchased from VWR International, Ltd. Microposit remover 1165 was purchased

from Shipley Chemicals, Ltd. Gold etchant was home made from 32 g iodine, 136 g potassium iodide and 800 ml deionized (DI) water. 4-mercaptobenzonic acid (4-MBA) with 99% purity was purchased from Sigma-Aldrich, Co. One filter wheel (six capacities), filters and linear polarisers were obtained from Thorlabs, Inc. Both the filters and polarisers have the same diameter of 1 inch to match the aperture size of the filter wheel. Two filters have the CWL (central wavelength) 635 nm and FWHM (Full Wave Half Maximum) 10 nm and another two filters have the CWL 488 nm and FWHM 10 nm.

2.3 Methods

2.3.1 Simulation method

2.3.1.1 Finite-difference time-domain (FDTD)

Finite-difference time-domain (FDTD) is a numerical calculation method widely used in modelling the interactions of electromagnetic wave and the surrounding environment and objects. In the Cartesian coordinate system, the algorithm of FDTD employs the finite-difference approximations to both the continuous derivatives in spatial and temporal domain. Therefore, the time-dependent Maxwell equations in the partial-differential forms (**equations 1.1c** and **1.1d**) are rewritten as the corresponding central-difference forms. For three-dimensional FDTD, the whole computation space is divided into numerous cubic grids or the so-called Yee lattice. [118] Each of the cubic grids contains both electric field (E-field) and magnetic field (M-field) vector components. The electric field components are assigned in the centre of each grid edge and their vector directions parallel with each edge. The magnetic field components are assigned at the centre of each grid face and their vector directions perpendicular to the each face. This meshing method means that the E-field and M-field components are separated in a half spatial step. Such discrete fields' components are calculated in a repeated way: the E-field is solved at a time point, and the M-field value is solved at the next time point, and this process runs cyclically until the fields in the whole space are solved. [119, 120] **Figure 2.1** shows the diagram of a three-dimensional (3-D) Yee lattice.

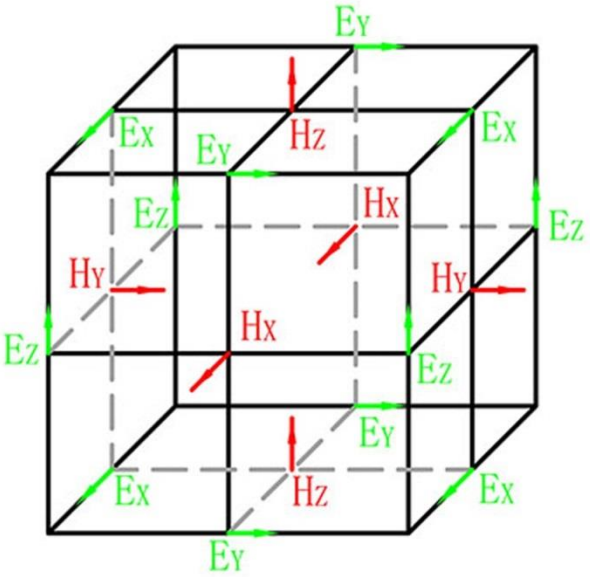

Figure 2.1, Diagram of a 3-D Yee lattice model. The vector components of electric and magnetic field are illustrated in the diagram. [118]

2.3.1.2 Lumerical FDTD solutions

Throughout the research, Lumerical FDTD solutions v7.5 was used to model the optical transmissions and resonant field distributions. Various types of structures (such as rectangular, polygon, circle, ring and et al) were included in the software package for building the simulation model. The dielectric properties of each material can be defined by selecting the data from a material database which is already included in the simulation package. After building the simulation model and defining structural materials, the next step is to add a 3-dimensional simulation region with certain dimensions in the x-, y- and z- axis. In the simulation region menu, background index, meshing accuracy, and boundary conditions need to be specified. If a finer meshing is needed, a mesh override region can be added into the simulation region which gives overriding meshing values in each axis. The third step is to position the source and monitors. The source, which includes: Dipole, Gaussian, plane wave etc., is used to generate an incident electromagnetic wave. The intensity and phase, polarisation, propagating direction and wavelength range for the incident wave need to be defined. Two commonly used monitors are: the frequency domain power monitor for plotting optical spectra, and the frequency domain field monitor for visualising field distributions. The sampling points and range, calculated values (such as field components along each axis and power (Poynting

vector which represents the electromagnetic field flux density)) and the monitor dimensions need to be defined. The monitor is able to plot the simulated results (spectra or field distributions) in a JEPG format or export such data into a TXT format which can be processed in other software. [121]

For all the simulations in this thesis, the simulation space was firstly defined from z=-500 nm to 2000 nm, with the dimensions in x- and y- axis representing the array period. The interface of metal and glass was positioned at z=0 nm. The refractive index below the metal was set at 1.47 to represent the glass substrate and the refractive index above the metal was set at 1 to represent the air. The dielectric values for gold was set at Johnson and Christy, [122] and for both aluminium and SiO_2 were set at Palik. [123] Only one nanostructure was enclosed in the simulation space. Perfect matched layers (PML) were applied to the boundaries at the z-axis, and periodical conditions were applied to the boundaries at the x- and y- axis representing an infinite array. The spectral data were exported from the power monitor and plotted in the Origin 8 package and the field distributions were directly plotted in the field monitor and saved as a figure.

2.3.2 Fabrication and characterisation techniques

2.3.2.1 Electron-beam lithography

Electron-beam (e-beam) lithography is to directly pattern arbitrary shapes on the substrate surface. Before e-beam exposure, a polymer thin film is spin coated onto a substrate. This polymer is sensitive to electron radiation and can be selectively removed by a specific chemical solvent after e-beam exposure. Such polymers are called “resist” and the solvents are called “developer”. This process of generating patterns in the resist layer is called “development”. E-beam lithography a further development of photolithography allows fabrication of fine structures with nanoscale resolution. In contrast to the ultraviolet (UV) light used in photolithography, an e-beam lithography system uses an electron beam to generate tiny patterns, because electrons can be easily focused to a smaller size than the photons with no significant diffraction. In addition, unlike photolithography where patterns were exposed at the same time, e-beam lithography is a direct-writing system which means it can only expose one unit

area at one time and expose another unit area at another time, thus requiring long writing time with limited throughput. Nevertheless, e-beam lithography has incomparable advantages in making features smaller than one micron, causing it to be widely used in scientific research.

Typically, the e-beam lithography tool consists of an electron gun, beam focusing parts, sample holder, vacuum and pumping system. The electron gun emits free electrons by thermal or field emission, and the strong electric field produced by the anode with a high voltage accelerates the free electrons to generate the electron beam. The high energetic electron beam is focused by a series of electromagnetic lenses and deflected by coils. However, only small area can be scanned by beam deflection, therefore, in order to expose a large area, it is necessary for the sample stage to move accurately. By using the vector scanning method, the designed pattern with custom shapes can be written. [124-127] **Figure 2.2** shows the schematic of an e-beam lithography tool and vector scanning.

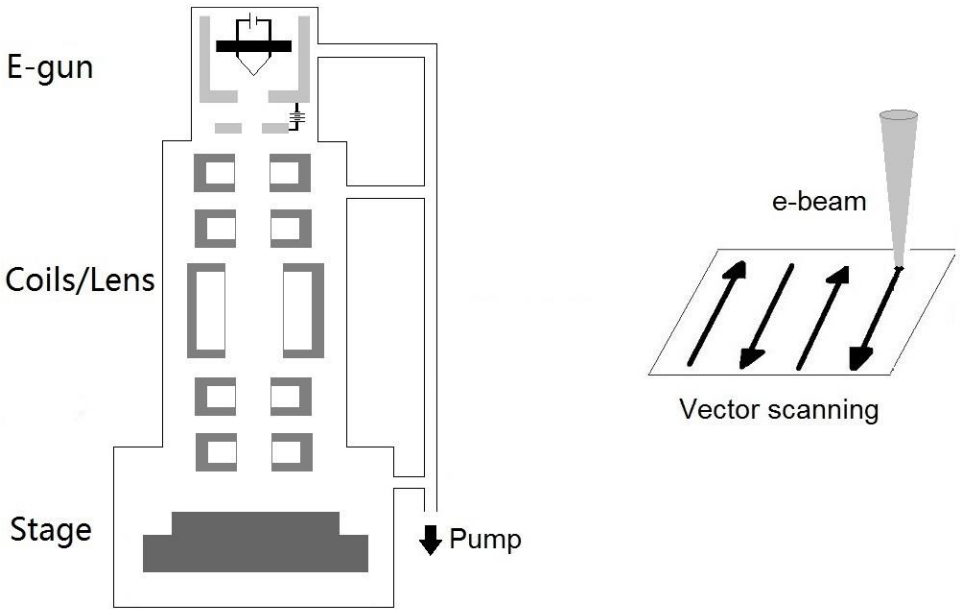

Figure 2.2, Schematic of e-beam lithography tool and vector scanning. Left: schematic of e-beam lithography tool, the system is working at a high vacuum condition. Stage chamber is vented to atmosphere when loading or unloading the samples. Right: schematic of vector scanning, the arrow indicates the scanning direction.

A conductive substrate is required for e-beam lithography to allow the electrons to dissipate away. For a non-conductive substrate (such as glass), a thin layer of

metal is necessary to act as a conduction layer. Otherwise, excess electrons accumulate on the substrate surface and repel incoming electrons, resulting in the beam distortion which significantly affects pattern shape and resolution.

Before exposure, resist is spin coated on the substrate. Thickness is controlled by spinning speed and time. E-beam resists can be divided into positive tone resist and negative tone resist. For positive resist, electrons break the long-chain in the polymer, thus generating the short-chain and more soluble polymers. For negative resist, the short-chain polymers are cross-linked to long-chain insoluble or less soluble polymers upon electrons exposure. In other words, after e-beam exposure and development, the exposed positive resist is removed while the unexposed positive resit is left, and the exposed negative resist is left while the unexposed negative resist is removed. [128, 129] **Figure 2.3** shows the positive and negative resist profile after e-beam exposure and development.

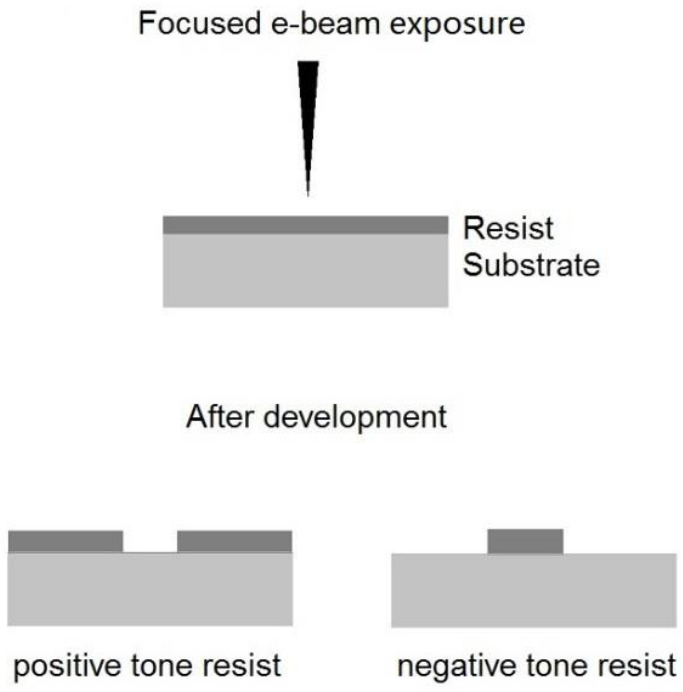

Figure 2.3, Resist profile after e-beam exposure and development for positive and negative resists. Different developers are used for different resists. For each resist, the concentration of the developer and development time may be different.

An appropriate exposure dose is important to fully expose the resist. Exposure dose ($\mu C/cm^2$) refers to the electron charge quantity per area. In addition, Electrons are scattered by the molecules inside the resist and substrate,

including both forward in the resist layer and backward scatterings from the substrate. Those scattered electrons travel through the resist laterally and expose the adjacent area, thus effectively enlarging the exposed pattern size, which gives rise to the so-called “proximity effect”. This effect is more pronounced for making tiny features in a very thick resist layer, therefore relevant corrections need to be carried out. **Figure 2.4** shows the diagram of electrons scattering inside the resist.

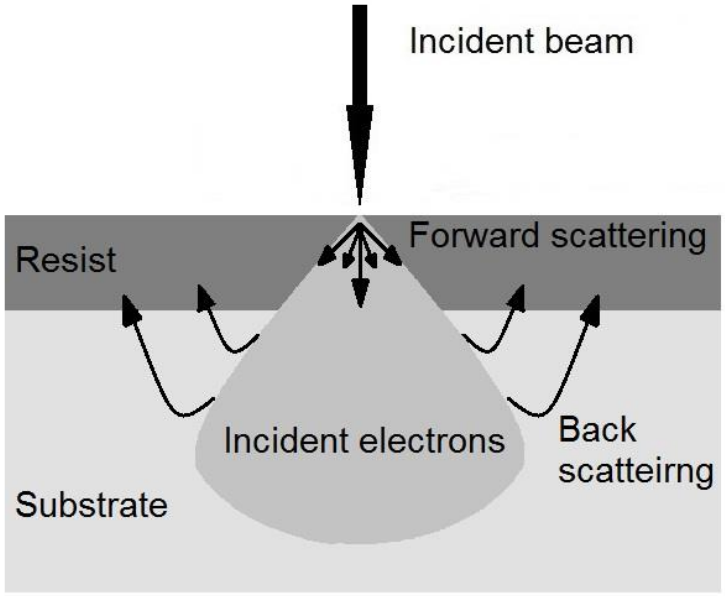

Figure 2.4, Electrons scattering by the resist. The grey sector indicates the exposed area in the resist layer and the profile of incident electrons inside the substrate. Generally, the lower incident energy leads to a larger forward scattering area. Such exposed area ranges from tens of nanometres even up to microns in lateral, which depends on the beam energy, resist thickness, feature size and so on. [130]

In JWNC, a Vistec VB6 UHR EWF tool is used for e-beam lithography and operates at 100kV. The minimum beam size of this machine is about 4 nm. The distance between two consecutive spots is termed as beam step size (BSS), it is calculated by: BSS = Resolution × VRU, where, VRU (variable resolution unit) is an integer number. Setting beam size about 25% larger than the BSS can guarantee that both the resist is fully exposed and the writing time is acceptable. Writing time can be estimated by: D × A=T × I, where, D is exposure dose, A is exposure area, T is the writing time, and I is the beam current.

2.3.2.2 Reactive-ion etching (RIE)

Reactive-Ion etching is used to chemically and physically react and remove materials on a substrate by using plasma and this technology is widely referred to as “dry etch”. The most common RIE system consists of a cylindrical vacuum chamber, upper and lower electrodes, substrate table, gas supply, and pumping system. Two parallel plates as upper and lower electrodes are placed inside the chamber. The substrate table sits lower electrode but is electrically isolated from it. The gas inlet is on top of the chamber while the pumping system is at the bottom. A high vacuum condition is achieved by the turbo pump and this is necessary for striking the plasma. Gas enters into the chamber at a flow rate controlled by a mass flow controller (MFC) to keep the chamber pressure in the millitorr (mTorr) range. Plasma is initiated by applying RF (radio-frequency) power at upper or lower electrode. The gas molecules absorb energy from the RF power and become ionized plasma. Electrons in the plasma are easily influenced by EM field due to the light weight compared to massive ions. As a consequence, electrons tend to move along the EM field and accumulate, resulting in a self-established voltage bias, ranging from tens to hundreds of volts. This voltage is crucial to maintain the plasma and accelerate the ions. Then highly energetic ions etch the substrate with both chemical reactions and physical bombardment. Since most of the ions are accelerated in a vertical direction, RIE is an anisotropic etching process. [131, 132]

Gas flow rate, chamber pressure and power can be adjusted to get a different etch rate and structural profile. Various gases can be chosen to etch different materials, for instance, fluorine based gases such as CF_4 or CHF_3 can be used for etching silicon nitride; chlorine based gases such as Cl_2 or BCl_3 can be used for etching gallium arsenide (GaAs) and so on,. [133, 134] A mask is used to confine etching to specific areas on the substrate. The area covered by the mask is protected while the exposed area is etched away. Commonly used mask materials include resist, silicon nitride and metals such as nichrome. Etching depth can be roughly controlled by etching time. However, another more accurate etching method is to use interferometer which is based on laser interference. A laser beam reflected from the substrate surface interferes with the incident beam. As the substrate is etched, the thickness of the substrate

decreases so that the optical path of the reflection beam increases, thus resulting indifferent interference signals. Through detecting these signal changes, etching depth can be monitored in real time. **Figure 2.5** shows the schematic of the RIE system and the process of selective etching by a mask.

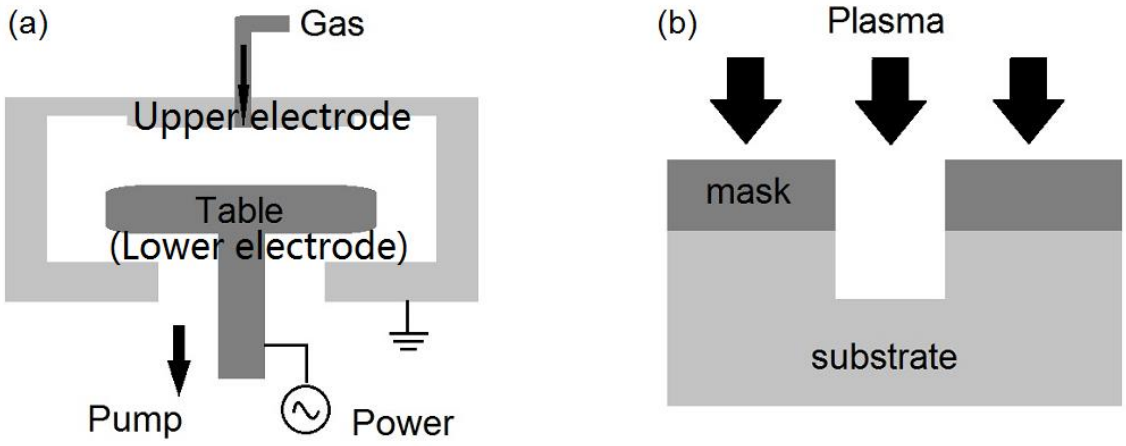

Figure 2.5, Schematic of RIE system and process. (**a**) RIE system. (**b**) Substrate selective etching by a mask. Patterns on the mask can be transferred by photolithography, e-beam lithography or other fabrication techniques.

In JWNC, an Oxford Instruments Plasmalab 80Plus RIE system and an Oxford Instruments Plasmalab system100 RIE system are RIE systems. The 80Plus RIE has a 240 mm diameter table inside a single chamber. The single chamber makes substrate loading/unloading easy. The System100 RIE has two chambers which are load-lock and inter-lock connected by a high vacuum valve. The substrate is firstly loaded in the load-lock chamber with pump down to ~7.5 mTorr and then transferred into the inter-lock chamber by robotic arm. The plasma in both machines is driven by 13.56 MHz RF (radio-frequency) power. Ashing and cleaning are based on O_2 plasma in both machines.

2.3.2.3 Plasma enhanced chemical vapor deposition (PECVD)

Chemical vapor deposition is a thin film deposition technology. Dielectric, metal oxides and metal nitride thin film can be deposited on a substrate from gas state to solid state within the plasma. New materials are created by chemical reactions in the plasma and deposited on the sample, thus forming the thin film. Film thickness is depended on the deposition time. [132, 135] For example, silane and oxygen are commonly used gases for the deposition of silicon dioxide.

The reaction is: $SiH_4 + O_2 \rightarrow SiO_2 + 2H_2$.The set-up of one PECVD is similar to the RIE system. Plasma is ignited between upper and lower electrodes in the vacuum chamber which is filled with chemical gases. RF power is used to generate plasma. In some cases, the substrate table in the PECVD system can be heated to hundreds of degrees Celsius during deposition. Another type of PECVD is inductively coupled plasma chemical vapor deposition (ICP-CVD). The inductively coupled plasma is generated by a strong magnetic field by inductance coils outside the chamber. This method allows film deposition at room temperature.

2.3.2.4 Electron-beam evaporation

In JWNC, a Plassys MEB 400S electron-beam evaporator is used for metallization. The machine has a valve to separate the load-lock chamber and a deposition chamber which is normally kept at a high vacuum. The load-lock chamber can be vented to atmosphere for loading and unloading the sample, while the deposition chamber still remains in a high vacuum condition. The metal sources and electron gun are inside the deposition chamber. There are eight metals which can be chosen. The electron beam is generated at 10 kV, deflected and directed onto the metal by a magnetic field. The solid metal is rapidly heated up and changes to a vapor state by absorbing energy from the electron beam. Quartz crystal is used for monitoring the evaporation rate and film thickness by detecting its oscillation frequency. **Figure 2.6** shows the schematic of the evaporator.

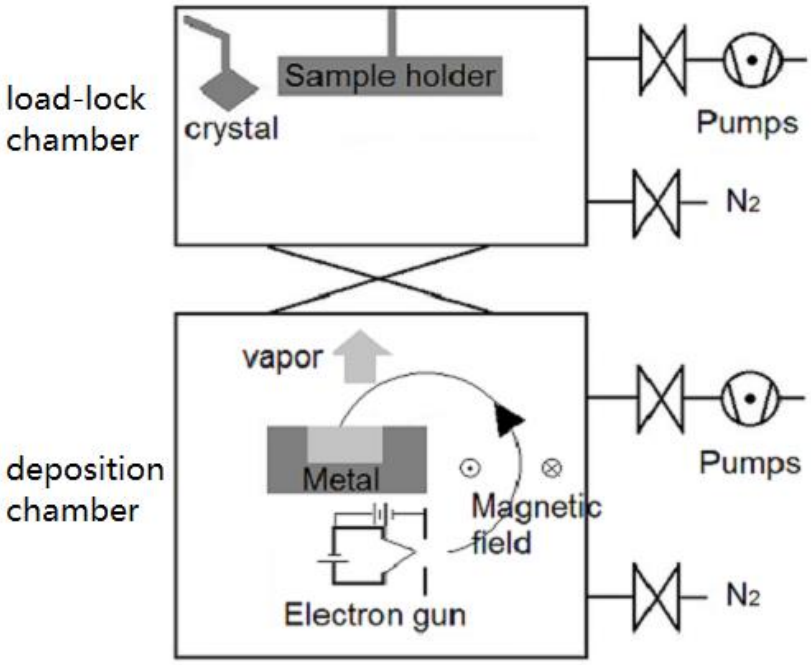

Figure 2.6, Schematic of the e-beam evaporator. Each chamber is pumped by a rotary and a cryogenic pump. N_2 is used for venting.

2.3.2.5 Scanning electron microscope (SEM)

The size of the focused electron beam is much smaller than that of light, resulting in higher resolution (which can be defined as the shortest distance between two points that can be distinguished as two separate objects) of the SEM compared to the traditional optical microscope. Apart from imaging, SEM can be used for chemical analysis as well. Similar to the e-beam lithography tool, within a vacuum column, an electron beam generated from an electron gun is focused by electromagnetic lenses and deflected by coils to scan over the sample surface. The SEM is used to image the sample's surface topography. Lenses and apertures control beam size as well. A high resolution image is produced by the signals from a secondary electron (SE) detector. Higher voltage and smaller working distance (the length between the final lens and sample) will give higher resolution images. Some SEMs equipped with back scattering electron (BSE) detectors and X-ray detectors (XRD) are used for chemical analysis. [127, 132] To get a clear SEM image, the sample must be conductive. For non-conductive material, a metal layer is sputtered over the sample to make it conductive. **Figure 2.7** shows the Schematic of a SEM.

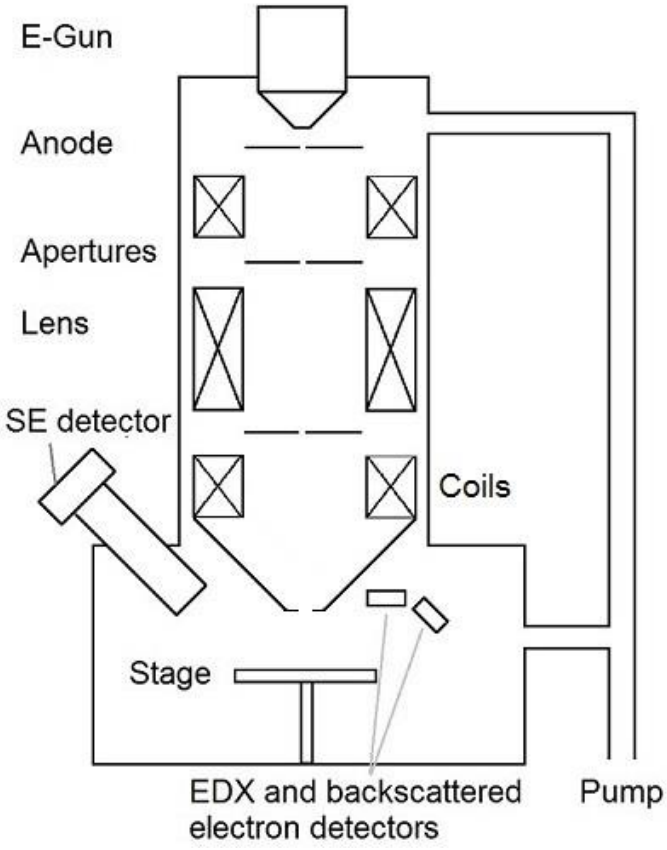

Figure 2.7, Schematic of the SEM. All components work in vacuum conditions.

2.3.2.6 Spectrophotometer

A spectrophotometer (single beam or double beam) is an instrument used to measure the light transmission, reflection or absorption of the sample as a function of wavelength (or reciprocal to wavelength such as electron volts or wavenumber). [136] Throughout this research, only the transmission spectra of the samples were measured. Transmittance is the ratio of the intensity of light transmitted through sample to the intensity of the reference light. Monochromatic light of different wavelengths is generated by rotating the diffraction grating. For a double beam UV-visible-NIR spectrophotometer, the single monochromatic beam is split into two beams with the same wavelength and intensity through a beam splitter. These two beams are used as the sample beam and the reference beam and their intensities are detected by two photo detectors respectively. Because the light intensity from the source might vary, a baseline scan is necessary to calibrate the detectors and compensate for such intensity variations. **Figure 2.8** shows the schematic of a double beam spectrophotometer.

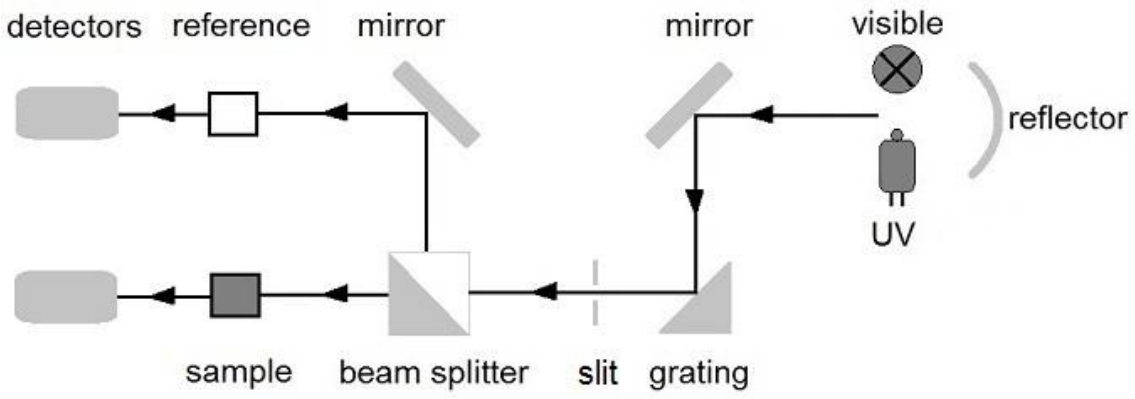

Figure 2.8, Schematic of a double beam UV-visible-NIR spectrophotometer. Near infrared (NIR) and visible range wavelengths are generated by diffraction of white light, and ultraviolet light is generated by a UV tube. The slit is to control the width of incident beam.

2.3.2.7 The Raman spectrometer

A Raman spectrometer is an analytical instrument used to measure and plot the Raman spectrum of analyte(s). There are three main parts of the Raman spectrometer: excitation sources, optical sampling systems and spectrometers. Laser light is chosen as the ideal excitation source due to its high photon density, ensuring that more photons are involved in the process of Raman scattering, thus enabling the detection of weak signals. Commonly used laser wavelengths (such as 533 nm, 632 nm, 785 nm and 1064 nm) range from visible to near infrared. The optical sampling system consists of mirrors, focusing lenses, notch filters and a microscope. The laser beam is collimated by a series of free space optical components. The objective on the microscope is to focus the laser onto analyte(s), and also collect the scattered light to a notch filter where the spectra components of Rayleigh scattering (in which the wavelength of the scattered light is the same as that of the excitation light) in the total scattered spectrum is filtered out, thus achieving the separation of Raman signals. The spectrometer disperses the Raman spectrum by gratings, and the intensity of the Raman scattering is measured by a CCD (charged coupling device). [137, 138] The intensities of Raman scattering are plotted versus the wavenumber which is the wavelength shift relative to that of the excitation laser. The schematic of Raman spectrometer is shown in **Figure 2.9**.

Raman spectroscopy can be used as a quantitative analytic technique and is necessary to estimate or calculate the total number of molecules involved in the Raman scattering process. Therefore, it requires calculating the resolution of laser spot coming from an objective, because the scattered Raman signals can be excited only from the molecules within the focus area. The diameter of the focused laser spot, D, can be estimated by using the equation: $D = \frac{1.22 \times \lambda}{NA}$, where, NA is the numerical aperture of the objective (if a condenser is applied in microscope, NA equals to the sum of objective's and condenser's numerical aperture), and λ is the laser wavelength.

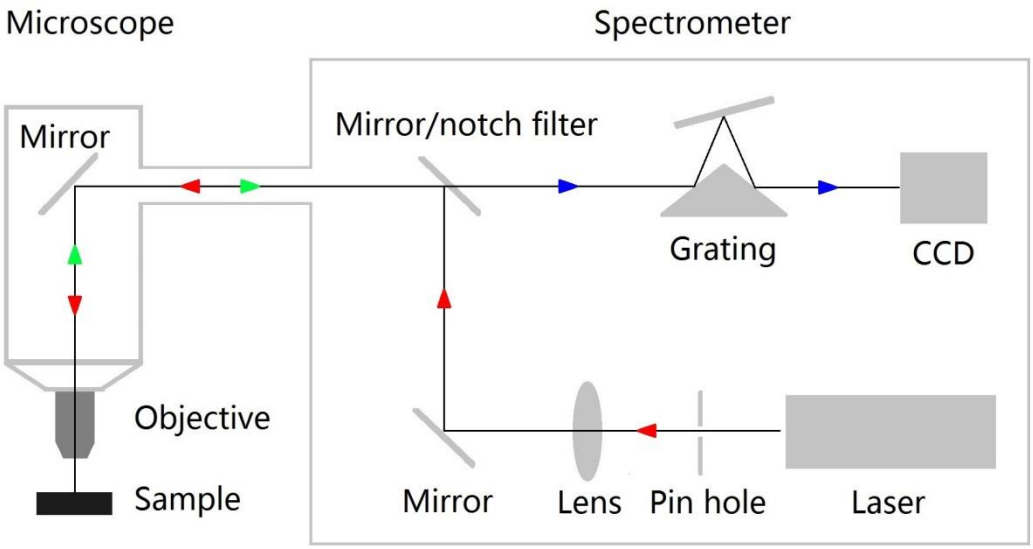

Figure 2.9, Schematic of a Raman spectrometer. The laser beam size is controlled by the pin hole. The red arrow indicates the incident laser. The green arrow indicates the total scattered light (Rayleigh scattering and Raman scattering). The blue arrow indicates the Raman scattered light.

2.3.3 Experiment methods

2.3.3.1 Cleaning

A Pyrex glass wafer was firstly cleaved into 15×15 mm small piece substrates. Substrates were separately immersed into acetone, methanol and IPA, in that sequence, for 5mins in each with applied ultrasonic agitation to clean all the organic/inorganic contaminations, and then rinsed in DI water, and finally blow dried by nitrogen.

2.3.3.2 Metallization

A Plassys MEB 400S was used for Au and Al evaporation. The substrate was placed upside down in the load-lock chamber. The whole process was automatically controlled and all the necessary evaporation recipes were included in the controlling software. Evaporation rate of Au and Al was both 0.3 nm/s.

2.3.3.3 Dielectric thin film deposition

Silicon dioxide (SiO_2) deposition was carried out in an Oxford Instrument Plasmalab 80Plus PECVD machine by using SH_4/N_2O/N2 gases with flow rates 70/200/85 sccm, at 15 W, 1000 mTorr and 300°C. The deposition rate was 60 nm/min.

Silicon nitride (Si_3N_4) deposition was carried out on either Oxford Instrument Plasmalab 80Plus PECVD machine or Oxford Instrument Plasmalab System100 ICP-CVD machine. For PECVD, $SH_4/N_2/NH_3$ gases were used with flow rates 8/170/16 sccm, at 20 W, 1000 mTorr and 300°C. The deposition rate was 20 nm/min. For ICP-CVD, SH_4/N_2 gases were used with flow rates 7/6 sccm, at 100 W, 4.4 mTorr and 40°C. The deposition rate was 16 nm/min.

2.3.3.4 Resist spin coating

HSQ (a negative resist) and ZEP520A (a positive resist) were used in the research. Resist coating was carried out by a spinner which uses the vacuum to hold down the sample. The substrate was firstly covered with resist by using a plastic pipette, and then spun at high speed for 60 seconds to form a thin resist film on the substrate. Before exposure, substrate baking is needed to evaporate the solvent in resist and release film stress. HSQ was baked on a 90°C hotplate for 5 minutes and ZEP520A was baked in a 180°C oven for 40 minutes. Throughout the research, neat HSQ, neat ZEP and a 50% dilution ZEP (1 part ZEP and 1 part anisole) were used. ZEP520A due to its high etching resistance was used as the mask for nitride and Al etching as well.

2.3.3.5 E-beam lithography

Exposure patterns were firstly designed in L-Edit version 15 (This software was developed by Tanner Research, Inc.) and exported as a graphical data system (GDS) file which may contain multilayer patterns. Layout beamer (This software was developed by GenlSys Gmbh.) was then used to extract each layer in the GDS file and generate each corresponding file with its resolution in VEP format (machine format for VB6 beam writer) separately. Layout beamer had three resolution options which could be chosen being 0.5 nm, 1 nm and 1.25 nm. And then each VEP file was opened in a Belle programme. Substrate size and exposure parameters such as dose, beam size VRU and pattern position were defined in Belle as well. Finally, the Belle file was transferred to VB6 machine for writing. Sample patterns of all plasmonic structures were designed in a 0.5 nm resolution in L-Edit and Layout beamer, and written by an electron beam with 4 nm beam size. The VRU value was set to 6 for patterning gold circular apertures and aluminium cross-shaped apertures, and was set to 7 for patterning gold annular apertures and split-ring shaped apertures.

2.3.3.6 Development

HSQ was developed in 25% Tetramethylammonium hydroxide (TMAH) solution at 23°C for 30 seconds, then rinsed in DI water twice for 30 seconds, and then rinsed in IPA for 15 seconds and blow dried with nitrogen. [139] ZEP520A was developed in o-xylene at 23°C for 40 seconds, and then rinsed in IPA for another 40 seconds and blow dried with nitrogen. [140]

2.3.3.7 Nitride plasma dry etching

Thin layer nitride (10nm) etching was carried out on Oxford Instruments Plasmalab System100 RIE by using SF_6/N_2 gases with flow rates 25/50 sccm, at 20 W, 15mTorr and 28°C. The etch rate was 15 nm/min. Thick layer nitride (200nm) etching was carried out on Oxford Instruments Plasmalab 80Plus RIE by using CHF_3/O_2 gases with flow rates 50/5 sccm, at 150 W, 55 mTorr and 20°C. The etch rate was 70 nm/min.

2.3.3.8 Metal plasma dry etching

Gold dry etching was carried out on Oxford Instruments Plasmalab 80Plus RIE by using Ar with flow rate 21.4 sccm, at 250 W, 30 mTorr and 20°C. The etch rate was 30 nm/min. Aluminium dry etching was carried out on Oxford Instruments Plasmalab System100 RIE by using $SiCl_4$ with flow rate 18 sccm, at 250 W, 9 mTorr and 20°C. The etch rate was 30 nm/min.

2.3.3.9 O_2 plasma ashing and cleaning

An O_2 plasma ash was used for removing the un-developed resist residues. This process gently etched away approximately several nanometres of the resist layer. Both Oxford Instrument Plasmalab 80Plus RIE and System100 RIE machines can run O_2 ash at the same conditions: O_2 flow rate 10 sccm, at 10 W, 50 mTorr and 20°C. O_2 plasma cleaning was for stripping off any of the undesired polymers on the sample. This process was to etch away the polymers for up to several microns. The O_2 cleaning condition in Oxford Instrument Plasmalab 80Plus RIE was: O_2 flow rate 50 sccm, at 100 W, 50 mTorr and 20°C.

2.3.3.10 Gold wet etch

Gold wet etchant was made by the staff of JWNC. It was made from 32 g iodine, 136 g potassium iodide and 800 ml DI water. The etch rate of the etchant was very fast, a 100 nm gold film was completely dissolved away within 30 seconds. 1 part of pure gold etchant was diluted by 5 parts DI water for gold wet etching. The sample was immersed in the diluted etchant with ultrasonic for 4 seconds for 15 nm gold etching.

2.3.3.11 Scanning electron microscope

A Hitachi S4700 scanning electron microscope was used to capture high resolution images of all the samples throughout the research. It was normally operated at 10 kV voltage and 10 μA current in SE (secondary electron) mode with working distance 12 mm. To capture a high resolution image, the working distance was reduced to 5 mm.

2.3.3.12 Optical transmission measurement

A Shimadzu UV3101PC spectrophotometer was used to measure transmission spectra. It is a double beam spectrophotometer with one beam for sample measurement and the other for the reference. Both of these two beams are generated from the same light source. Two diffraction gratings involved in generating monochromatic light to cover a wide wavelength range from visible to near infrared. Grating changing is executed at 894 nm, therefore, it unavoidable that the spectrum is discontinuous around that wavelength.

Before measurement, a baseline scan was carried out to calibrate the detectors. Two empty holders were placed in the sample and reference positions and the pinhole in each holder was aligned to the corresponding incident beam. The baseline scan range was the same as the measuring range. Then a testing sample was attached to the sample holder using Blu-Tack. It was necessary to make sure the sample was fully in contact with the holder and guarantee there was no gap between them. The testing array on the sample was aligned to the pinhole with correct orientation. The sample holder was then placed in the right position by aligning the pinhole to the sample beam. A piece of clean Pyrex glass was attached to the reference holder which was then placed in the reference position by aligning the pinhole to the reference beam. **Figure 2.10** shows images of the sampling setup of Shimadzu UV3101PC spectrophotometer and the sample holder.

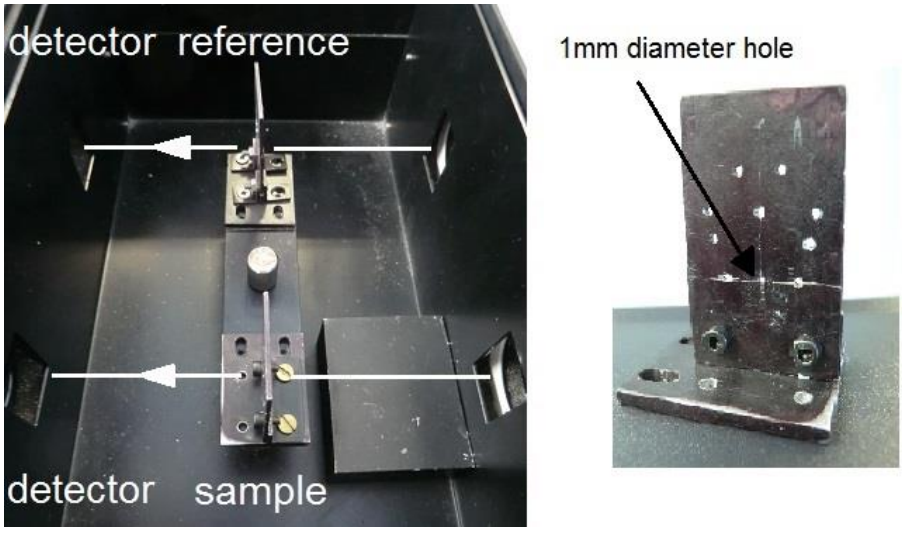

Figure 2.10, Measurement set up in spectrometer and self-made sample holder. 1 mm diameter hole was indicated for beam alignment.

For measuring the polarisation dependent transmission spectra, linear polarised incident light was generated by placing a Thorlabs linear polariser between the incident light and the sample. The direction of incident polarisation was fixed during baseline correction and actual measurement. The test sample was rotated to the parallel or perpendicular position relative to the incident polarisation. **Figure 2.11** shows the sampling setup for measuring polarisation dependent transmission spectra.

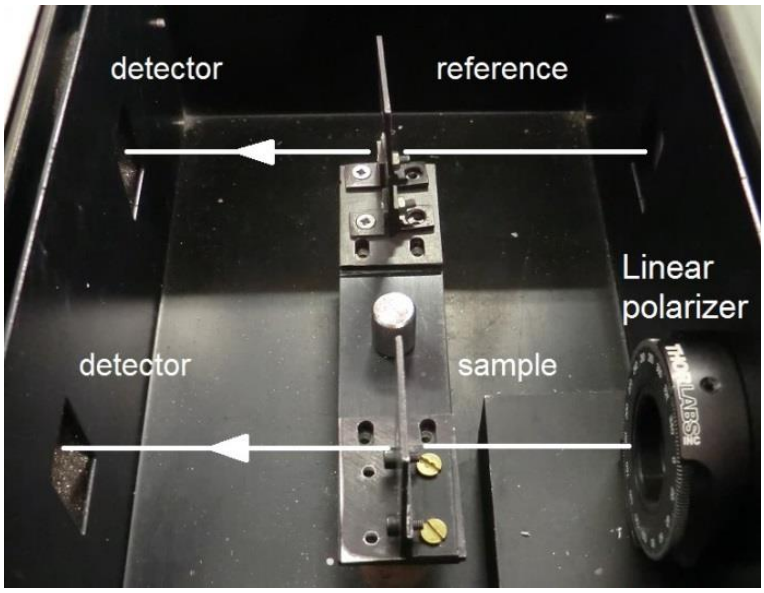

Figure 2.11, Polarisation dependent optical transmission spectra measurement setup. Normal incidence of light toward the polariser must be guaranteed.

2.3.3.13 Surface modification of 4-mercaptobenzonic acid (4-MBA)

At room temperature, 4-MBA appears in powder form with a light yellow or faint beige colour and it is soluble in some organic solutions (e.g. alcohol). Its molecular formula is $C_7H_6O_2S$, molecular weight is 154.19 g/mol and melting point is 215-224 degrees Celsius. 4-MBA consists of a thiol group (-SH), a carboxyl group (-COOH) and a benzene ring. A lot of research have proved that surface modification of 4-MBA on gold surface can be achieved by forming a self-assembled monolayer (SAM) via the bond between thiol group and gold atom. [141, 142] **Figure 2.12** shows the chemical structure of 4-MBA and the schematic of its monolayer on a gold surface.

The detailed procedures for surface modification are as follows: 15.4 mg 4-MBA (0.1 mmol) was dissolved in 10 ml alcohol to get a 10 mmol/L concentration

molecular solution. The sample was surface modified by immersing it into such a solution for 2 hours at room temperature, and this was then flushed by alcohol to wash away excess solution on its surface. Finally, the sample was blow dried with nitrogen, forming a 4-MBA SAM layer on the gold array's surface.

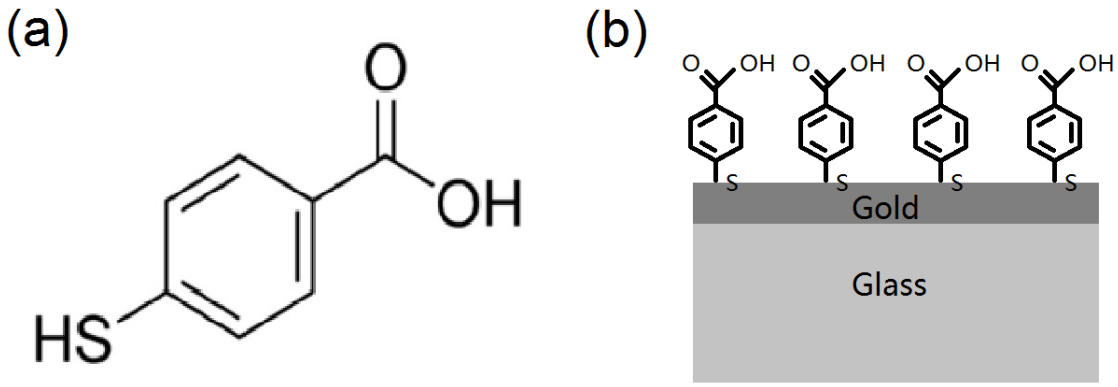

Figure 2.12, Schematics of 4-MBA and surface modification. (**a**) Chemical structural formula of 4-MBA. (**b**) Schematic of the 4-MBA monolayer modified on gold surface.

2.3.3.15 Surface enhanced Raman spectroscopy (SERS)

Horiba Jobin Yvon LabRam HR800UV and LabRam INV spectrometers were used for the SERS measurements. First of all, a piece of silicon was used to obtain the Raman peak at 520 cm^{-1} to calibrate the spectrometer. Then, the test sample was face-down placed, on a holder which was clamped on the microscope stage. During the measurement, the diameter of the pin hole was set to 1000 μm. The raw data were processed for spectra baseline and smoothing in Horiba LabSpec software. For LabRam HR800UV, the Raman spectrometer was conjunct with an Olympus IX71 microscope and the power of 633 nm HeNe laser was 2 mW. The laser power was measured at the objective. A 600 grooves/mm grating is used in the spectrometer. For LabRam INV, it was conjunct with an Olympus IX70 microscope and the power of 633 nm HeNe laser was 5 mW. The laser power was measured at the objective as well. A 1800 grooves/mm grating is used in the spectrometer. Both the SERS measurements had the same range 900-1700 cm^{-1} and the acquisition time of each measurement was set at 5 seconds. **Figure 2.13** shows the optical setup of LabRam HR800UV and LabRam INV spectrometers.

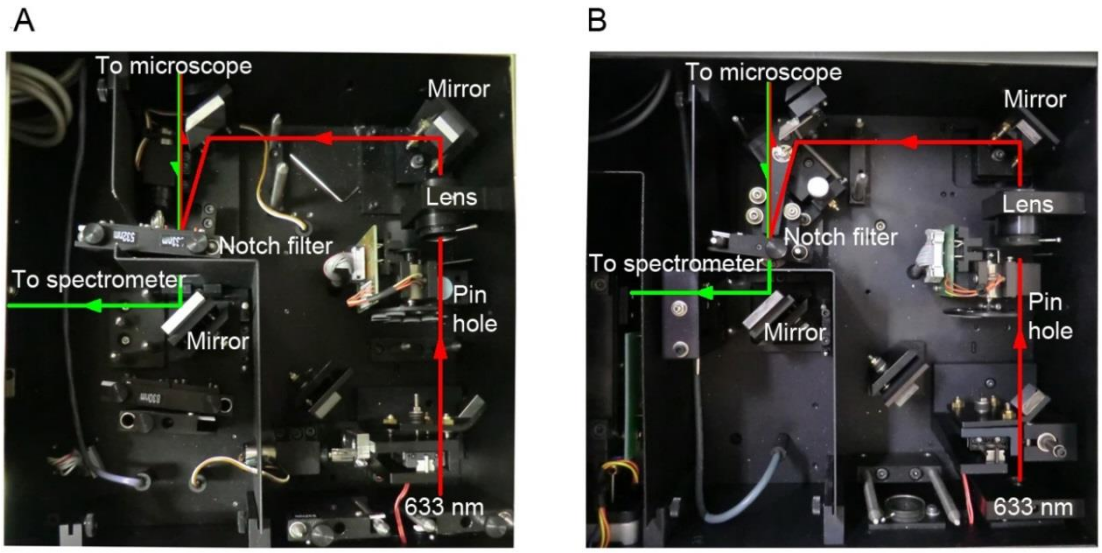

Figure 2.13, Optical setups of the Raman spectrometers used for measuring the Raman scattering. (**A**) Optical setup of LabRam HR800UV spectrometer. (**B**) Optical setup of LabRam INV spectrometer.

2.3.3.16 Optical transmission micro-imaging

A Zeiss Axio Imager A1 optical microscope in conjunction with a JENOPTIK CCD camera was used to take the images of plasmonic structures as colour pixels and relevant chromatic micro-patterns made up of such pixels. A linear polariser was installed in the microscope between back-illuminated light source and the test sample to control the polarisation of incident light. A 12V 100W Tungsten-Halogen bulb was used for the light source. Before capturing pictures, the auto white balance was carried out without clamping any sample on the stage. The exposure time for capturing each image was 150 ms. **Figure 2.14** shows the schematic of optical microscope for capturing the polarisation dependent optical transmission images.

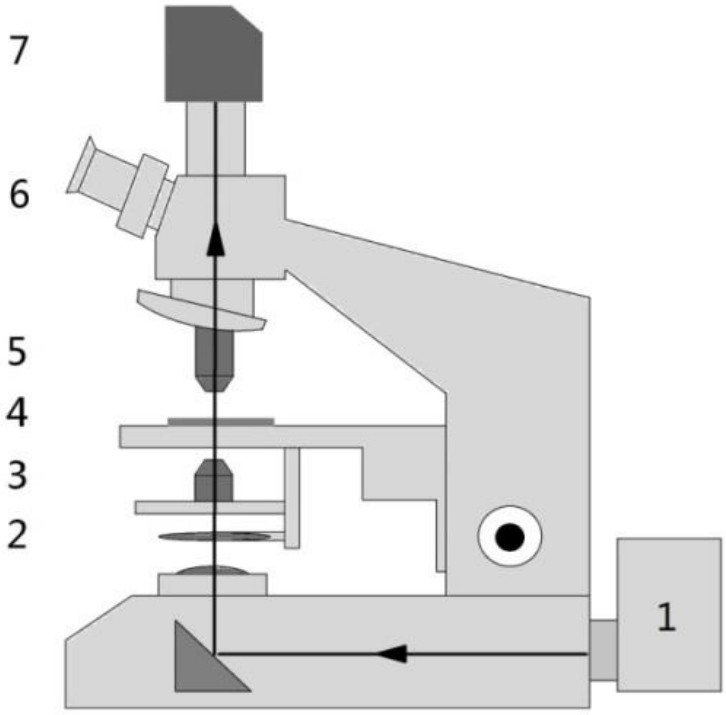

Figure 2.14, Schematic of optical transmission microscope with installed linear polariser. (1) Incident white light source. (2) Linear polariser. (3) Condenser lens. (4) Test sample clamped on the moveable stage. (5) Selected objective. (6) Eyepiece. (7) A CCD camera attached on top of the microscope. The black arrow line indicates the optical path of the incident and transmission light.

2.4 Conclusion

In this chapter, the necessary materials and relative nanofabrication processes for making subwavelength plasmonic structures have been described in detail. Simultaneously, optical characterisation methods including micro imaging and transmission spectrum analysis and numerical simulation techniques are presented. The procedures of molecule surface modification and detection by surface enhanced Raman spectroscopy have been presented. The working principles and operating conditions of equipment for device fabrication and characterisation have been explained.

Chapter 3 - Annular Aperture Arrays as Molecular Sensors

Abstract

Gold annular apertures arrays and circular apertures arrays were fabricated using e-beam lithography and various etching techniques. The plasmonic resonances of these arrays were measured using the spectrometer, and it was shown that their optical resonances can be manipulated from the visible to near infrared by altering the structural dimensions. Simulations of optical properties and resonant fields were carried out by using FDTD software. The annular aperture array as a promising substrate for surface enhanced Raman spectroscopy is demonstrated. A comparison of the Raman efficiency for these new structures against traditional circular aperture arrays is also presented.

3.1 Introduction

The discovery of extraordinary optical transmission (EOT) through subwavelength nano hole arrays in thin metal film [35] has resulted in the development of a variety of applications, including filters, [82, 143-145] photovoltaics, [146-148] and metamaterials. [149-151] In addition, plasmonic resonance with the associated electric field generated by the nano apertures makes these structures ideal for sensing applications such as SERS. So far, the commonly reported metallic nano aperture structures for SERS are limited to the simple circular holes, [105, 106, 152-154] even though they have an inherent disadvantage in low electric field enhancements. However, the potential of other subwavelength aperture arrays with complex geometries has yet to be fully recognized. Here, we proposed an array design which consists of annular apertures in gold thin film for the SERS application. Until now, extensive investigations into such annular aperture configurations still concentrate on the EOT phenomenon. Very few explorations about utilising the resonant field properties of such nanostructures have been conducted. According to the simulations, the annular configuration requires a smaller aperture size than that of the circular configuration in order to keep the same resonant wavelength. The smaller gap size of the annular configuration is able to generate a larger electric field, thus resulting in stronger

Raman scattering compared to the structures with circular apertures. However, if assuming both circular aperture and annular aperture arrays have the same metal thickness, the smaller gap of the annular aperture configuration means it has a higher structural aspect-ratio (defined as proportion of structure height to width), thus bringing difficulties in fabrication. Therefore, nearly all the reported annular aperture configurations were made by the focused ion beam (FIB) milling method. Here, a new approach for fabricating large gold annular aperture arrays has been specially developed. [155]

In this chapter, the surface plasmon resonance tunable properties of the circular aperture and annular aperture arrays are presented. The purpose of this set of experiments is not only to show the optical resonances of these structures can be manipulated but also to find out one circular aperture arrays and one annular aperture arrays where their resonant wavelengths can be tuned to match the excitation laser (633 nm) used in the SERS measurement. The above explorations are followed by two series of experiments regarding the use of SERS for molecular sensing. The first experiment was to compare the SERS performance of two annular aperture arrays, when the resonant wavelength of one annular aperture array was tuned to match the excitation laser (633 nm) while the other was in the mismatching condition. The next experiment was a comparison between one annular aperture array and one circular aperture array, where both of these two nanostructures were in the resonant state by using the same excitation laser (633 nm).

3.2 Materials

The materials used in this Chapter refer to Section 2.2 in Chapter two.

3.3 Methods

3.3.1 Fabrication of circular aperture arrays

Figure 3.1 shows the fabrication process for circular aperture arrays by using electron-beam lithography, inductively coupled plasma (ICP) deposition and reactive ion etching (RIE). A Pyrex glass substrate was firstly modified with a 140 nm Au layer, and then 200 nm silicon nitride was deposited as a mask layer. (For

the procedures of sample cleaning, metallization and nitride deposition refer to **Sections 2.3.3.1**, **2.3.3.2** and **2.3.3.3** respectively.) The sample was then spin coated with a 50 % diluted ZEP520A positive e-beam resist at 3000 rpm spinning speed, and oven baked to yield a 200 nm thickness, (**Fig.3.1.1**). Patterns of nano holes were generated on the resist layer after e-beam exposure and development, (**Fig.3.1.2**). The exposure dose was 520 μC/cm^2 and VRU was set to 6. (For the procedures of resist coating, e-beam lithography and resist development refer to **Sections 2.3.3.4**, **2.3.3.5** and **2.3.3.6** respectively.) After an O_2 plasma ash, nano hole patterns were transferred to the mask layer by nitride dry etching, the remaining resist was removed by O_2 plasma cleaning, (**Fig.3.1.3**). Ar plasma was applied to transfer the nano holes from the nitride layer into the Au layer underneath. Finally the mask layer was removed by nitride dry etching, leaving the complete Au circular aperture arrays, (**Figure 3.1.4**). (For the procedures of nitride dry etching, Au dry etching, and O_2 plasma ashing and cleaning refer to **Sections 2.3.3.7**, **2.3.3.8** and **2.3.3.9** respectively.)

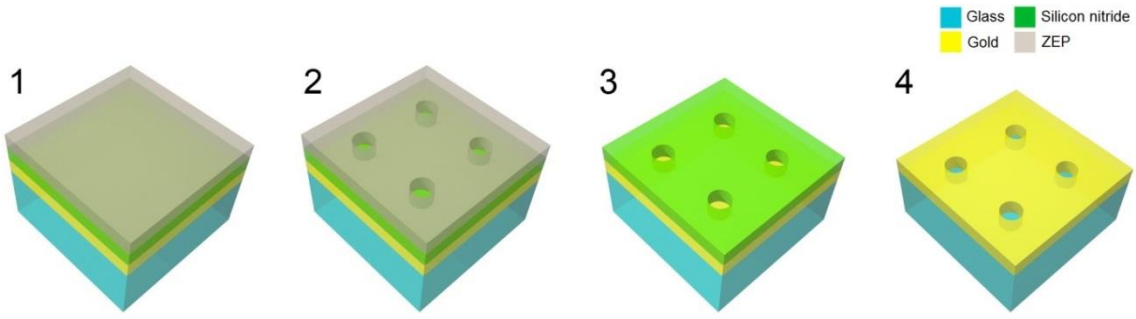

Figure 3.1, Fabrication of Au circular aperture arrays. (**1**) Sample preparation and resist coating. (**2**) Nano holes were generated on resist layer after e-beam exposure and development. (**3**) Nano holes were transferred to the nitride mask layer after nitride etching. (**4**) The complete Au circular aperture array was fabricated on glass after Au dry etching and nitride stripping.

3.3.2 Fabrication of annular aperture arrays

Figure 3.2 (a) shows the fabrication process of annular aperture arrays by using electron-beam lithography, inductively coupled plasma (ICP) deposition, reactive ion etching (RIE) and chemical wet etching. Pyrex glass substrate was firstly modified with 15 nm Au film as a conduction layer for the e-beam lithography. Then a 10 nm silicon nitride layer was deposited onto the sample as a resist adhesion layer. (For the procedures of sample cleaning, metallization and nitride

deposition refer to **Sections 2.3.3.1**, **2.3.3.2** and **2.3.3.3** respectively.) The sample was then spin coated with a neat HSQ negative e-beam resist with 3000 rpm spinning speed, and baked on a hotplate to yield a 500 nm thick layer, (**Fig.3.2 (a1)**). After e-beam exposure, resist development and low damage nitride etching, free standing ring-shaped pillars which consisted of resist and nitride were fabricated on the sample, (**Fig.3.2 (a2)**). Exposure dose was 3000 $\mu C/cm^2$ and VRU was set at 7. **Figure 3.2 (b)** and **(c)** show the SEM images of the ring-shaped pillars under top and tilted views respectively. (For the procedures of resist coating, e-beam lithography, resist development and low damage nitride etching refer to **Sections 2.3.3.4**, **2.3.3.5**, **2.3.3.6** and **2.3.3.7** respectively.) Then a 125 nm Au layer was deposited, (**Fig.3.2 (a3)**). A 50 nm PMMA layer was spun onto the sample before HF wet etching in order to protect the Au surface. The sample was then immersed in the HF solution to dissolve resist/nitride ring-shaped pillars. Finally, the exposed Au conduction layer, revealed after the HSQ removal, was removed using gold etchant, leaving the uniform 140 nm Au annular aperture array.

To achieve a successful wet etching, the most important step of this fabrication process is to make the sidewalls of ring-shaped pillars vertical to guarantee no metals were deposited on the sidewalls during gold evaporation (Refer to **Figure 3.2 (a2)** and **(a3)**). If the pillars are somewhat sloping, the gold will be deposited on it and act as a protect barrier to block the HF from dissolving the pillars. In that case, the gold on top of the pillars will connect to the gold on the array surface and be difficult to separate. **Figure 3.2 (d)** shows an example of annular apertures after such failure in wet etching. It is clear to see that many conglomerated gold fragments (white agglomerate) were stuck on the array surface.

This fabrication process also has some limitations in making annular apertures with other dimensions. For example, to make an annular aperture array with the gaps smaller than 20 nm, the resist after development must maintain the aspect-ratio of ~25:1 (assuming the resist thickness keeps the same). There is a very great difficulty for HSQ to keep such an ultrahigh aspect-ratio when the minimum dimensions are in tens of nanometers. Also, if annular apertures have small inner diameters but large aperture gaps, the central islands inside the

annular aperture may fall down during wet etching, and this can be seen in **Figure 3.2 (d)** as well. Through many trials, the process of fabricating annular apertures with a 30 nm gap was established.

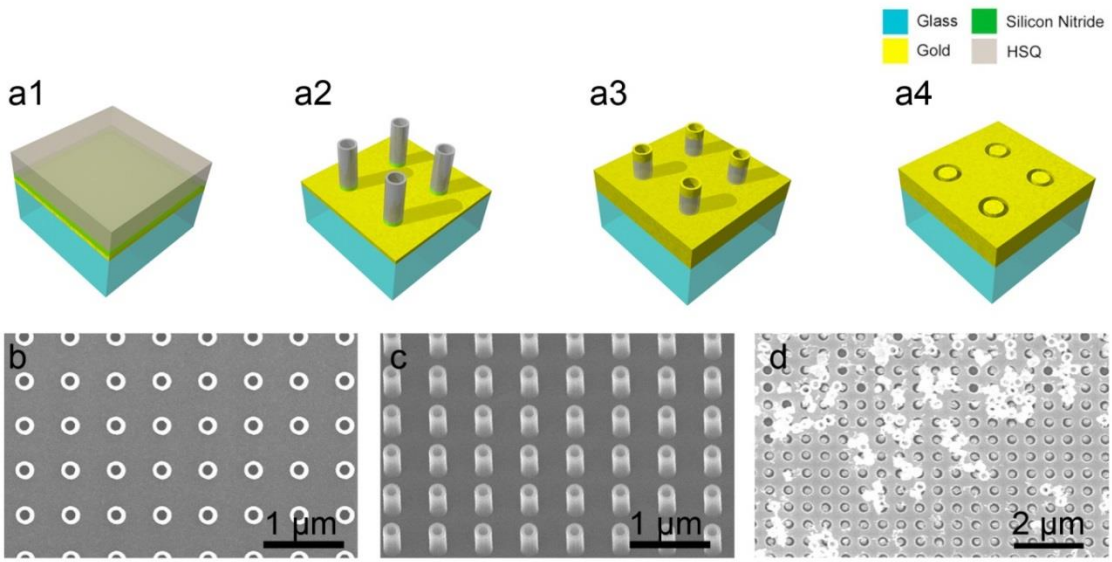

Figure 3.2, Fabrication of Au annular aperture arrays. (**a1**) Sample preparation and resist coating. (**a2**) Free standing ring-shaped pillars. (**a3**) Gold evaporation. (**a4**) Complete Au annular aperture array. The SEM images of free standing ring-shaped pillars from top view (**b**) and 30° tilted view (**c**) are presented. (**d**) An example of annular aperture array after a failure in the wet etching process.

3.3.3 Optical transmission spectra measurement

For measuring circular aperture arrays, the wavelength range was set in the visible from 400 nm to 750 nm. For measuring annular aperture arrays, the wavelength range was set from 400 nm to 2000 nm. The sampling interval was set at 1 nm. Other general procedures for the measurements can be found in **Section 2.3.3.12**.

3.3.4 FDTD simulations

Figure 3.3 shows the schematic of the simulation models. A 140 nm Au layer was defined from z=0 nm to z=140 nm. In **Figure 3.3 a**, a plane wave source was positioned at z=-400 nm and the direction of incident light was along the +z axis and a power monitor was positioned at z=1800 nm to record the optical spectra. In the second model as shown in in **Figure 3.3 b**, because in the SERS experiment a 633 nm laser directly shined to the sample surface, therefore, a

plane wave source was positioned at z=400 nm and the direction of incident light was along the -z-axis. A field monitor in the x-y plane was positioned at z=140 nm for visualising electric field distributions on the top surface. Another field monitor in the x-z plane was positioned at y=0 μm for visualising electric field distributions through the cross-section. For the circular aperture arrays, one circular cylinder was inserted into the gold layer to represent the circular aperture. For the annular aperture arrays, one annular cylinder was inserted into the gold layer to represent the annular aperture. Details of the simulation methods can be found in in **Section 2.3.1**.

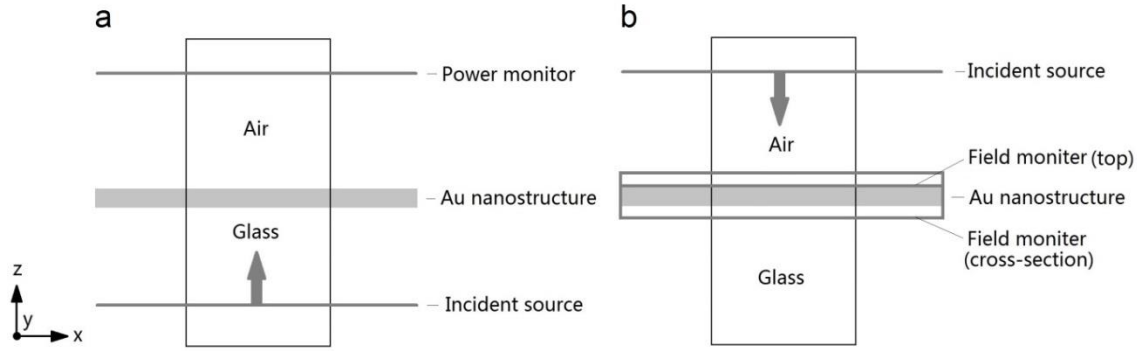

Figure 3.3, Schematic of the simulation models for the Au circular aperture and annular aperture arrays. (**a**) Schematic of the model for the spectra simulation. (**b**) Schematic of the model for the resonant field simulation. The arrow indicates the propagation direction of the incident light and the area enclosed in the rectangle represents the simulation space.

3.3.5 SERS of 4-MBA using a 633 nm laser

The SERS measurements of the first comparison between two annular aperture arrays were performed by using the Horiba Jobin Yvon LabRam INV spectrometer. A 50×, 0.55 NA objective was used. The diameter of focused laser spot was ~1.4 μm. Five repeated measurements were carried out in random positions of each array. The SERS measurements of the second comparison between one annular aperture array and one circular aperture array were performed by using the Horiba Jobin Yvon LabRam HR800UV spectrometer. A 20×, 0.4 NA objective was used. The diameter of focused laser spot size was ~2 μm. Eleven repeated measurements were carried out in random positions of each array. Other general procedures of the SERS measurement can be found in **Section 2.3.3.15**.

3.4 Results and discussions

3.4.1 Tunable plasmonic resonances of circular aperture arrays

As mentioned above, the extraordinary optical transmission and plasmonic activities of circular aperture arrays have been intensively studied and various applications related to this nanophotonics phenomenon have been reported. The objective of this section is not only for demonstrating the optical tuneable properties of circular aperture arrays, but also to find one such array whose optical resonance matches the 633 nm laser used in the Raman spectrometer. Two groups of experiments were carried out. The first was to investigate the effects of the array period on the plasmonic resonance. Three arrays (array A, B and C) were fabricated for this test. All three arrays kept the same hole diameter but the array period was changed. Another four arrays (array D, E, F and G) were fabricated as the second group which was to investigate the effect of structural dimensions on plasmonic resonance. For these arrays, hole diameters and the corresponding array periods were increased by the same proportion. All of these circular aperture arrays (A-G) were fabricated 600 μm^2 in area and the optical transmission spectra were normalized in order to give a clear indication of the resonant wavelength of each array.

3.4.1.1 Effect of array period on the resonance

Figure 3.4 shows the SEM images of circular aperture arrays A, B and C. These three arrays kept the same hole diameter of 240 nm, but their array periods were 460 nm, 500 nm and 540 nm respectively.

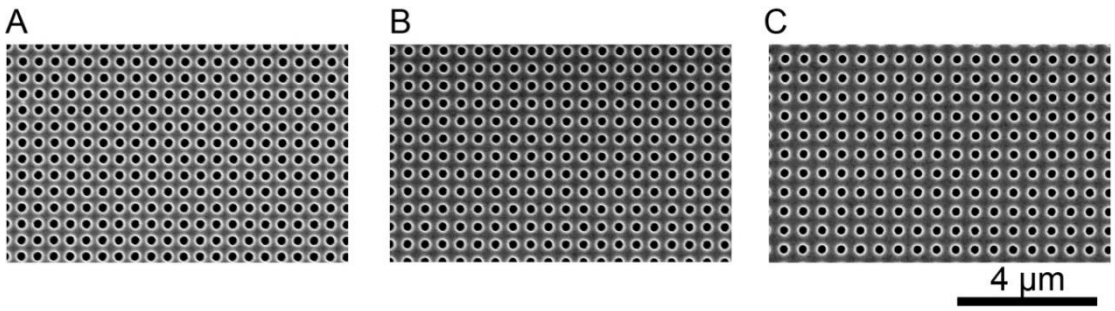

Figure 3.4, SEM images of the circular aperture arrays A, B and C. The diameters of these three arrays were the same as 240 nm (with a standard deviation was 5 nm), and the period of array A was 460 nm, of array B was 500 nm, of array C was 540 nm (the corresponding standard deviations were 3 nm, 4 nm and 3 nm respectively). Twenty circular apertures had been randomly chosen for calculating dimensional errors.

Figure 3.5 shows the experimentally measured (**Fig.3.5 (a)**) and numerically calculated (**Fig3.5 (b)**) plots of the normalized transmission spectra of circular aperture arrays A, B and C. As mentioned above, the characterisation range was in the visible from 400 nm to 750 nm. The measured resonance peak of array A was at 602 nm, of array B was at 633 nm, and of array C was at 662 nm respectively. This resonance peak experienced a 60 nm shift to a longer wavelength (from 602 nm to 662 nm) as a result of a 80 nm increment in array period (from 460 nm to 540 nm). The corresponding simulated resonance peaks of arrays A, B and C were 614 nm, 647 nm and 680 nm respectively.

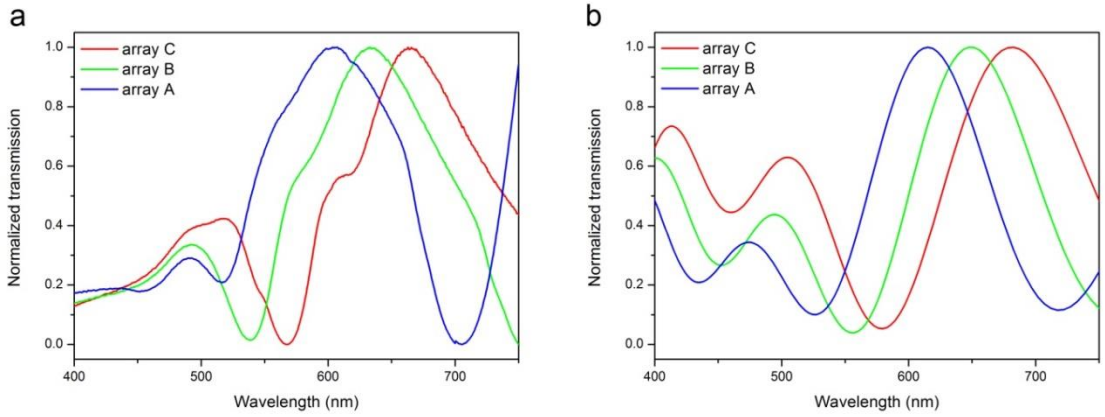

Figure 3.5, Normalized transmission spectra of circular aperture arrays A-C. (**a**) Measured spectra. (**b**) Simulated spectra. Both measured and simulated wavelengths were in the range 400 nm to 750 nm.

Figure 3.6 shows the dispersion relationships of plasmonic resonance (peak wavelength) with respect to array period of circular aperture arrays A, B and C. The extraordinary optical transmission through subwavelength apertures is determined by the surface plasmon resonance excitation and interference from adjacent apertures. In this set of experiments, the diameters of the apertures were identical, therefore, plasmonic resonances of such nano hole arrays can be attributed to the change of array period, thus altering the optical interference condition. More specifically, with increasing the array period, the light with longer wavelength generates constructive interference at exits of apertures, thus exhibiting the red-shift of the resonances.

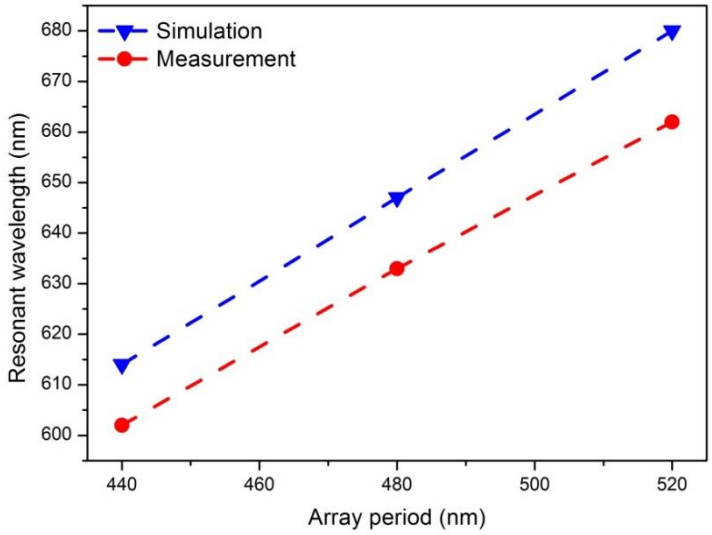

Figure 3.6, Dispersion relationships of plasmonic resonance with array period of the circular aperture arrays A-C. The measured and simulated data are drawn with red and blue markers respectively.

3.4.1.2 Effect of structural diameter/period on the resonance

Except for varying array period, structural dimensions also play an important role in shifting the plasmonic resonance. To demonstrate this, four circular aperture arrays (D, E, F and G) were fabricated and characterised. The diameters of the holes and array periods of these four arrays were increased by the same proportion. **Figure 3.7** shows the SEM images of arrays D-G. Array D had a diameter of 160 nm and period of 400 nm, array E had a diameter of 200 nm and period of 500 nm, array F had a diameter of 220 nm and period of 550

nm, and array F had a diameter of 240 nm and period of 600 nm. Although both the diameter and period increased, the ratio of the diameter to period of these four arrays was kept constant at 0.4.

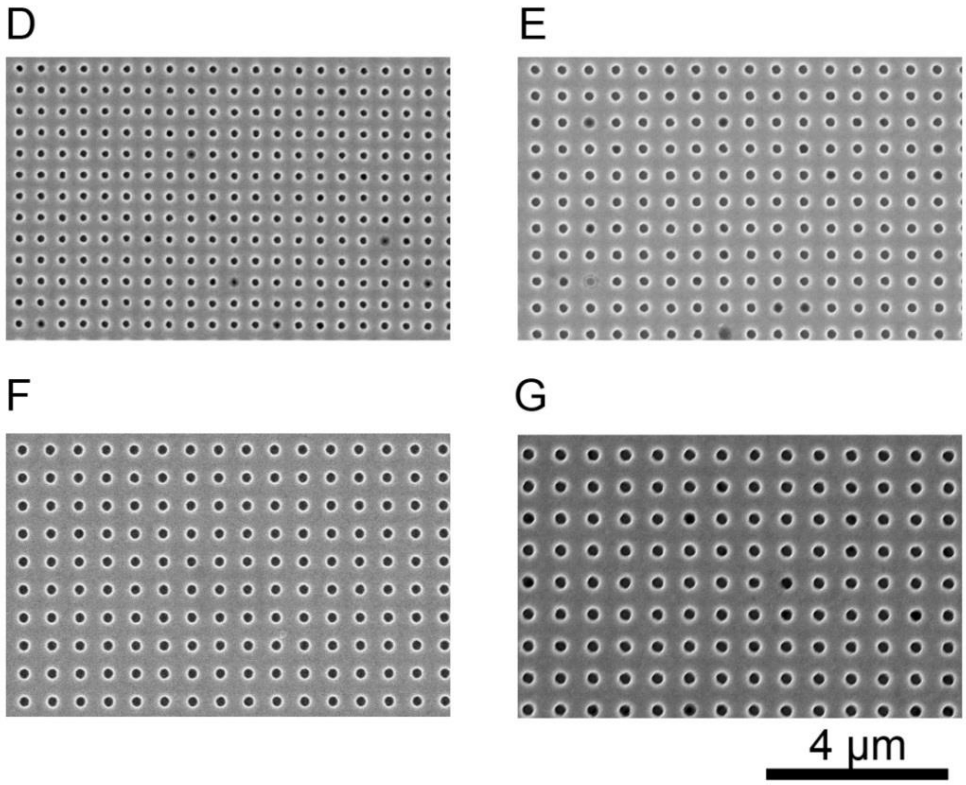

Figure 3.7, SEM images of circular aperture arrays D, E, F and G. The hole's diameter and array period were: 160 nm and 400 nm for array D (the corresponding standard deviations were 4 nm and 5 nm), 200 nm and 500 nm for array E (the corresponding standard deviations w 5 nm and 3 nm), 220 nm and 550 nm for array F (the corresponding standard deviations were 4 nm and 3 nm), and 240 nm and 600 nm for array G (the corresponding standard deviations were 3 nm and 3 nm). Twenty circular apertures had been randomly chosen for calculating dimensional errors.

Figure 3.8 shows both the experimentally measured and numerically calculated plasmonic activities of the arrays D-G. Spectra were characterised and normalized from 400 nm to 750 nm. The measured resonance peaks occurred at 544 nm for array D, at 595 nm for array E, at 638 nm for array F, and at 670 nm for array G. The corresponding resonant wavelengths in the simulations were at 565 nm, 650 nm, 698 nm and 745 nm respectively. As mentioned above, during the fabrication structural deformations are inevitable and these are one reason for the differences in spectra between the measurements and simulations. While,

with improving the structural quality and uniformity, such disparity can be reduced. [70]

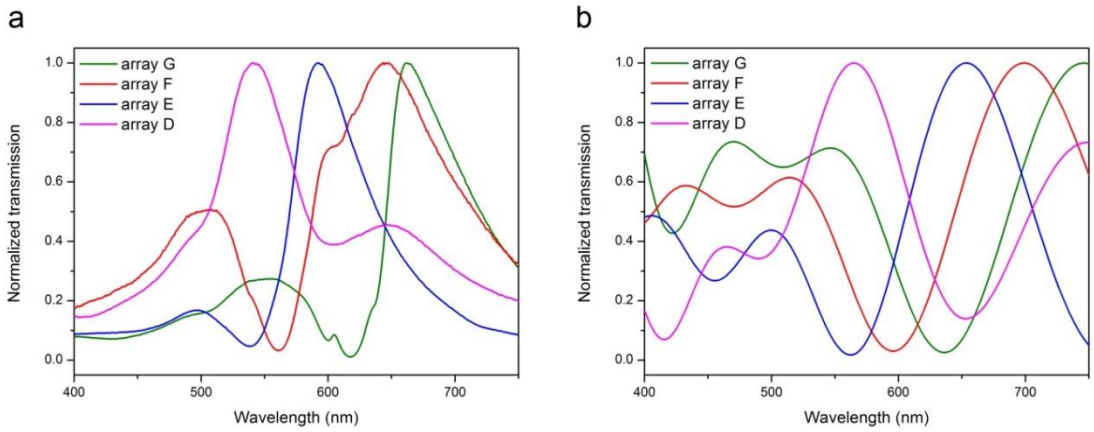

Figure 3.8, Normalized transmission spectra of circular aperture arrays D-G. (**a**) Measured spectra. (**b**) Simulated spectra. Both measured and simulated wavelengths were in the range 400 nm to 750 nm.

Figure 3.9 shows the dispersion relationships of plasmonic resonance (peak wavelength) with respect to the diameter (or array period) of the circular aperture arrays D-G. The resonant wavelength exhibited an over 100 nm red-shift as a consequence of a 80 nm increment in diameter (the corresponding increment in period was 200 nm) progressing from array D to G. In this series of experiment, both the aperture diameter and array period affect the resonant condition. With increasing the hole's diameter, the coupled plasmonic resonance varies, and the cut-off wavelength of the circular aperture moves to the longer wavelength range as well. All these result in the red-shift of the resonant wavelength. Together with the increment in array period, the resonances of these nanostructures presented such red-shift tendency although the ratio of diameter to period was kept the same.

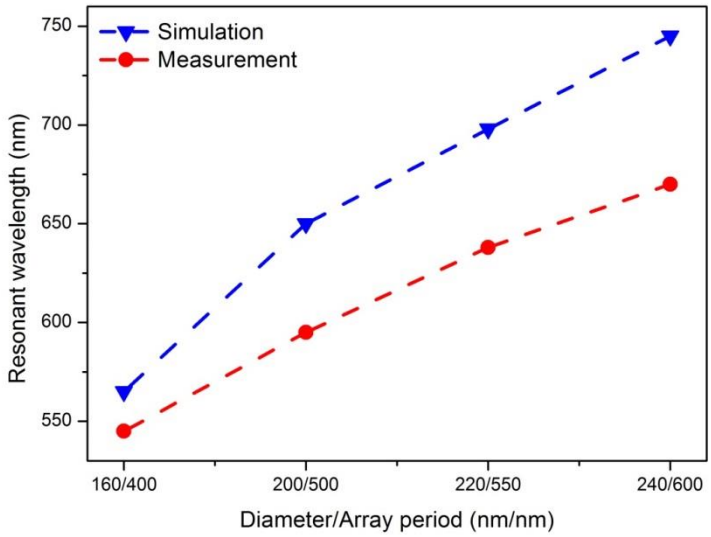

Figure 3.9, Dispersion relationships of plasmonic resonance with the diameter (period) of the circular aperture arrays D-G. The measured and simulated data are drawn with red and blue markers respectively.

Once again, it is necessary to point out here that the characterisations of circular aperture arrays discussed above are not comprehensive explorations of the plasmonic tunable properties of such nanostructures. And the characterised range was still limited to the visible range. In fact, for the resonance tunability of the circular aperture configurations, a large number of investigations have been done, where the effects of hole's diameter, array period, metal thickness and different metals have been discussed in a detail. [156, 157] Nevertheless, through the demonstrations presented above, circular aperture array F was found to have an optical resonant wavelength matching 633 nm (the excitation laser used in Raman spectrometer). Therefore, this array can be used for a comparison with an annular aperture array (which had the same array period as circular aperture array F) and was able to be excited to a resonant state by a 633 nm laser.

3.4.2 Tunable plasmonic resonance of annular aperture arrays

To investigate how plasmonic activities of annular aperture arrays varied by altering their structural dimensions, two groups of experiments were carried out. The first group included four annular aperture arrays (A-D) which had identical ring dimensions but different array periods. Another six arrays (E-J) were

fabricated as the second group to explore the effect of ring dimensions on the plasmonic resonance, while the array periods were kept constant. All the transmission spectra were measured from the visible to near infrared. However, the purposes of these studies not only focus on the optical tunable properties of such annular aperture structures but also need to find out one array where its resonant wavelength is able to match 633 nm which is the wavelength of the laser used in the Raman spectrometer. Such an array is under the "on" resonant state when excited by a 633 nm laser, while other arrays (with different resonant wavelengths) are under the "off" resonant state. All of these annular aperture arrays (A-J) were fabricated 600 μm^2 in area and the optical transmission spectra were normalized in order to clearly show the tuning of the surface plasmon resonance.

3.4.2.1 Effect of array period on the resonance

Figure 3.10 shows the SEM images of annular aperture arrays A-D. The annular apertures in these four arrays had the same geometrical size where the outer and inner diameters were 170 nm and 230 nm respectively. The array periods were 400 nm for array A, 450 nm for array B, 500 nm for array C, and 600 nm for array D. The gap of the ring aperture was ~30 nm (with standard deviation 3 nm). As can be seen in the SEM images, some tiny fragments were stuck inside the aperture in array A and B. The reason for that was partially due to the small distance between the annular apertures (or the higher array density). In other words, the higher structural density prevented the metals set on top of the models dissipating during wet etch process, thus resulting in some metal scraps falling into the annular apertures. Nevertheless, such small blockers did not affect the corresponding plasmonic resonances very much. This was not a problem for the arrays which had relatively larger periods, where the surface topography of the annular apertures shown in arrays C and D were much cleaner than that of arrays A and B.

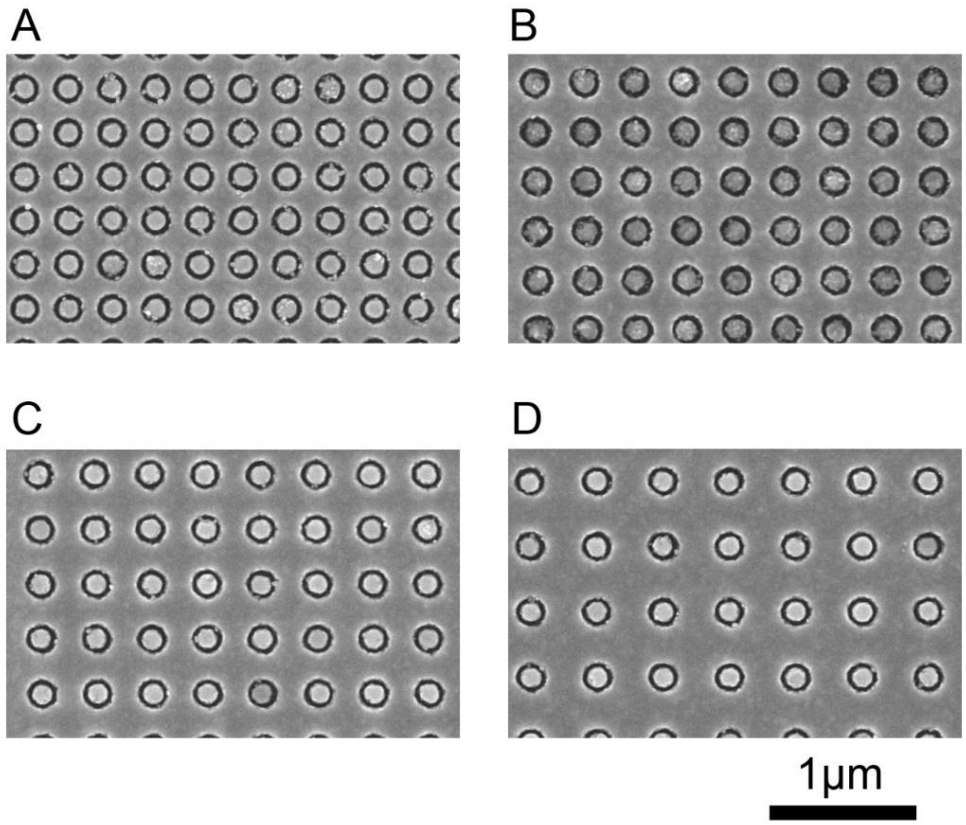

Figure 3.10, SEM images of annular aperture arrays A, B, C and D. For all these arrays, the inner diameter of the annular aperture was 170 nm (with a standard deviation was 3 nm), the outer diameter of the ring was 230 (with a standard deviation was 5 nm). The period was 400 nm for array A, 450 nm for array B, 500 nm for array C and 600 nm for array D (the corresponding standard deviation was 4 nm, 5 nm, 5 nm and 3 nm respectively). Twenty annular apertures had been randomly chosen for calculating dimensional errors.

Figure 3.11 shows plots of measured and simulated optical transmission spectra for arrays A-D. The measured and simulated spectra were both characterised from 400 nm to 2000 nm and normalized in intensity. In the measured spectra (**Fig.3.11 (a)**), the two almost vertical drops which appeared for arrays B and C in the range from 893 nm to 896 nm were due to the grating changing in the spectrometer. This caused the intensity of the incident light to be unstable at these wavelengths. The measured resonance peak was at 855 nm for array A, at 930 nm for array B, at 980 nm for array C and at 1035 nm for array D and the corresponding simulated peaks at 990 nm, 1033 nm, 1068 nm and 1100 nm for arrays A-D (**Fig.3.11 (b)**). It can be observed that the resonance peak trended to shift to shorter wavelengths as the array period decreased. All these characterisations show that the resonant wavelengths are dependent on the

array period. Therefore, an effective way of tuning the plasmonic resonances of the annular aperture arrays is by changing the array period.

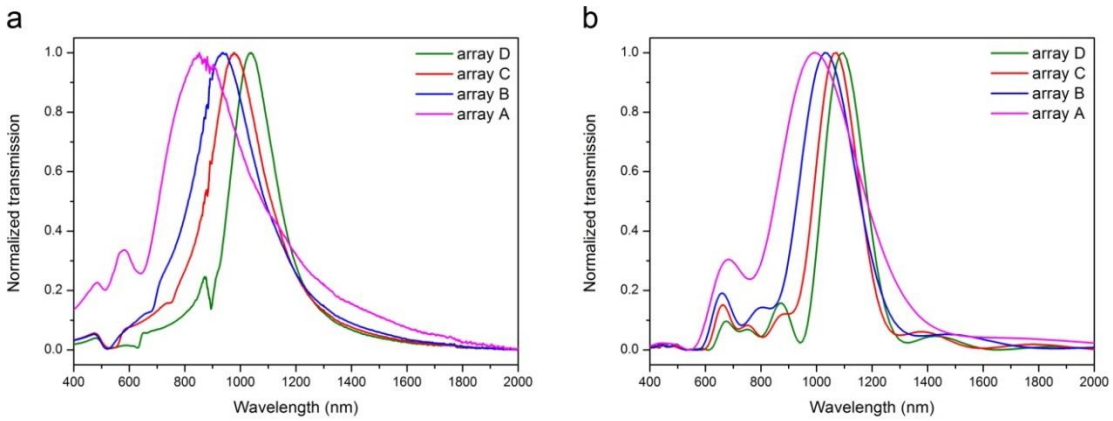

Figure 3.11, Normalized transmission spectra of annular aperture arrays A-D. (**a**) Measured spectra. (**b**) Simulated spectra. Both measured and simulated wavelengths were in the range 400 nm to 2000 nm.

Figure 3.12 shows the dispersion relationships of plasmonic resonance (peak wavelength) with respect to array period for annular aperture arrays A-D. Compared to the dispersive behaviours of circular aperture arrays, a similar red-shift tendency of the resonant wavelength appeared among these annular aperture arrays. According to experimental results, a 200 nm increase in structure period led to a 180 nm shift in transmission peak progressing from array A to D. When array period increased from 400 nm to 500 nm, there was a 125 nm red-shift in resonant peak as shown in arrays A and C, when the period continued to increase to 600 nm, there was only a 55 nm red-shift in the resonance which can be seen in arrays C and D. As discussed in **Section 3.4.1.1**, the increment in array period alters the interference condition at exits of apertures and resulting in a resonant wavelength red-shift. For these annular apertures with different array period as shown above, the resonance shift was a consequence of planar surface plasmons (PSPs) excitation due to the periodic arrangement of the apertures. [54] The coupling field travels along the structural surface evanescently with different propagating length on both sides of the apertures, leading to the shift in optical transmission.

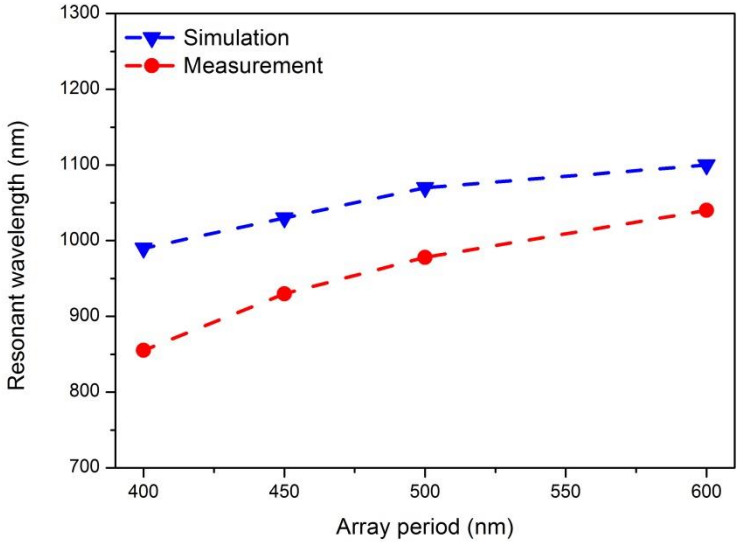

Figure 3.12, Dispersion relationships of plasmonic resonance with array period of annular aperture arrays A-D. The measured and simulated data are drawn with red and blue markers respectively.

3.4.2.2 Effect of diameter on the resonance

Although plasmonic resonance of annular aperture arrays can be manipulated by changing period, the dimensions of annular apertures such as the outer and inner diameters also affect the resonant wavelength. In order to explore the effect of the aperture dimensions on the plasmonic resonance, another six annular aperture arrays were fabricated. **Figure 3.13** shows the SEM images of annular aperture arrays E-J. The inner and outer diameters of the apertures in these arrays increased progressing from arrays E to J, while the aperture gap was fixed at ~30 nm and the array periods were identical as 550 nm. The inner/outer diameters were 90/150 nm for array E, 140/200 nm for array F, 170/230 nm for array G, 190/250 nm for array H, 210/270 nm for array I and 230/290 nm for array J. It was found that the larger structural dimensions resulted in smaller structural deformation. In array E, some ring apertures look darker than others. This was largely due to the residual resists and polymers on the structural surface. In array J, two irregular holes appeared at the bottom right of the image. These were probably caused by some defects arising during the wet etching process.

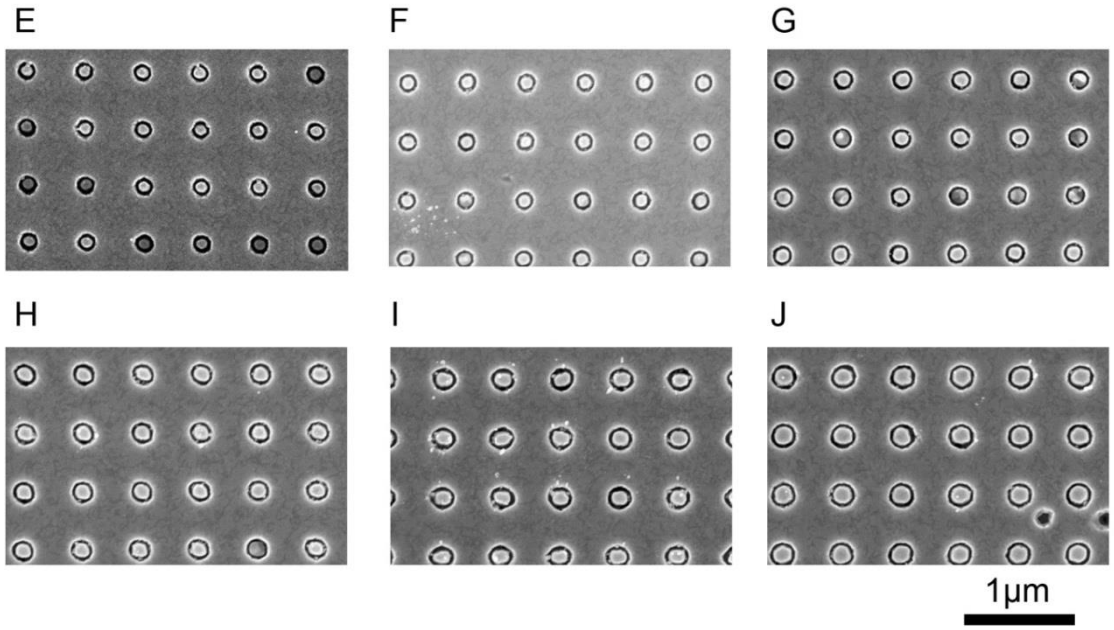

Figure 3.13, The SEM images of annular aperture arrays E-J. The inner and outer diameters of array E were 90 nm and 150 nm (the corresponding standard deviations were 5 nm and 5 nm), of array F were 140 nm and 200 nm (the corresponding standard deviations were 4 nm and 5 nm), of array G were 170 nm 230 nm (the corresponding standard deviations were 3 nm and 5 nm), of array H were 190 nm and 250 nm (the corresponding standard deviations were 4 nm and 3 nm), of array I were 210 nm and 270 nm (the corresponding standard deviations were 5 nm and 7 nm), and of array J were 230 nm and 290 nm (the corresponding standard deviations were 5 nm and 4 nm). The array period of these arrays were identical as 550 nm with standard deviation 4 nm. Twenty annular apertures had been randomly chosen for calculating dimensional errors.

Figure 3.14 (a) and **(b)** show the measured and simulated transmission spectra of annular aperture arrays E-J respectively. The characterisation wavelength was from 400 nm to 2000 nm and all spectra were normalized in intensity. The measured peak wavelength was at 630 nm for array E, at 823 nm for array F, at 886 nm for array G, at 897 nm for array H, at 950 nm for array I and at 1095 nm for array J. It is clear to see that with increasing the structural diameters the resonant wavelength is shifted from the visible to the near infrared. The simulation results also verified such a trend of spectra shifting. As shown in **Figure 3.14 (b)**, the peak wavelengths of arrays E to J progressing sequentially was 700 nm, 970 nm, 1070 nm, 1153 nm, 1240 nm and 1314 nm. The simulation models only reflected a very ideal condition that the all structural dimensions were perfect. However, in reality, due to the structural deformations in the diameters, and variations of array period and some defects and impurities

introduced during fabrication, there are certain kinds of mismatching between the measured data and the corresponding simulation results.

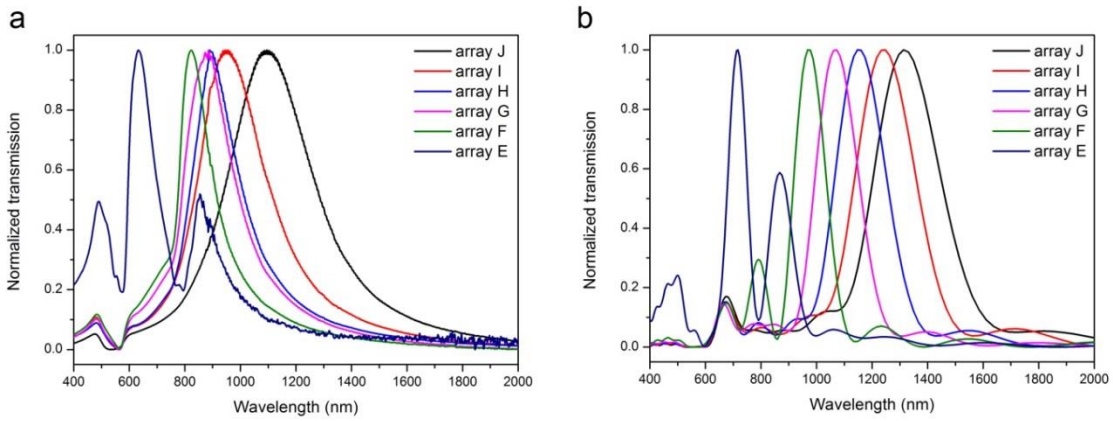

Figure 3.14, Normalized transmission spectra of annular aperture arrays E-J. (**a**) Measured spectra. (**b**) Simulated spectra. Both measured and simulated wavelengths were in the range 400 nm to 2000 nm**.**

Figure 3.15 shows the dispersion relationships of the resonant wavelength with respect to the structural diameters (inner and outer) of arrays E to J. When the inner diameter increased from 90 nm to 230 nm, and the outer diameter increased from 150 nm to 290 nm, the measured peak wavelength showed a red-shift of a 465 nm (increasing from 630 nm to 1095 nm). The simulation results also verify such resonance tunability. Due the identical array period, the resonance shift of arrays E to J was attributed to the variation in the aperture dimension. The field excited by the periodic structure channels through the annular aperture which is able to support cylindrical surface plasmons (CSPs) Such CSPs propagate along the interface inside the aperture from the entrance to the exit. In this case, the annular aperture is like a waveguide, therefore the propagating surface mode inside the aperture is dependent on dimensions of the aperture. Similar to the circular aperture, with the increment in the aperture size, the cut-off wavelength of the annular waveguide increases. This leads to the wavelength red-shift of the resonant guided mode inside the annular aperture. [48, 53]

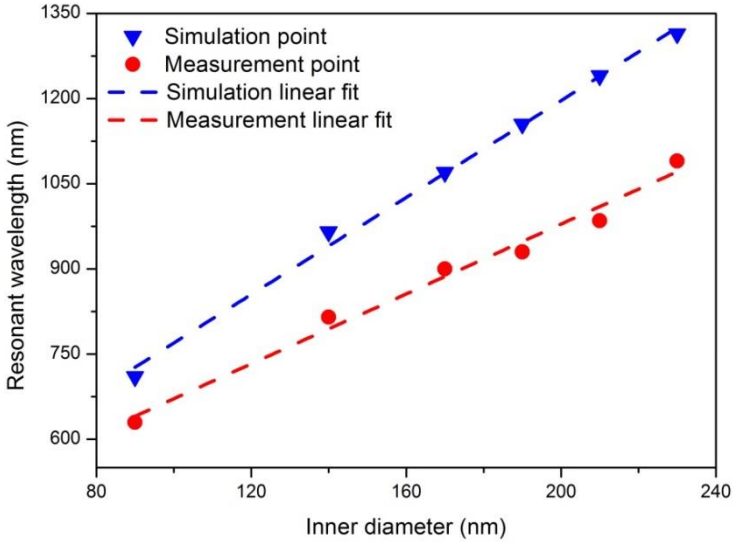

Figure 3.15, Dispersion relationships of plasmonic resonance with diameter (inner) of the annular aperture arrays E-J. The measured and simulated data are drawn with red and blue markers respectively. The dashed lines show the linear fitted results from each data point.

Through the spectral characterisations of these two groups, it is demonstrated that when increasing array period or structural diameter, the resonant wavelengths exhibit a red-shift and can be tuned from the visible to the near infrared. These two groups of experiments did not include all the parameters which affect the structural resonant conditions. For example, due to the limitation of the fabrication process, it is difficult to make a series of annular aperture arrays with diameters below 300 nm as well as keeping a large gap size (>60 nm), therefore, only the annular apertures with a 30 nm gap size were discussed in this chapter. The examples of tunable resonance of annular aperture arrays are to demonstrate that such structural resonant wavelength can be tuned to some specific wavelength (e.g. 633 nm) for various applications. For example, among all these annular aperture arrays, only array E has the plasmonic resonance (630 nm) closest to 633 nm, which is the wavelength of Raman excitation laser. Therefore, array E can be selected as a potential candidate for SERS. Detailed discussions related to SERS can be found in following sections.

3.4.2.3 Effects of deformations of annular aperture on the resonances

Deformations of annular apertures are inevitable during the fabrication. Therefore, it is necessary to study the effect of structural imperfection on the optical resonance. In this section, annular aperture array C was chosen as an example. The optical transmissions of several annular apertures with dimensional variations were simulated, which included the increase and decrease of array period (P), inner diameter (D_i) and outer diameter (D_o). The amounts of structural deformations were based on the error analysis of the annular array C. For a better comparison, the measured transmission of annular array C and the corresponding simulated spectrum without any deformations were plotted in the same graph.

Figure 3.16 (a) shows such measured and simulated spectra from 400 nm to 2000 nm and **Figure 3.16 (b)** shows the same spectra in a narrower wavelength range (900 nm to 1200 nm) to give a clear view of the peak wavelength of each spectrum. As mentioned before, the measured peak wavelength of annular aperture array C (shown in red) was at 980 nm and the simulation peak (without deformations) was at 1068 nm (shown in blue). However, for the array period with +5 nm (period 505 nm) and -5 nm (period 495 nm) deformations, the simulated peak appeared at 1074 nm and 1060 nm respectively. For the inner diameter with +3 nm (D_i 173 nm) and -3 nm (D_i 167 nm) deformations, the simulated peak was at 1096 nm and 1051 nm respectively. For the outer diameter with +5 (D_o 235 nm) and -5 nm (D_o 225 nm) deformations, the simulated peak was at 1061 nm and 1080 nm respectively. Although there were small variations (several nanometers) in structural dimensions, the resonance shift due to such deformations should be considered. Nevertheless, the purpose of the simulation is to give an overall guidance on the structure design rather than to give a precise predication of the resonant wavelength.

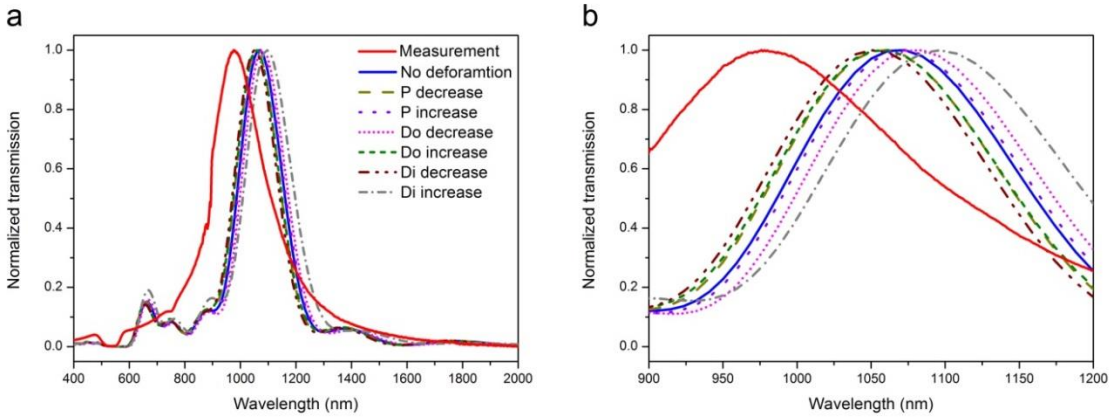

Figure 3.16, Normalized optical transmission spectra of annular aperture array C with and without structural deformations. (**a**) Spectra plotted in the wavelength range 400 nm to 2000 nm. (**b**) Spectra plotted in the wavelength range 900 nm to 1200 nm in order to give a clear view of the shift of peak wavelength.

3.4.3 Annular aperture arrays as molecular sensors based on SERS

Although a large variety of nanoparticle structures have been demonstrated to be effective for enhancing Raman scattering, [102, 104, 158-161] the electromagnetic field confinement and enhancement features of nano aperture structures enable them to be a novel alternative nanoengineered structure for SERS. These nanostructures can be used as the platform for molecular sensing. Due to the highly tunable plasmonic resonance of such nano apertures, one structure can be tuned to a specific wavelength to match the excitation laser of the Raman spectrometer. The condition when plasmonic resonance of one plasmonic nanostructure matches the wavelength of excitation laser is termed as the "plasmonic 'on' state", while the mismatching condition is termed as the "plasmonic 'off' state". As described before, two comparison experiments were carried out to demonstrate the applications of proposed gold annular aperture arrays in molecular sensing. For the first comparison (**Section 3.4.3.1**), Raman spectra were obtained from two annular aperture arrays at their respective plasmonic "on" and "off" states relative to the 633 nm excitation laser. For the second comparison (**Section 3.4.3.2**), Raman spectra were obtained from an annular aperture array and a circular aperture array both at their plasmonic "on" states under the 633 nm excitation laser.

3.4.3.1 SERS of 4-MBA on two annular aperture arrays

To compare the SERS performances of the annular aperture arrays under the resonant matching and mismatching conditions, annular aperture array E and annular aperture array I were chosen as test samples. The plasmonic resonance of array E (630 nm) was closest to the 633 nm excitation laser while the resonant wavelength of array I (950 nm) was far enough removed from the 633 nm laser line. In this case, array E was in the plasmonic "on" state, and array I can be seen as being in the plasmonic "off" state. **Figure 3.17** shows the simulated electric field distributions of array E and array I under the 633 nm excitation. **Figure 3.17 (a1)** and **(a2)** show the top view (in the x-y plane) and cross-section view (in the x-z plane) of array E respectively while **Figure 3.17 (b1)** and **(b2)** show the corresponding views of array I

As shown in the top views, annular aperture array E generated the maximum electric field of 240 V/m at the aperture edges, and the field enhancement in the centre of the aperture was still larger than 70 V/m. However, for annular aperture array I, the largest field which appeared at the edges was just over 70 V/m and the minimum field in the centre of the ring was 25 V/m. The electric fields distributed along the x-axis symmetrically, because the incident polarisation was set parallel to the x-axis in the simulations, and the maximum field area appeared at edges of the aperture when the coordinate in y-axis was 0. From the cross section views, it is clearly seen that annular aperture array E generated the strongest electric fields at the top surface (the air/gold interface), and only small fields appeared at the bottom surface (the glass/gold interface) with a strength ~80 V/m. In contrast, for annular aperture array I, both of the top and bottom surfaces had some field enhancement but the overall intensities were still quite low, and the field minimum area in which almost no field enhancing took place occurred at z=70 nm (the middle of the aperture). Through the comparisons of field enhancement at 633 nm excitation, array E was able to generate the stronger electric fields, with the maximum field enhancing ratio over 3 times higher than that of array I. Therefore, it can be considered that annular aperture array E was at the plasmonic "on" state while annular aperture array I was at the plasmonic "off" state when excited by the 633 nm laser. The scale range in each figure was chosen as 0-100 V/m in order to give a better

visual effect for the comparison between the two fields rather than to show the actual highest and lowest fields.

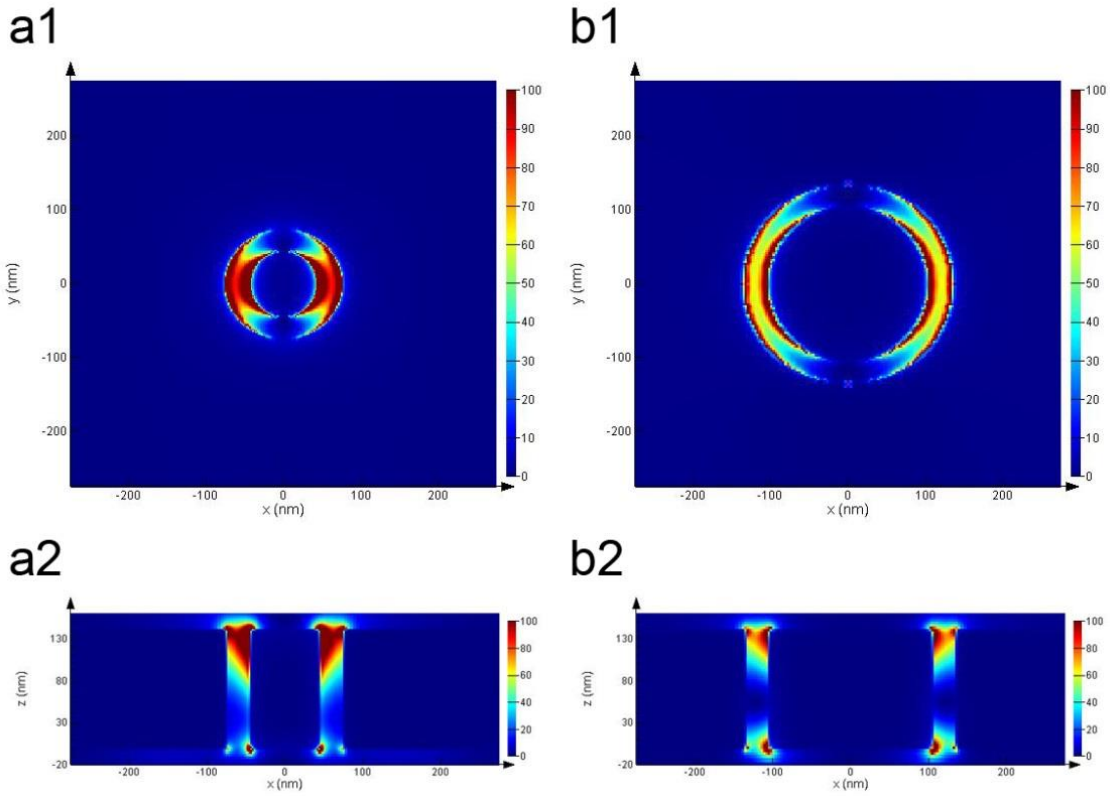

Figure 3.17, Plasmonic induced electric field enhancements at 633 nm of annular aperture arrays E and I. (**a1**) Top view of array E. (**a2**) Cross-section view of array E. (**b1**) Top view of array I. (**b2**) Cross-section view of array I.

Since the Raman scattering is proportional to the fourth power of the local electric field, [95] the calculated maximum Raman enhancements of annular aperture arrays E and I were ~$3x10^9$ and ~$2.4x10^7$ respectively. Therefore, these annular aperture configurations have great potential to be used in enhancing Raman scattering under the appropriate excitation. To demonstrate this assumption, 4-MBA was chosen as the target molecule for SERS due to its stable chemical properties, the thiol group guaranteeing that the molecules attached to the gold surfaces.

Figure 3.18 shows the 4-MBA Raman spectra of annular aperture arrays E and I respectively, as well as the spectrum from a flat gold surface as a reference. Five repeated measurements were carried out at random positions on each array. The error bar of 1580 cm^{-1} peak is shown in the inserted figure. For the annular

aperture array E, the average intensity was 3800 counts with standard deviation 333 counts. The corresponding average intensity of annular aperture array I was 734 counts with standard deviation 134 counts.

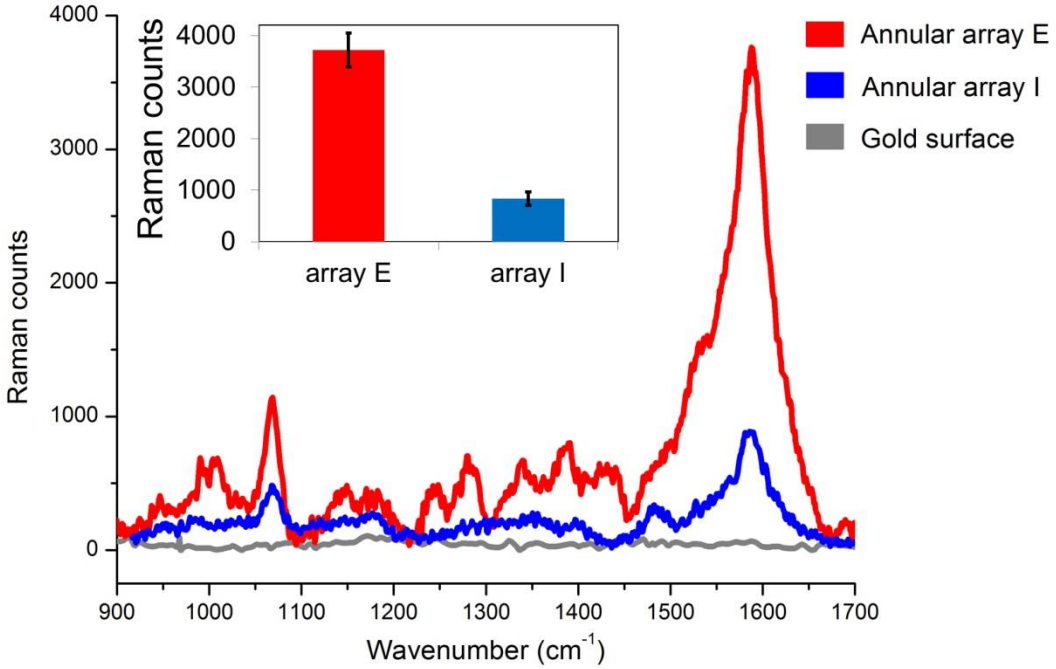

Figure 3.18, SERS spectra of 4-MBA attached to annular aperture arrays E and I under the 633 nm laser excitation. The Horiba LabRam HR800UV spectrometer was used for analysing the Raman signals and the acquisition time was 5 seconds for each measurement. Taking the 1580 cm^{-1} peak for comparison, annular aperture array E provided the largest Raman scattering, which was ~5 times higher than that of annular aperture array I. The reference spectrum was taken from the gold surface beside the test arrays. Before measurement, a piece of silicon was used to calibrate the spectrometer with the 520 cm^{-1} peak.

As expected, annular aperture array E (shown in red) represents a significant Raman scattering enhancement over annular aperture array I (shown in blue). There was no Raman scattering from a gold surface and only a randomly fluctuant spectrum was obtained due to the fact that there was no electric field enhancement on the bare gold surface. Two prominent peaks appeared at 1070 cm^{-1} and 1580 cm^{-1} which can be associated with the benzene ring breathing mode $\nu(CC)_{ring}$. [162, 163] For the 1070 cm^{-1} peak, the maximum Raman intensity of annular aperture arrays E and I were 1160 and 480 counts respectively. For the 1580 cm^{-1} peak, the average scattering intensity of annular aperture array E was 3800 counts. In contrast, annular aperture array I had an average value of

only 734 counts, this being over 5 times lower than that of array E. Moreover, on the spectrum of array E, some weak peaks appeared from 1132 cm^{-1} to 1357 cm^{-1} which indicated the presence of carbon-hydrogen bonds and the -COOH group. [154, 162] These peaks did not appear on the spectrum of array I. These results demonstrate that the resonant electric field excited by the annular apertures do not just provide strong Raman scattering but also contain more detailed spectral information.

One point worth emphasizing is that the Raman scattering spectra shown above were only collected from the surfaces covered by the laser spot. The laser diameter in this experiment was 1.4 μm as mentioned in **Section 3.3.5**, and the period of the two arrays used were the same at 550 nm. Based on this information, it can be calculated that only 5 annular apertures of each array were covered by the laser spot and participated in enhancing the Raman scattering. The surface area of annular aperture arrays E and I under the laser was estimated as 1.5 μm^2 and 1.4 μm^2 respectively. According to relevant research, the surface coverage of 4-MAB on gold surface is about 0.5 $nmol/cm^2$ (5×10^{-16} $mol/\ \mu m^2$). [162] Taking the Avogadro constant as 6.02×10^{23}, the number of molecules on annular aperture arrays E and I covered by the laser were ~4.5×10^8 and ~4.2×10^8 respectively. The array E contained 7% more molecules than that of array I, and after adjusting for this difference, the Raman intensity of array E was still 4.8 times larger than that of array I (the average intensity after adjusting of array E was 3534 counts). Therefore the Raman enhancement was not due to the greater number of the molecules but due to highly confined resonant fields. However, the enhance factor of the simulated results of the array E is much higher than that of the array I (over 100 times). This was due to the different laser beam profile in the real measurement and in the simulation model. In the simulation, the whole incident light was set to the normal incident condition (perpendicular to the apertures). While, in the experiment, due to the NA of objective lens cannot be infinite small, the actual profile of excitation laser looks like a cone rather than a plane wave. Therefore, only a small proportion of the incident light can be assumed as normal incident, thus resulting in the difference between the measurement and the prediction.

3.4.3.2 SERS of 4-MBA on a annular aperture array and a circular aperture array

This section presents the comparison of Raman spectroscopy between one annular aperture array and one circular aperture array. In order to guarantee both arrays can be excited in the resonant state by using the 633 nm laser, annular aperture array E (resonant wavelength at 630 nm) and circular aperture array F (resonant wavelength at 638 nm) were selected as test samples. The plasmon induced electric fields for each type of nano apertures (annular and circular) reach its own maximum level by the 633 nm laser excitation. In other words, these two arrays were both switched to the plasmonic "on" state by the 633 nm laser. **Figure 3.19** shows the simulated electric field distributions of annular aperture array E and circular aperture array F under the 633 nm excitation. **Figure 3.19 (a1)** and **(a2)** show the top view (in the x-y plane) and cross-section view (in the x-z plane) of the annular aperture array E respectively while **Figure 3.19 (b1)** and **(b2)** show the corresponding views of the circular aperture array F.

Although the resonant fields of annular aperture array E have been discussed in detail in **Section 3.4.3.1**, in order to give a clear comparison of the field distributions between annular aperture array E and circular aperture array F, in this section it is necessary to once again briefly summarize the electric field features of annular aperture array E as well as consider the electric fields of circular aperture array F. From the top views as shown, the maximum electric field supported by annular aperture array E was 240 V/m at the edges of the ring and the field in the centre of the ring was over 80 V/m. In contrast, the circular aperture array F had the electric field enhancement of 90 V/m at the edges of the hole and of only 9 V/m in the centre of the hole. The electric fields generated by the circular apertures were significantly less than those of the annular aperture, when both arrays were at the resonant condition. When comparing the field enhancements from the cross-section views, for annular aperture array E, the resonant fields were not just maximized at the top surface but were also distributed along the gold/air interface into the aperture along the z-axis with a gradual decrease in intensity. However, for circular aperture array F, the electric fields was only confined to the top surface and almost no

resonant fields were excited inside the hole, and although some field enhancement was observed at bottom surface, the intensity was still no more than 40 V/m. Through this comparison, the electric field of annular aperture array E was over 2.6 times greater than that of circular aperture array F when both of them were at the resonant condition. The scale range in each figure was chosen as 0-100 V/m in order to give a better visual effect for the comparison between the two fields rather than to show the actual highest and lowest fields.

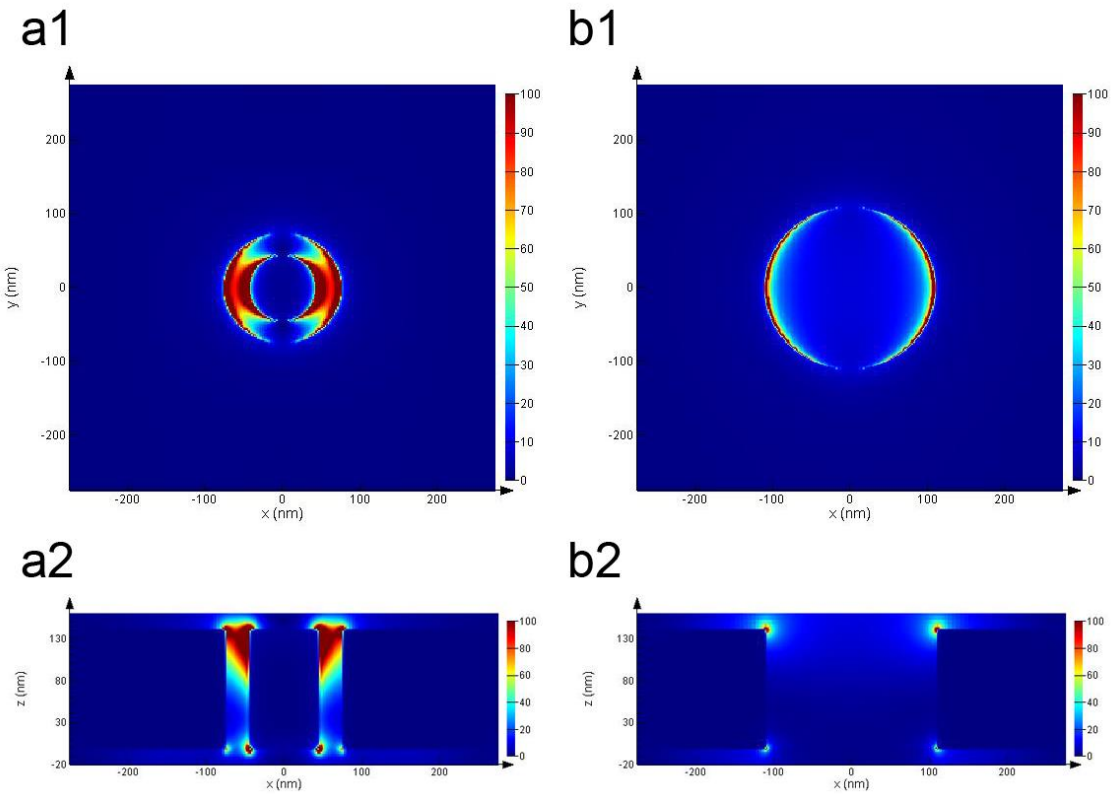

Figure 3.19, Plasmonic induced electric field enhancements at 633 nm of annular aperture array E and circular aperture array F. (**a1**) Top view of annular aperture array E. (**a2**) Cross-section view of annular aperture array E. (**b1**) Top view of circular aperture array F. (**b2**) Cross-section view of circular aperture array F.

The electric field values illustrate the significance of choosing an annular aperture array over a circular aperture configuration for the application of Raman spectroscopy. The corresponding maximum Raman enhancements of annular aperture array E and circular aperture array F was $3x10^9$ and $6.6x10^7$ respectively. To compare the SERS performance, these two nanostructures were modified with 4-MBA as a target molecule.

Figure 3.20 shows the 4-MBA Raman spectra of annular aperture array E and circular aperture array F, as well as the spectrum from a flat gold surface as a reference. Eleven repeated measurements were carried out at random positions on each array. The error bar of 1570 cm^{-1} peak is shown in the inserted figure as well. For the annular aperture array E, the average intensity was 8376 counts with standard deviation 590 counts. The corresponding average intensity of circular aperture array F was 1226 counts with standard deviation 78 counts.

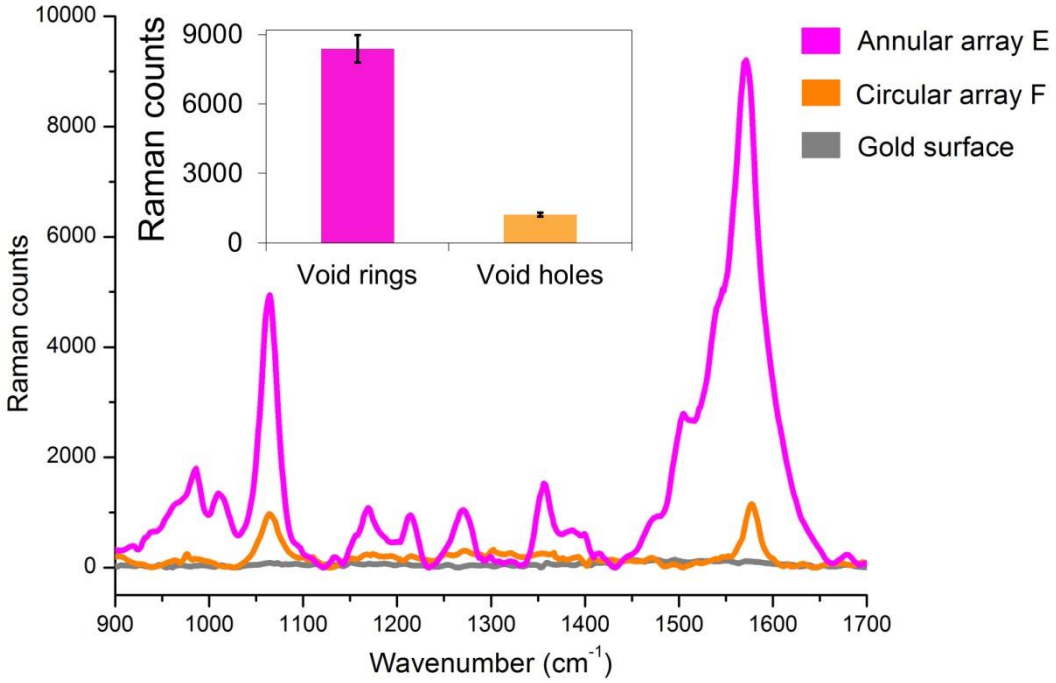

Figure 3.20, SERS spectra of 4-MBA attached to annular aperture array E and circular aperture array F under the 633 nm laser excitation. The Horiba LabRam INV spectrometer was used for collecting scattered Raman signals and the acquisition time was 5 seconds for each measurement. Taking the 1570 cm-1 peak for comparison, annular aperture array E provided the largest Raman scattering, which was almost 7 times higher than that of circular aperture array F. The reference spectrum was taken from the gold surface beside the test arrays. Before measurement, a piece of silicon was used to calibrate the spectrometer with the 520 cm^{-1} peak.

As can be seen, both the annular aperture and circular aperture arrays have demonstrated enhancement in Raman spectroscopy, but the overall intensities of Raman scattering provided by annular aperture array E (shown in magenta) was much higher than the commonly used circular aperture array F (shown in orange). In contrast, there was no Raman scattering at all from the reference

gold surface. As mentioned before, the two peaks at 1065 cm^{-1} and 1570 cm^{-1} in the graph were due to the benzene ring breathing mode $\nu(CC)_{ring}$. [162, 163] The maximum intensity of the peak at 1065 cm^{-1} was over 4970 counts from annular aperture array E, while for the circular aperture array F, the maximum level was only 992 counts. For the 1570 cm^{-1} peak, the maximum intensity of annular aperture array E was 9230 counts, which was 7.3 times greater than that of circular aperture array F (whose scattering intensity was 1266 counts). In addition, several weak peaks at 1173 cm^{-1}, 1215 cm^{-1}, 1285 cm^{-1} and 1357 cm^{-1} in the spectra of the annular aperture array E indicated the C-H bonds and -COOH group of the molecule. [154, 162] This detailed molecular information, however, can hardly be seen from the spectrum provided by the circular aperture array. The discussions above have shown that the electric field enhancement of annular apertures far exceeds the capability of a circular aperture. Therefore, although both of these two types of nanostructures were excited to their resonant state, the annular aperture array was able to generate the stronger Raman spectra as well as giving more detailed molecular information than that of the circular aperture array for equal exposure time.

In order to have a thorough understating of the interactions between Raman scattering and such nano aperture structures, it is worth knowing how many annular apertures or circular apertures are involved in the Raman enhancement. The laser diameter in this experiment was 2 μm as mentioned in **Section 3.3.5**, and both of the annular aperture and circular aperture arrays had the same period of 550 nm. Based on this information, it can be calculated that only nine apertures of each array were covered under the laser spot and participated in enhancing the Raman scattering. Through similar calculations to those in **Section 3.4.3.1**, it can be estimated that the number of molecules within the laser on annular aperture array E and circular aperture array F were ~9×10^{8} and ~8.2×10^{8} respectively. The annular aperture array E contained 9.7% more molecules than that of circular aperture array F, and after adjusting for this difference, the average Raman intensity of annular aperture array E (7563 counts) was still 6.2 times larger than that of array F. The difference in the enhance factor calculated from experimental data and simulation results was due to the different laser beam profile between actual measurement and simulation model. This has been discussed at the end of the previous section.

3.5 Conclusion

It has been demonstrated that various annular aperture arrays with different geometrical sizes were successfully produced via a specially developed fabrication process which combined e-beam lithography, plasma dry etching and chemical wet etching. By manipulating the geometrical sizes, the surface plasmon resonance of either circular aperture arrays or annular aperture arrays can be tuned within a certain wavelength range.

In the experiments where annular aperture arrays were used for SERS, the results showed that at the resonant state this structure can generate intense, highly confined electric fields with a significant increase in the Raman spectra. In the experiments where one annular aperture array and one circular aperture array were used for SERS, the void rings generated a Raman spectrum with maximum peak intensity over 7 times higher than that of the circular apertures while containing a great amount of information about the target molecule. This reiterated the powerful capability for electric field enhancement produced by this structure. Therefore, the proposed annular aperture array proved to be a highly sensitive structure for molecular interrogation.

Chapter 4 - Split-ring Shaped Aperture Arrays as Molecular Sensors

Abstract

Gold split-ring shaped aperture arrays were fabricated by using electron-beam lithography and etching techniques. The plasmonic resonant properties of these nanostructures were studied by analysing their optical transmission spectra which were obtained by a spectrometer. Through control of the structural dimensions such as the inner and outer diameters of the split-ring and the split-angles, it is possible to tune the resonant wavelength over a wide range. Due to the asymmetric nature of the split-ring, one single structure can generate two distinct plasmonic resonances which depended on the incident polarisation. By using an appropriate design, one of the resonant wavelengths of such a structure can be tuned to match the excitation laser in the Raman spectrometer and a resonant state can only be established when the structure is in a correct orientation. This allows the split-ring shaped aperture to be used for enhancing Raman scattering in a molecular sensor.

4.1 Introduction

As has been demonstrated in a previous chapter, the metallic nano aperture arrays not only exhibited unique properties in extraordinary optical transmission but also showed great capability in the resonant electric field enhancement which can be utilised in SERS for molecular sensing. Among the reported the results, nearly all of the nano aperture configurations which were used in SERS applications had symmetrically shaped apertures such as circular or annular holes. The resonant wavelengths of these structures are independent of the incident polarisation. In contrast, an asymmetric aperture possesses an incomparable advantage where its optical resonant wavelength is not only determined by structural dimensions but also is highly dependent on the polarisation direction of the incident light, thus enabling one single structure to be excited with two plasmonic resonances. When using appropriate structural dimensions, the resonance can be tuned to match the laser used in the Raman spectrometer, therefore, such asymmetric apertures can be upgraded to an

experimental platform for SERS. In fact, a large number of asymmetric nanoparticle configurations with their plasmonic properties have been shown to be usable for sensing applications. [104, 164-168] However, the possibility of the nanostructures with asymmetric apertures for SERS has rarely been studied. This is partially due to the difficulties in fabricating the apertures with complex shapes in gold or silver. Based on the specially developed fabrication process which has been shown in the previous chapter, the fabrication of arrays with complex apertures became a reality.

In this chapter, gold split-ring shaped apertures have been proposed and fabricated. To characterise their plasmonic properties, the corresponding optical transmission spectra of such nanostructures are studied from two aspects, both of which focus on the effect of structural dimensions on their optical resonances. Due to the structural resonances which are highly dependent on the incident polarisation, one resonant wavelength could be tuned to match the 633 nm laser and used for SERS, while the other is mismatched to 633 nm. Therefore, using one single structure only the correct orientation is able to obtain the Raman spectra which are produced from the molecules absorbed on its surface. Detailed discussion of using such a split-ring shaped aperture arrays for SERS is presented at the end of this chapter.

4.2 Materials

The materials used in this Chapter refer to Section 2.2 in Chapter two.

4.3 Methods

4.3.1 Fabrication of split-ring shaped aperture arrays

The fabrication process for making split-ring shaped aperture arrays was quite similar to that of making annular aperture arrays shown in the previous chapter, only changing the exposure patterns from the rings to split-rings. **Figure 4.1 (a1)**-**(a4)** show the fabrication process of split-ring shaped aperture arrays using electron-beam lithography and various etching techniques. **Figure 4.1 (a1)** shows the sample before e-beam exposure, this included gold and nitride depositions and resist coating. **Figure 4.1 (a2)** shows the profile of split-ring

pillar after development and nitride etching. **Figure 4.1 (a3)** shows the sample after gold evaporation. **Figure 4.1 (a4)** shows the complete split-ring shaped apertures after multi step wet etchings. The detailed fabrication process can be found in **Section 3.3.2**.

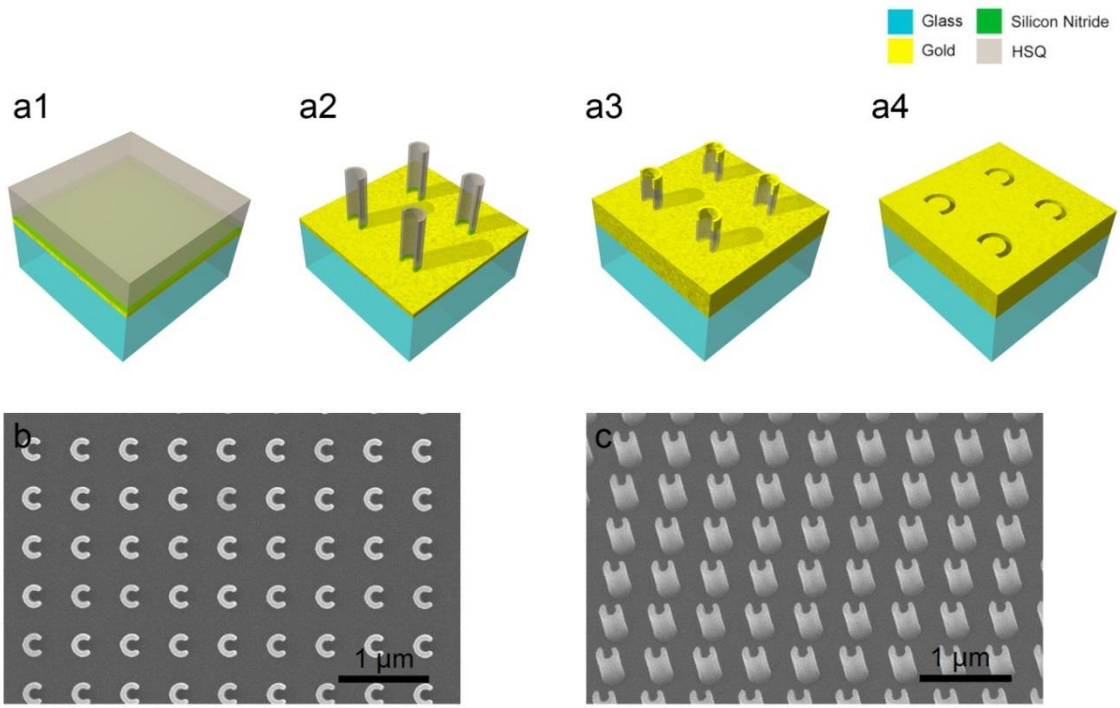

Figure 4.1, Fabrication of Au split-ring arrays. (**a1**) Sample preparation and resist coating. (**a2**) Free standing C-shaped (split-ring) pillars. (**a3**) Gold evaporation. (**a4**) Completed Au split-ring shaped aperture arrays. The SEM images of the developed resist profiles of C-shaped pillars from the top view (**b**) and 30° tilted view (**c**) are presented.

4.3.2 Optical transmission spectra measurement

For measuring the polarisation dependent transmission spectra of the split-ring shaped aperture arrays, the wavelength range was set from 400 nm to 2000 nm. The sampling interval was 1 nm and slit width was set at 8 nm. **Figure 4.2** shows the schematic of a split-ring orientation. During the measurement, the incident polarisation was fixed along the x-axis. For measuring the x-polarised transmission, the sample was placed in the orientation where the split opening was parallel to the x-axis, while for measuring the y-polarised transmission, the sample was then rotated 90° with its split opening parallel to the y-axis. The general measurement procedures can be found in **Section 2.3.3.12**.

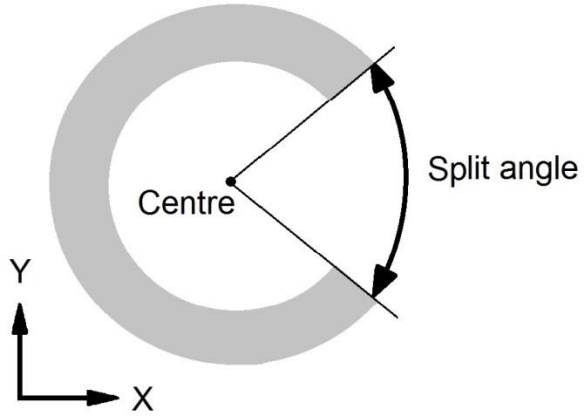

Figure 4.2, Diagram of a split-ring. The split-angle and x- and y- axes are indicated in the figure.

4.3.3 FDTD simulations

Figure 4.3 shows the schematic of the simulation models. These were quite similar to the models used in the previous chapter but the major difference was the aperture shape. In this chapter, the simulation models employed a split-ring shape aperture rather than a circular or annular shape aperture. In **Figure 4.3 a**, it shows the model diagram for the simulation of the transmission spectra. This was identical to the model shown in **Figure 3.3 a**. In **Figure 4.3 b**, it shows the model diagram for the simulation of the resonant field. The settings were almost the same as shown in **Figure 3.3 b**, however, the only difference was there were three field monitors in the x-y plane were positioned at z=140 nm, z=70 nm and z=10 nm for visualising the electric field distributions on the upper surface, in the middle of the aperture and at the bottom of the aperture respectively. Other general settings and detailed simulation method can be found in **Section 3.3.4** and **Section 2.3.1**.

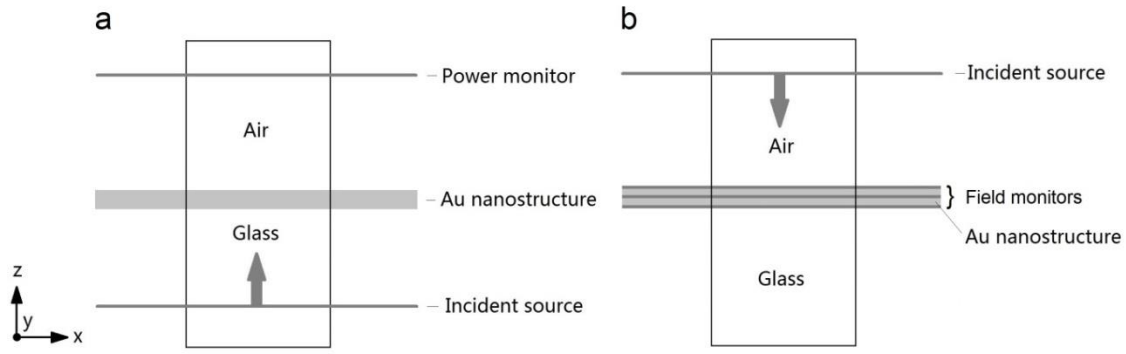

Figure 4.3, Schematic of the simulation models for the Au split-ring shaped aperture arrays. (**a**) Schematic of the model for the spectra simulation. (**b**) Schematic of the model for the resonant field simulation. The arrow indicates the propagation direction of the incident light and the area enclosed in the rectangle represents the simulation space.

4.3.4 Polarization dependent SERS of 4-MBA using a 633 nm laser

The polarisation dependent SERS measurement of one split-ring shaped aperture arrays was performed by using the Horiba Jobin Yvon LabRam HR800UV spectrometer. A 20×, 0.4 NA objective was used. The diameter of focused laser spot was ~2 μm. Five repeated measurements were carried out in random positions on the array. A linear polariser was first used to confirm the polarisation direction of the incident laser. Then, the test sample was aligned with its split opening parallel and perpendicular to the incident polarisation to measure the Raman spectra under different polarisation conditions. The measurements range was 900-1700 cm^{-1} and the acquisition time of each measurement was set at 5 seconds. Other general procedures of the SERS measurement can be found in **Section 2.3.3.15**.

4.4 Results and discussions

4.4.1 Tunable plasmonic resonances of split-ring shaped aperture arrays

As mentioned above, the plasmonic resonance of split-ring shaped aperture arrays is determined by either the structural dimensions or incident polarisation. In this section, the two studies of the tunable resonance properties of such nanostructures were carried out. For the first study, four split-ring shaped aperture arrays (A-D) were fabricated and characterised. These four arrays had the same array period, aperture width and split-angle, but their diameters

varied. For the second study, three split-ring shaped aperture arrays (C, E and F) were examined. The diameters, aperture width and array period were kept the same, but the split-angle varied. For both groups, the optical transmission spectra of each array were measured at different polarisation states.

4.4.1.1 Effect of structural diameter on the resonances

Figure 4.4 shows the SEM images of split-ring shaped aperture arrays A-D. As can be seen, the split openings were orientated along the same direction and this was along the x-axis. These four arrays had the same array period of 480 nm, split-angle of 90^{o}, and aperture gap of ~30 nm. The corresponding inner and outer diameters of array A were 105 nm and 165 nm, of array B were 135 nm and 195 nm, of array C were 165 nm and 225 nm, and of array D were 195 nm and 255 nm.

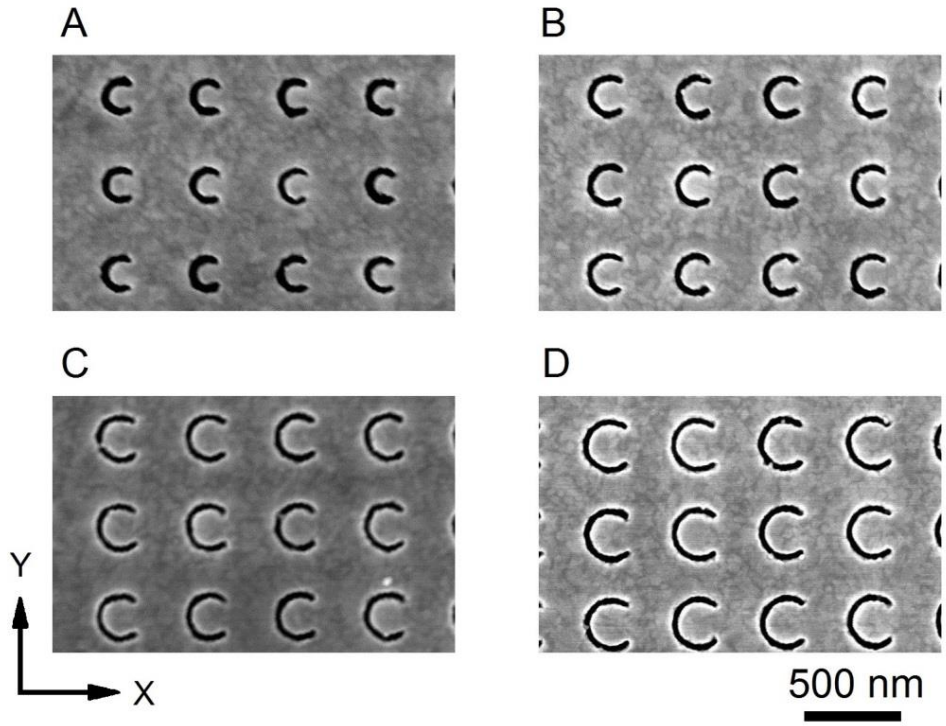

Figure 4.4, SEM images of split-ring shaped aperture arrays A-D. Array A had inner and outer diameters of 105 nm and 165 nm respectively (the corresponding standard deviations were 6 nm and 5 nm). Array B had the inner and outer diameters of 135 nm and 195 nm respectively (the corresponding standard deviations were 5 nm and 5 nm). Array C had the inner and outer diameters of 165 nm and 225 nm respectively (the corresponding standard deviations were 3 nm and 4 nm). Array D had the inner and outer diameters of 195 nm and 255 nm respectively (the corresponding standard deviations were 3 nm and 2 nm). The array period was constant at 480 nm (with a standard deviation was 3 nm) and the split angle was 90^{o} for all these arrays. The aperture width was 30 nm (with a standard deviation was 5 nm). Ten split-ring apertures had been randomly chosen for calculating dimensional errors. The x- and y-axes are indicated in the figure.

Figure 4.5 shows the experimentally measured and numerically simulated transmission spectra of split-ring shaped aperture arrays A-D under the x-polarisation state. All the spectra were normalized in order to clearly show the resonant wavelength. The measured peak wavelength of the plasmonic resonance of array A was at 1200 nm, of array B was at 1480 nm, of array C was at 1740 nm, and of array D was at 1945 nm. The corresponding simulation results of these arrays was 1223 nm for array A, 1440 nm for array B, 1670 nm for array C and 1939 nm for array D. Once again, the structural deformations and dimension variations may have caused the difference between the measured and

simulated results. But the overall tendency of the resonant spectra shifting along with the increment in structural diameters was demonstrated. It also can be seen that the optical transmissions of these arrays under the x-polarisation state were in the wavelength range of 1-2 μm which is the near infrared.

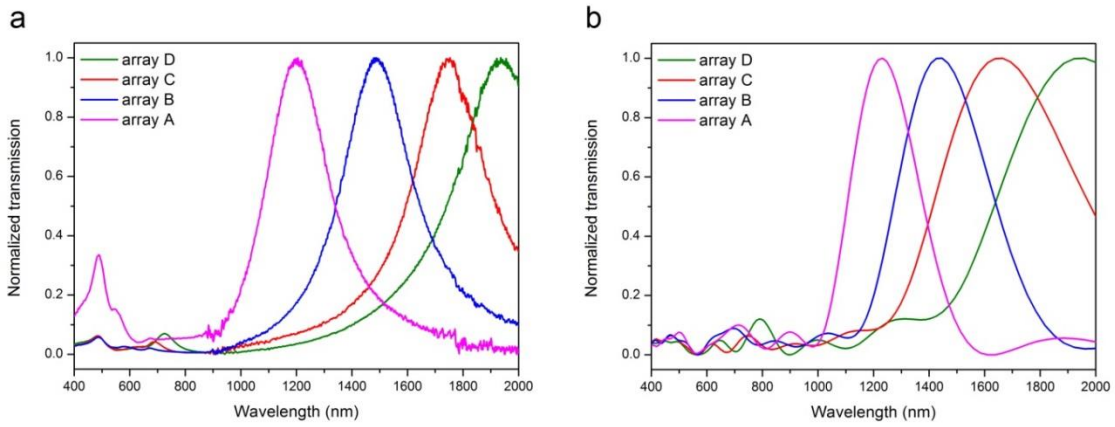

Figure 4.5, Normalized transmission spectra of split-ring shaped aperture arrays A-D at the x-polarisation state. (**a**) Measured spectra. (**b**) Simulated spectra. Both measured and simulated wavelengths were in the range 400 nm to 2000 nm.

Figure 4.6 shows the experimentally measured and numerically simulated transmission spectra of split-ring shaped aperture arrays A-D under the y-polarisation state. All the spectra were normalized in order to clearly show the resonant wavelength. The measured resonant wavelength was 670 nm for array A, 740 nm for array B, 826 nm for array C, and 895 nm for array D. The corresponding simulation results of were 660 nm for array A, 783 nm for array B, 878 nm for array C, and 981 nm for array D. The transmission band of these arrays in the y-polarisation state occurred in the shorter wavelength range (from visible to near infrared (<1 μm)) compared to the transmissions at x-polarisation state. The resonant peak in the y-polarisation state exhibited a similar red-shift tendency as the structures were in the x-polarisation state when the diameters were increased.

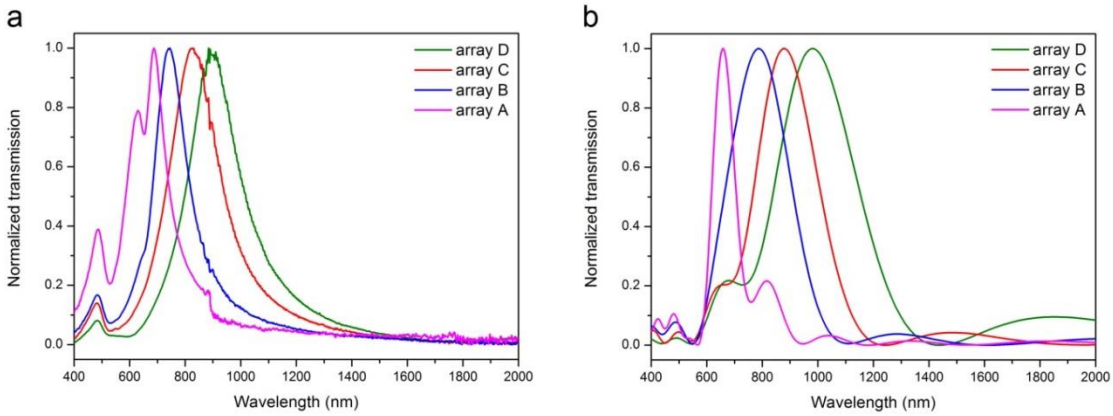

Figure 4.6, Normalized transmission spectra of split-ring shaped aperture arrays A-D at the y-polarisation state. (**a**) Measured spectra. (**b**) Simulated spectra. Both measured and simulated wavelengths were in the range 400 nm to 2000 nm.

Figure 4.7 (a) and **(b)** show the dispersion relationships of plasmonic resonance (peak wavelength) with respect to the inner diameter of split-ring shaped aperture arrays A-D at the x-polarisation and the y-polarisation states respectively. For the x-polarised transmission, it can be seen that with a 90 nm increment in the inner diameter from array A to D, the measured resonant wavelength showed a 740 nm red-shift. Meanwhile, the outer diameters of each array increased correspondingly and the aperture gaps were kept as a constant at ~30 nm. For the y-polarised transmission, with the same increment in diameters, a 225 nm red-shift of the optical resonance can be observed. Such a tendency of these dispersion relations was also verified by the simulation results. Although in both polarisation states, the plasmonic resonance exhibited a red-shifting as the diameters increased, a larger shift was generated at the x-polarisation state than at the y-polarisation state.

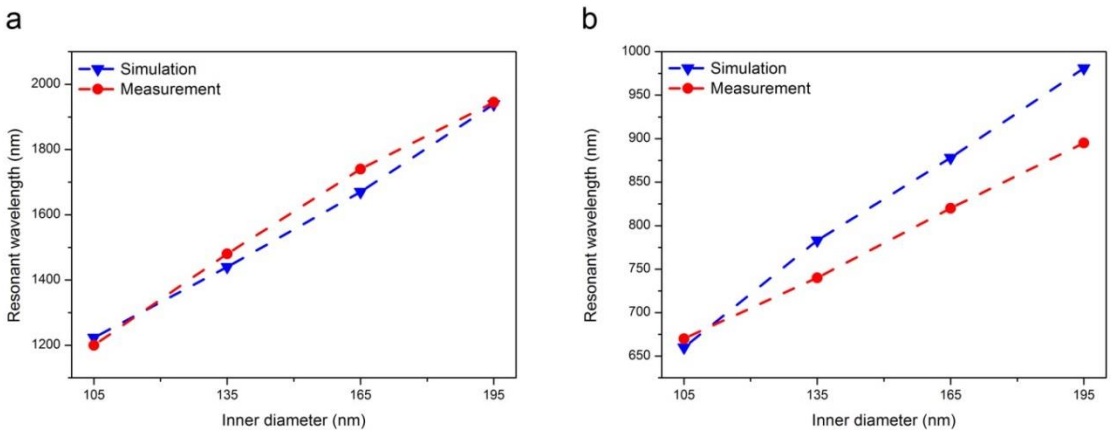

Figure 4.7, Dispersion relationships of plasmonic resonance with inner diameter of the split-ring shaped aperture arrays A-D. (**a**) Dispersion relationships of the resonance with inner diameter of the test arrays at the x-polarisation state. (**b**) Dispersion relationships of the resonance with inner diameter of the test arrays at the y-polarisation state. The measured and simulated data are drawn with red and blue markers in each figure respectively.

As explained in the previous chapter, the nano apertures as a grating coupler firstly excite surface plasmon resonances, and then surface waves with proper wavelengths are able to propagate along the aperture due to its waveguide effect. These processes are dependent on the aperture's shape and dimension. However, for this split-ring shaped aperture, which can be seen as adding a discontinuity part into the symmetric annular aperture. This disruption in the aperture varies the coupling energy and waveguide mode for the incident light with different polarization (parallel or perpendicular to the aperture disruption), resulting in different resonant wavelength.

4.4.1.2 Effect of split angle on the resonances

Figure 4.8 shows the SEM images of split-ring shaped aperture arrays C, E and F. These three arrays had the same structural diameters (inner 165 nm and outer 225 nm), array period (480 nm) and aperture width ~30 nm. However, the split-angle of array C was 90^{o}, of array E was 140^{o} and of array F was 180^{o} respectively. The split openings of each array were orientated along the same direction along the x-axis.

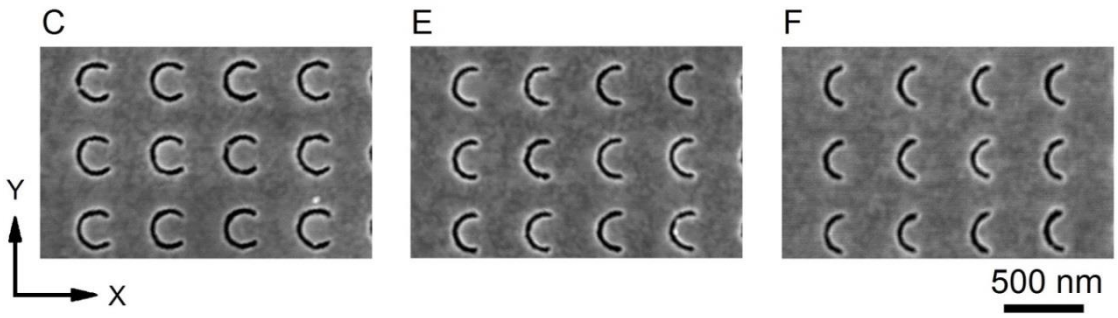

Figure 4.8, SEM images of split-ring shaped aperture arrays C, E and F. For the split-ring, the inner diameter was 165 and the outer diameter was 225 nm (the corresponding standard deviations were 3 nm and 4 nm respectively). The period of all these arrays was the same at 480 nm (with a standard deviation was 5 nm). Ten split-ring apertures had been randomly chosen for calculating dimensional errors. The split-angle increased from 90° in array C, to 140° in array E, and finally to 180° in array F.

Figure 4.9 shows the experimentally measured and numerically simulated transmission spectra of split-ring shaped aperture arrays C, E and F under the x-polarisation state. All the spectra were normalized in order to clearly show the resonant wavelength. The measured peak wavelength of the plasmonic resonance of array C was 1740 nm, of array E was 1405 nm, and of array F was 1140 nm. The corresponding simulation results of these arrays was 1670 nm for array C, 1432 nm for array E, and 1210 nm for array F. It can be seen that optical resonances of these three arrays were in the near infrared where the peak wavelengths were in the range 1-2 μm. In addition, as the split-angle increased, the resonant wavelength showed a blue-shift tendency.

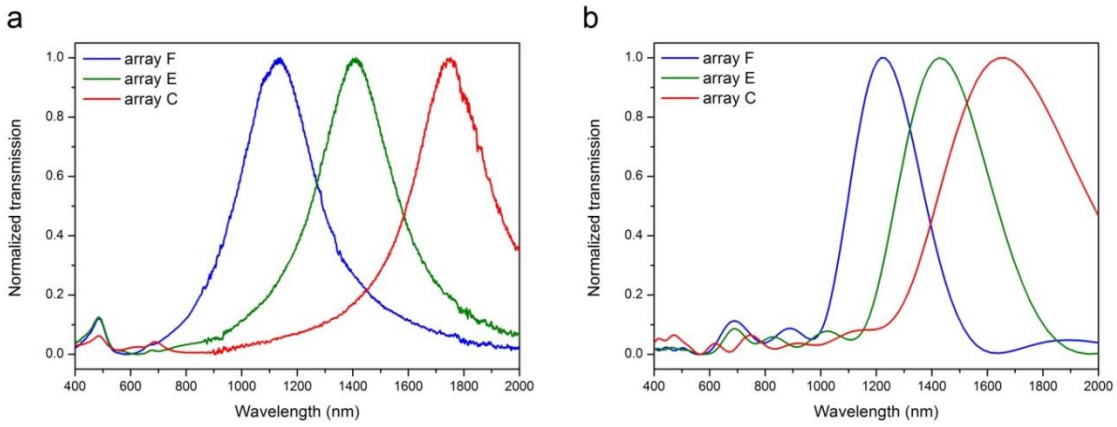

Figure 4.9, Normalized transmission spectra of split-ring shaped aperture arrays C, E and F at the x-polarisation state. (**a**) Measured spectra. (**b**) Simulated spectra. Both measured and simulated wavelengths were in the range 400 nm to 2000 nm.

Figure 4.10 shows the experimentally measured and numerically simulated transmission spectra of split-ring shaped aperture arrays C, E and F under the y-polarisation state. All the spectra were normalized in order to clearly show the resonant wavelength. The measured resonant wavelength was 820 nm for array C, 720 nm for array E, and 668 nm for array F. The corresponding simulation results were 875 nm for array C, 760 nm for array E, and 698 nm for array F. At the y-polarisation condition, the optical transmissions were almost in the visible range and a similar blue-shift tendency can be observed when the split-angle increased from 90^{o} to 180^{o} when compared to the x-polarisation state.

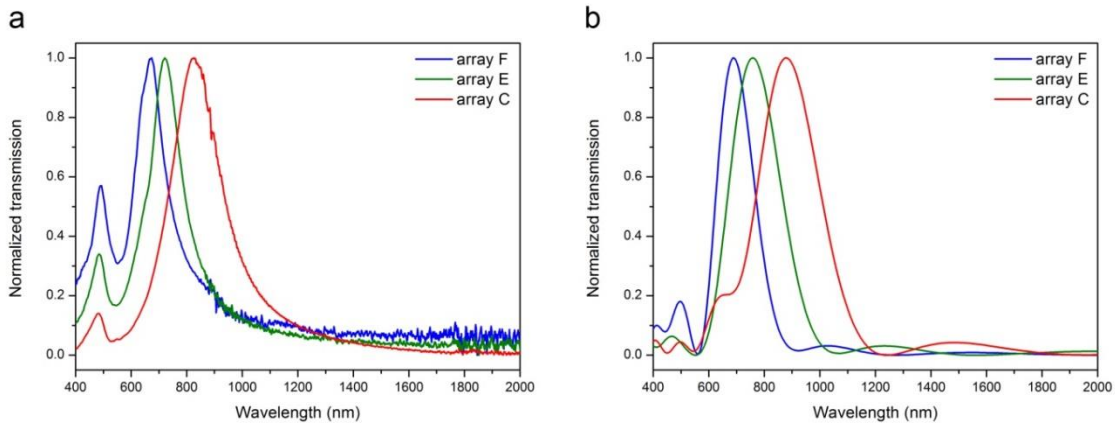

Figure 4.10, Normalized transmission spectra of split-ring shaped aperture arrays C, E and F in the y-polarisation state. (**a**) Measured spectra. (**b**) Simulated spectra. Both measured and simulated wavelengths were in the range 400 nm to 2000 nm.

Figure 4.11 (a) and **(b)** show the dispersion relationships of plasmonic resonance (peak wavelength) with respect to the split-angle of split-ring shaped aperture arrays C, E and F in the x-polarisation and y-polarisation states respectively. For the measurement results under the x-polarisation state, a 90^{o} increment in the split-angle from array C, to array E and finally to array F resulted in a 600 nm blue-shift in the resonant wavelength. For the y-polarisation state, the same increment in the split-angle resulted in a ~150 nm blue-shift. The simulation results also demonstrated the blue-shift in the resonance at two polarization states.

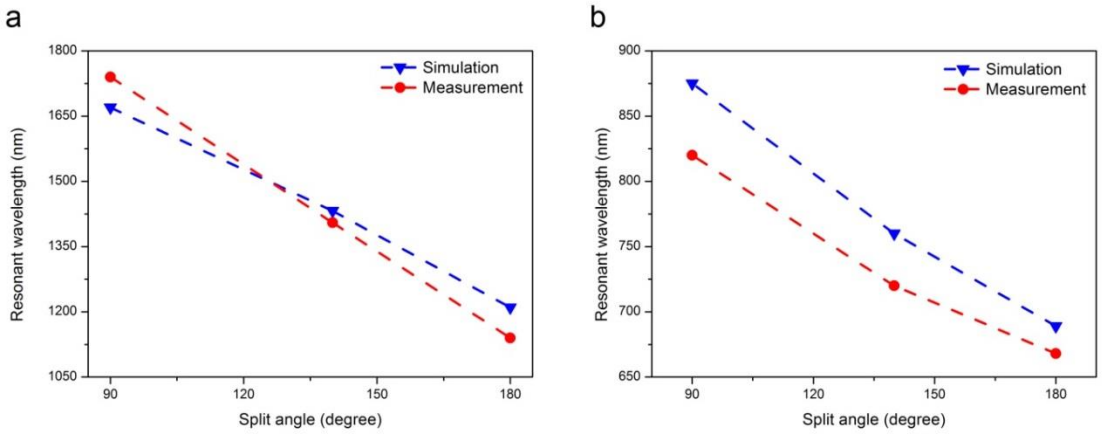

Figure 4.11, Dispersion relationships of plasmonic resonance with split-angle of the split-ring shaped aperture arrays C, E and F. (**a**) Dispersion relationships of the resonance with split-angle of the test arrays at the x-polarisation state. (**b**) Dispersion relationships of the resonance with split-angle of the test arrays at the y-polarisation state. The measured and simulated data are drawn with red and blue markers in each figure respectively.

4.4.2 Polarisation dependent SERS of 4-MBA on split-ring shaped aperture arrays

Through the analysis of the transmission spectra shown above, the split-ring shaped aperture array A was chosen as a test sample for SERS measurement under a 633 nm excitation laser. This is because under the y-polarisation state the optical resonance of array A was ~670 nm which was the closest to the excitation wavelength (633 nm) of all of the arrays. Although the resonant wavelength of array A did not match the 633 nm exactly, it still exhibited a very high transmission at that wavelength (as can be seen in **Figure 4.6 a**, where the normalized transmission intensity of split-ring shaped aperture arrays A at 633 nm was nearly 0.8). Moreover, the optical transmissions of all test arrays (including array A) under the x-polarisation state were in the near infrared range (1-2 μm) which was quite far away from the excitation wavelength. Therefore, for a 633 nm laser under the y-polarisation state as an excitation light, split-ring shaped aperture arrays A can be thought of as being excited to a resonant state which is termed as the “on resonance” state. On the contrary, when the 633 nm incident light was turned to x-polarisation state, such an array is in a non-resonant state which is termed as the “off resonance” state.

Figure 4.12 (a1)-(a3) shows the simulated electric field distributions on the top surface, in the middle of the aperture and at the bottom of the aperture respectively of array A, at 633 nm under the y-polarisation state. It can be seen that the electric field on top of the split-ring aperture (air/gold interface) became the strongest of the three, although there was some field enhancement at the bottom of the aperture. And the field was the weakest in the middle of the aperture. **Figure 4.12 (b1)-(b3)** show the simulated electric field distributions at the corresponding positions under the 633 nm x-polarisation state. Similarity to the y-polarisation state, the highest electric field appeared at the top surface (air/gold interface) and the lowest electric field was in the middle of the aperture. However, when comparing the top surface electric field enhancements between the two polarisation states, the largest field strength of the y-polarisation state was ~200 V/m which occurred at the aperture edges and the field strength in the centre of the aperture was still larger than 30 V/m. While the largest field strength of the x-polarisation state was ~90 V/m and the field strength in the centre of the aperture did not exceed 20 V/m. The scale range in each figure was chosen as 0-50 V/m in order to give a better visual effect of the electric fields rather than to show the actual highest and lowest values of those fields. In addition, for the y-polarisation state, the electric fields were excited at both inner and outer edges of the split-ring aperture (**Fig.4.12 (a1)**), while for the x-polarisation state, the electric field enhancements only appeared at the inner edge of the aperture. These simulation results also demonstrated that under the y-polarisation state of 633 nm excitation, the split-ring shaped aperture arrays A was in an "on resonance" state in which the resonant field became the strongest. But for the x-polarisation state, test array A cannot support a great field enhancement even though it was excited by using the same laser.

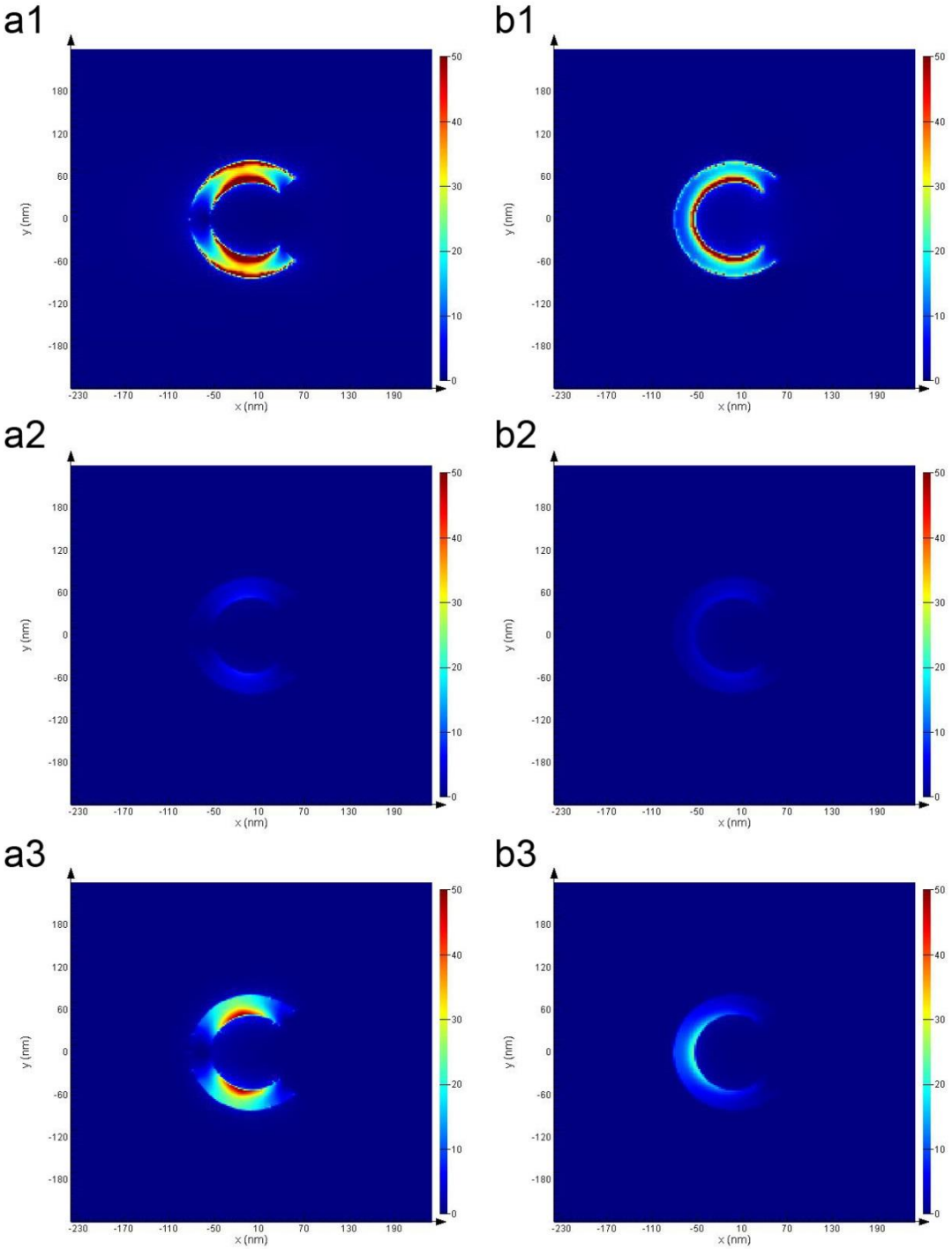

Figure 4.12, Plasmonic induced electric field enhancements at 633 nm of split-ring shaped aperture arrays A at different polarisation states. (**a1**) The electric field distribution on the top surface of the aperture in the y-polarisation state. (**a2**) The electric field distribution in the middle of the aperture at in the y-polarisation state. (**a3**) The electric field distribution at the bottom of the aperture in the y-polarisation state. (**b1**) The electric field distribution on the top surface of the aperture in the x-polarisation state. (**b2**) The electric field distribution in the middle of the aperture in the x-polarisation state. (**b3**) The electric field distribution at the bottom of the aperture in the x-polarisation state.

Figure 4.13 shows the surface enhanced Raman spectra of 4-MBA on the split-ring shaped aperture arrays A under the "on resonance" (y-polarisation) and "off resonance" (x-polarisation) states. Five repeated measurements were carried out at random positions on the test array under either "on" or "off" resonance states. At the "on resonance" state, due to the great resonant field enhancement a very strong surface enhanced Raman spectrum of 4-MBA (shown in red) can be seen. Two prominent peaks appeared at 1065 cm^{-1} and 1570 cm^{-1} which corresponded to the benzene ring breathing mode $\nu(CC)_{ring}$ [162, 163]. There were also some small peaks which appeared at 1132 cm^{-1}, 1173 cm^{-1}, 1232 cm^{-1} and 1426 cm^{-1} which can be attributed to the presence of -CH bonds and -COOH group. [154, 162] In contrast, when compared to the "off resonance" state, the intensities of two peaks at 1065 cm^{-1} and 1570 cm^{-1} became very weak (shown in blue) and they were difficult to distinguish. The peaks which appeared at the "on resonance" state in the region from 1100 cm^{-1} to 1450 cm^{-1} vanished. This is due to the relatively weak field generated by the test array at this "off resonance" state. Besides, at the "on resonance" state, the average intensity of the 1570 cm^{-1} peak based on such five repeated measured data was ~2710 counts with a standard deviation of ~550 counts. On the contrary, at the "off resonance" state, the average intensity of the corresponding peak was only about 342 counts. This analysis has shown that the split-ring shaped aperture arrays A exhibited the ability to enhance the Raman spectra only under the "on resonance" condition in which the polarisation of the excitation light must satisfy a certain requirement. Otherwise, even if the split-ring shaped aperture arrays A was excited by the same laser, it could not provide high fidelity sensing information.

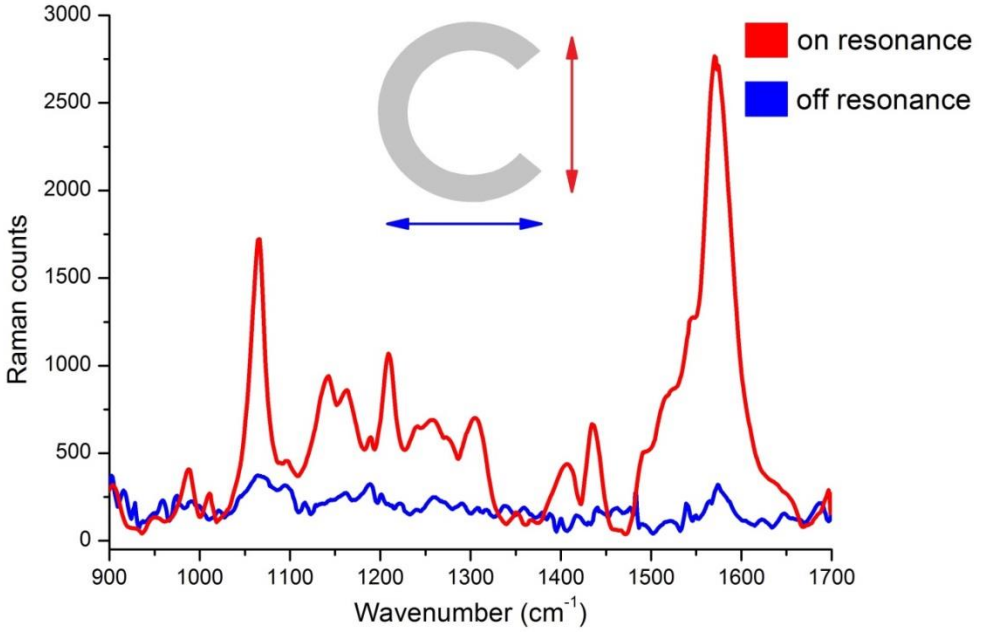

Figure 4.13, SERS spectra of 4-MBA attached to split-ring shaped aperture arrays A at 633 nm laser excitation under "on" and "off" resonance states. The Horiba LabRam HR800UV spectrometer was used for analysing the Raman signals and the acquisition time was 5 seconds for each measurement. The spectra in red and blue indicate the "on" and "off" resonance states respectively. The inserted diagram shows the orientation of the split-ring, and the red arrow indicates the incident light with y-polarisation (which corresponds to the "on resonance" state) and the blue arrow indicates the incident light with x-polarisation (which corresponds to the "off resonance" state). Before measurement, a piece of silicon was used to calibrate the spectrometer with the 520 cm^{-1} peak.

4.5 Conclusion

In this chapter, the gold split-ring shaped aperture array was proposed and the relevant fabrication and characterisation processes were introduced. Due to the asymmetric nature of the split-ring aperture, one structure was able to excite two different plasmonic resonances according to the incident polarisation. Two groups of experiments were carried out in order to study the effect of structural dimensions on the optical resonance. At both polarisation states (incident light polarised along either the x- or y- axis), the resonant wavelength of the split-ring shaped aperture arrays exhibited a red-shift when the aperture diameter was increased, and also exhibited a blue-shift when the split-angle was

increased. For the application in the molecular sensing, one resonance of a split-ring shaped aperture arrays was tuned to match the laser used in the Raman spectrometer, while the other resonance was tuned to the mismatched wavelength. At the resonance matching state, the split-ring shaped aperture was excited to support a large resonant field, thus Raman scattering could be enhanced. However, at the resonance mismatching state, the structure loses its ability in field enhancement even under the same laser excitation. These findings could be used in the area of polarisation dependent spectroscopy research and for potential applications in SERS as a molecular sensing platform as well.

Chapter 5 - Cross-shaped Aperture Arrays as Dual-Colour Pixels

Abstract

In this chapter, aluminium nanostructures consisting of cross-shaped apertures are demonstrated as dual-colour pixels for switchable microscopic chromatic information displays. These dual-colour pixels were fabricated by using electron-beam lithography and reactive ion etching techniques. Polarisation dependent optical transmission spectra were measured by a spectrometer. Due to the asymmetry of the cross-shaped aperture, one pixel is able to produce two distinct colours, selected when the polarisation of light incident on the rear of the pixels is changed. A colour palette comprising of 16 pixels with different cross arm lengths and array periods is presented. Various chromatic patterns are designed and fabricated by utilizing these dual-colour nano pixels for achieving polarisation controlled image switching. In order to have a further understanding of optical properties, the minimum array size for colour production and some initial attempts regarding colour mixing at nanoscale are presented.

5.1 Introduction

Colour pixels or colour filters are essential optical components in digital imaging applications. Commonly used colour filters can be categorized into two types: interference filters and organic dye filters. Interference filters rely on the optical interference produced by alternating thin-film dielectric coatings with different refractive indices deposited on a glass substrate. [169] Applications of these filters range from scientific instruments to commercial products, such as the fluorescence microscope, astronomical telescope, thermal imaging, digital projector, and so on. However, such interference colour filters, normally working as a separate component in an optical system, are difficult to achieve miniaturisation and integration with other functional modules.

Organic dye filters are widely utilised in the integrated imaging sensors, liquid crystal displays (LCD), and organic light emitting diodes (OLED). [170-176] These dyes tend to degrade at high temperatures or through exposure to ultraviolet

radiation. Moreover, due to the poor optical absorption of the dyes, these filters cannot produce high quality colours when the thickness of organic dye is smaller than hundreds of nanometres. [174]

In contrast to the traditional colour filters, metallic nanoparticles which possess the capability to absorb and scatter certain wavelengths of incident light are proposed as a new candidate for colour filters. [177] However, the easily oxidized nature of tiny metals employed in nanoparticle structures results in fast degradation of the filters, thus limiting wide applications. In the past two decades, with the rapid development of nanofabrication techniques, it has been possible to realize metal nano hole arrays with associated extraordinary optical transmission (EOT) and this opens up a promising solution for future colour filtering. As mentioned before, the surface plasmon resonance (SPR) excited at metal/dielectric interface contributes to light transmission through subwavelength holes. Therefore, by varying the size, shape, thickness and period of the array, the permitted SPR coupling frequency can be tuned, dictating the colour of the transmitted light. [41, 178, 179]

Nevertheless, the vast majority of filters, whether they be interference- based, dye-based, are designed to operate efficiently at a single wavelength, though in some cases, such as polarimetry microscopy, security encryption and hyperspectral imaging, dual- or multi-colour filters are necessary. [180-182] Therefore, a dual-colour generation scheme using Al asymmetric cross-shaped aperture arrays was proposed, designed and fabricated in order to achieve one single nanostructure which is able to produce two separate colours depending on incident polarisation. [183] This providing more versatility than single wavelength filters. Aluminium was the chosen material due to its low cost, its compatibility with current industrial fabrication processes, and, significantly, its high plasmon frequency which allows visible wavelength transmission with a lower optical loss than gold and silver alternatives. [184-186] When free space propagating light encounters a slit-shaped nano aperture, a series of selection rules, defined by the size, shape and array period, determine what wavelengths will be transmitted. Paramount among these is the requirement for the polarisation orientation (transverse electric-field component) of the incident

light to be perpendicular to the long-axis of the slit; a condition without which no light will be permitted through the aperture, regardless of wavelength. [187]

In this chapter, the optical dual-colour palette which comprises of the pixels with different combinations of arm-length and array period together with measured and simulated transmission spectra are presented, and this is followed by the results of optical transmission images of several microscopic patterns at different incident polarisations. At the end, two discussions about minimal pixel size for making colours and possibility of colour mixing at nanoscale, and the plots of some typical pixels in the CIE chromaticity coordinates are shown.

5.2 Materials

The materials used in this Chapter refer to Section 2.2 in Chapter two.

5.3 Methods

5.3.1 Fabrication of dual-colour nano pixels

Figure 5.1 shows the fabrication process for Al dual-colour nano pixels by using electron-beam lithography, reactive ion etching (RIE), and inductively coupled plasma (ICP) deposition. Pyrex glass substrate was firstly modified with a 100 nm aluminium thin film. (For the procedures of cleaning and metallization refer to **Sections 2.3.3.1**and **2.3.3.2** respectively) The sample was then spin coated with a dilute ZEP520A positive e-beam resist (2 parts ZEP with 1 part anisole) at 3000 rpm spinning speed, after oven baking, the resist thickness was approximately 250 nm, (**Fig.5.1.1**). Cross-shaped patterns were generated on the resist layer after e-beam exposure and development, (**Fig.5.1.2**). Exposure dose was 700 $\mu C/cm^2$ and VRU was set to 6. (For the procedures of resist coating, e-beam lithography and resist development refer to **Sections 2.3.3.4**, **2.3.3.5** and **2.3.3.6** respectively.) Then the developed resist acted as an etching mask and the sample was plasma etched by using $SiCl_4$ gas. After etching, the mask (resist) was removed by rinsing the sample in 50℃ Microposit remover 1165 for 30 minutes (**Fig.5.1.3**). Finally, a 150 nm SiO_2 cap layer was deposited on the surface of etched Al structure (**Fig.5.1.4**). (For the procedures of Al plasma dry etching and SiO2 deposition refer to **Sections 2.3.3.8** and **2.3.3.3** respectively)

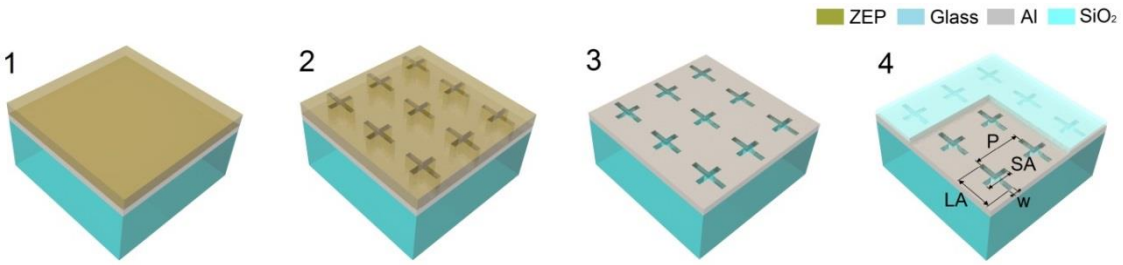

Figure 5.1, Fabrication of Al cross-shaped dual-colour nano pixels. (**1**) Sample preparation and resist coating. (**2**) Cross-shaped patterns were generated on the resist layer. (**3**) Cross-shaped patterns were transferred to Al layer. (**4**) Complete aluminium dual-colour pixels after SiO_2 deposition, in which LA and SA refer to the long-arm and short-arm of the cross respectively. P and w refer to array period and arm width.

Figure 5.2 shows the SEM image of one test sample. As may be seen, the electron scattering inside the resist during e-beam exposure may cause structural expansion and distortion to occur on the cross shape (especially at the junction area of the long-arm and short-arm).

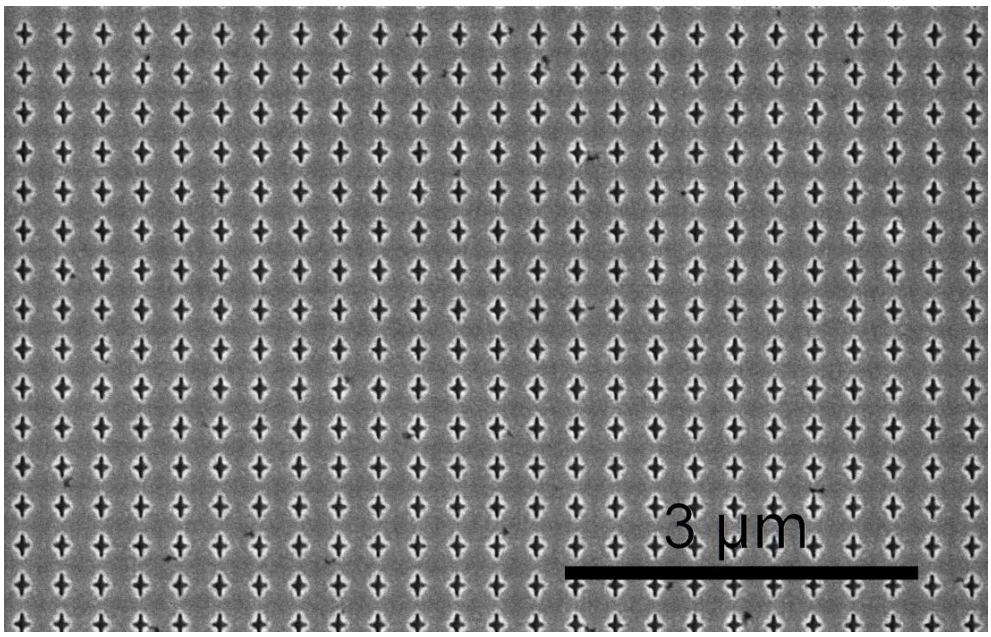

Figure 5.2, SEM image of the test sample. The dimensions are: LA 203 nm, SA 120 nm, P 310 nm and w ~30 nm (the width of each arm is identical).

5.3.2 Optical transmission measurement

For measuring the transmission spectra of the nano pixels, the wavelength range was set from 400 nm to 800 nm. Detailed measurement procedure can be found in **Section 2.3.3.12**.

5.3.3 FDTD simulation

A 100 nm Al layer was defined from z=0 nm to z=100 nm. A cross-shaped structure was inserted into that metallic layer to represent the cross-shaped aperture. A 150 nm SiO2 layer was defined from 100 nm to 250 nm. A plane wave source was positioned at z=-400 nm and the wave propagated along the +z axis. Three field monitors in the x-y plane was positioned at z=0 nm, 50 nm and 100 nm for visualising the electric field distributions at these slices of the Al layer. For the LA transmission, the incident polarisation was set to perpendicular to the long-arm, and for the SA transmission, incident polarisation was set to perpendicular to the short-arm. **Figure 5.3** shows the schematic of the simulation model and the details of the simulation methods can be found in **Section 2.3.1**.

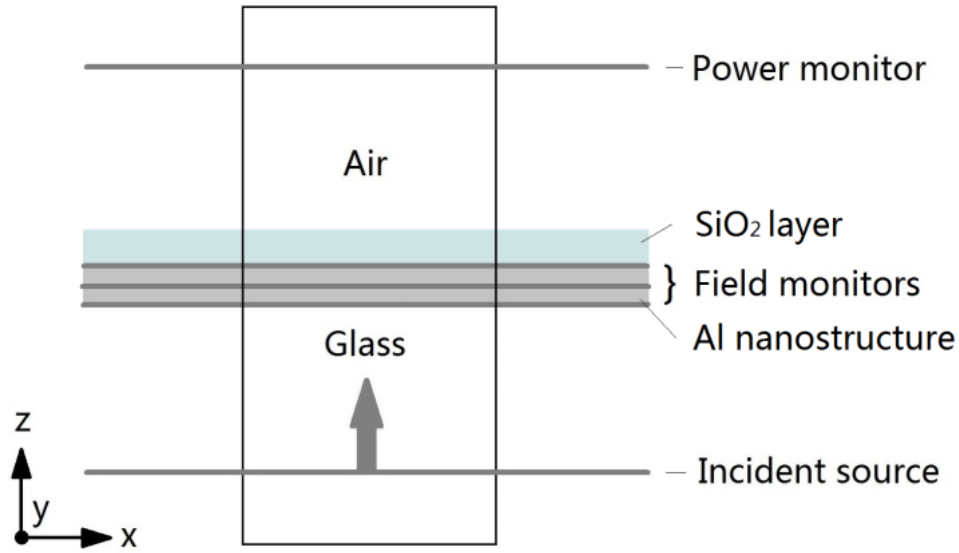

Figure 5.3, Schematic of the simulation model for Al dual-colour pixel. The arrow indicates the propagation direction of the incident wave and the area enclosed in the rectangle represents the simulation space. Three field monitors were positioned at the glass/Al interface, the centre of the Al layer and at the Al/SiO_2 interface respectively.

5.3.4 Dual-colour pattern design

The method used for designing complicated shapes which are made up of such dual-colour nano pixels is as follows: first of all, a pattern image in the JPEG format was imported into the L-Edit software (version 15). Simultaneously, one parameter needs to be pre-defined to control the imported pattern's size; this is

that which is for converting image pixel numbers into pattern dimensions (length and width). The second step is to create a nano pixel array (as a normal square array consisting of cross-shaped apertures) and make sure the array is large enough to cover the pattern, and then, after Boolean operation (logic "and") operated in L-Edit, those pixels inside the pattern are left, while the others (pixels located outside the pattern) are deleted, thus generating a new pixel array in which the border is in accordance with the shape of the pattern. And finally, to export the file of the pattern filled with the pixels to a GDS format. Then the previously described procedures for e-beam lithography (**Section 2.3.3.5**) were followed. Four different types of patterns were designed in this experiment: university logos; smiling-sad cartoon faces; butterflies and Marylyn head portraits.

5.3.5 Image capturing by an optical microscope

Details of the colour imaging process can be found in **Section 2.3.3.16**. A Zeiss 50x, 0.5NA objective was used for taking the pictures of the dual-colour palette and microscopic chromatic patterns, and a Zeiss 100x, 0.75NA objective was used for the investigation of pixels arrays with minimal size for colour generation. A Zeiss 10x, 0.25NA objective was used for taking the pictures of arrays of mixed pixels. The long-arm transmissions were produced by making the polarisation of the incident light perpendicular to the long axis of the aperture. The short-arm transmissions were produced only by rotating the polariser 90^{o} but keeping the sample orientation the same. This procedure was followed throughout the experiment.

5.4 Results and discussions

5.4.1 Optical characterisations of dual-colour nano pixels

The plasmonic resonances of a cross-shaped pixel array depend on many parameters such as arm lengths (long-arm length and short-arm length), arm width and array period. In order to ensure that both the optical resonances of each pixel array are visible at the two incident polarisations, structural dimensions should not exceed certain limits, therefore, some geometrical sizes were set as constants. In this chapter, the long-arm length was fixed at 200 nm

and the width of each arm was fixed at 30 nm, while the short-arm length was increased from 120 nm to 180 nm by 20 nm steps, and the array period was increased from 250 nm to 340 nm by 30 nm steps. Therefore 16 pixel arrays with different combinations in short-arm length and array period can be fabricated on the same substrate, thus creating a colour palette.

Figure 5.4 shows bright-field transmission images of that colour palette when the polarisation of the white-light incident on the rear of the palate was polarised along the long-arms and short-arms of the apertures. In this colour palette, pixels' long-arms orientated along the y-axis and their short-arms orientated along the y-axis. A linear polariser was used to control the polarisation of the incident light. As can be seen, all of these pixel arrays were fabricated in 20×20 μm^2 and numbered 1-16. In all cases, the LA length was 200 nm, while the SA lengths were 120 nm, 140 nm, 160 nm and 180 nm respectively in each column moving from top to bottom, and the array period was 250 nm, 280 nm, 310 nm and 340 nm respectively in each line moving from left to right.

Figure 5.4 (a) shows the long-arm transmissions of all these nano pixels. In this case, the incident light was polarised along the x-axis (x-polarisation), where the incident polarisation (electric oscillations) was perpendicular to the long-arms, thus enabling the light transmission through them. No significant differences are observed in the transmission colours of the four pixels in each column, because the long-arm lengths and array period of such pixels are the same. However, four different colours can be seen from the pixels located in different columns, because the array periods of such pixels are different although the long-arm length is still unchanged. **Figure 5.4 (b)** shows all these nano pixels' short-arm transmissions. In this case, the incident light was polarised along the y-axis (y-polarisation), where the incident polarisation was perpendicular to the short-arms, thus enabling the light transmission through them. Since either the short-arm length or the pixel period are different for each of these 16 arrays, a gradual red-shift in transmitted colours can be seen; from high frequency blue wavelengths at the shortest arm length and smallest period (pixel 1), to low frequency reds at the longest arm length and largest periods (pixel 16). Significantly, there is a distinct difference between the colours transmitted by the long and short-arms of the same pixel array, showing that a single geometry

nano-pixel can be tuned to produce any two colours in the visible spectrum. Also because of the polarisation dependant transmission requirements, the resonance of one arm does not affect that of the other, giving a large tunability between the two polarisations.

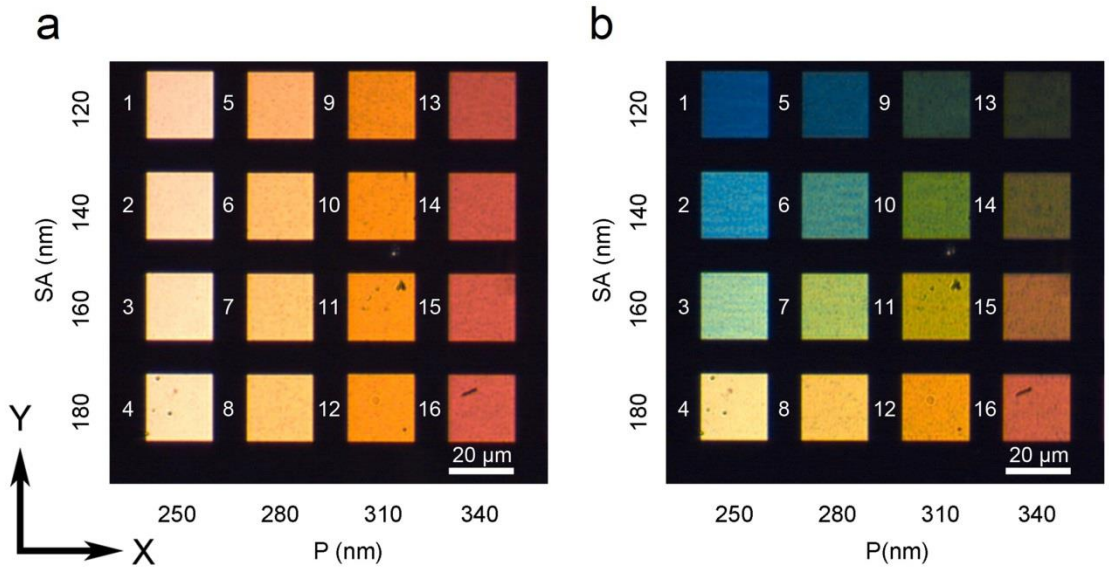

Figure 5.4, Bright-field microscopic images of the nano-pixels back illuminated with a white light source from the rear of the sample. (a) Long-arm transmission image, the incident light was polarised along the x-axis (the electric oscillations of the incident light was perpendicular to the long-arms, thus light was transmitted through the long-arms). (b) Short-arm transmission image, the incident light was polarised along the y-axis (the electric oscillations of the incident light was perpendicular to the short-arms, thus light was transmitted through the short-arms). The directions of x and y are indicated in the figure.

Figure 5.5 shows the transmission spectra associated with each of the 16 fabricated arrays, measured at both x- and y- polarisation states. For ease of reading, these spectra have been grouped according to their array period.

The spectra transmitted through the long-arms of each pixel were plotted in **Figure 5.5 (a1)**-**(a4)**. Due to the identical long-arm size of all these pixels, the plasmonic response of each pixel was only determined by array period. Therefore, the long-arm transmission varies only a small amount between pixels with the same period, although the short-arm lengths of those arrays are different. The spectral variations are mostly due to pattern defects introduced during fabrication. As can be seen in **Figure 5.5 (a1)**, for example, the average

transmission maxima of pixels 1-4 (which had the same period of 250 nm) appeared at 656 nm, hence the indistinguishable colours pixels 1-4 of the first column of **Figure 5.4 (a)** were produced. Similarly, the colours produced by the pixels where the array period was constant in other columns are also hard to differentiate. However, for an identical cross shape, with the array period increasing from 280 nm, to 310 nm, and to 340 nm, the average peak wavelength was 649 nm, 652 nm, and 662 nm respectively. Thus four colours were generated, which are cream, yellow, orange and red in the columns progressing from left to right, as shown in **Figure 5.4 (a)**. Apart from the array period, another factor which contributes to the transmitted colour is the full-wave half-maximum (FWHM) or the sharpness of the spectra which was shown to decrease in line with the increment in array period. The average FWHM drops from 373 nm for a period of 250 nm, to 120 nm for a period of 340 nm when comparing pixels 1-4 with pixels 13-16. Increasing the period narrows the spectral FWHM, resulting in more "pure" colours which appear closer to the wavelength of the peak value. Predictably, the larger period also manifests itself as a drop in transmitted light intensity, for example, for pixels 3 and 15 having the same cross-shaped configuration, the optical transmission dropped from >12% in pixel 3 (array period 250 nm) to <5% in pixel 15 (array period 340 nm).

The wavelengths transmitted through the short-arm of each nano pixel were plotted in **Figure 5.5 (b1)**-**(b4)**. Within each column of 4 pixels the array period and the long-arm length were the same, but the length of the short-arm was 120 nm, 140 nm, 160 nm and 180 nm progressing from top to bottom, as shown in **Figure 5.4**. Through the comparison of SA transmissions among pixels with identical geometries, for example, pixel 3, 7, 11 and 15 which use the same cross-shape configuration (LA 200 nm and SA 160 nm) but increasing in array period (250 nm, 280 nm, 310 nm and 340 nm respectively), the corresponding transmission peak appeared at 536 nm, 553 nm, 576 nm and 598 nm. Therefore, the colours of these 4 pixels produced by the short-arms changed from light green to brownish red, as can be seen in **Figure 5.4 (b)**.

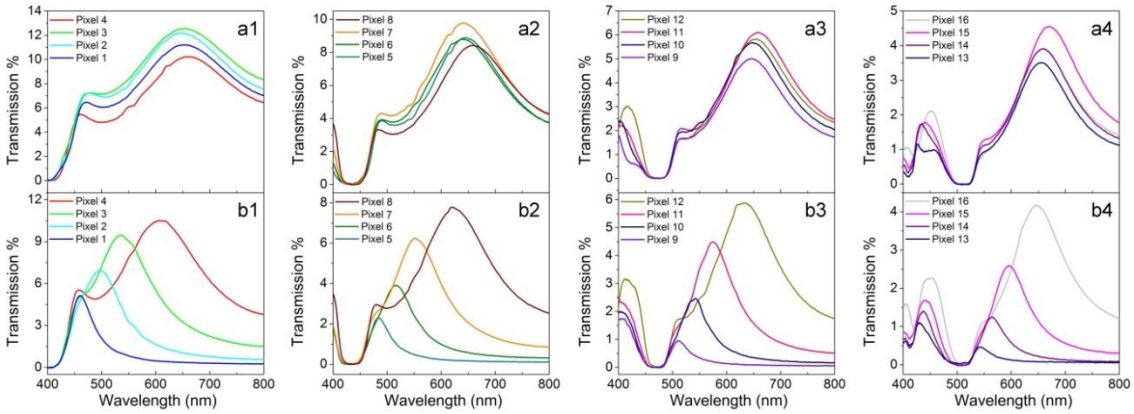

Figure 5.5, Measured optical transmission spectra of each pixel. (**a1**) and (**b1**) Transmission spectra of pixels 1-4 through the apertures' long-arms and short-arms respectively. (**a2**) and (**b2**) Transmission spectra of pixels 5-8 through the apertures' long-arms and short-arms respectively. (**a3**) and (**b3**) Transmission spectra of pixels 9-12 through the apertures' long-arms and short-arms respectively. (**a4**) and (**b4**) Transmission spectra of pixels 13-16 through the apertures' long-arms and short-arms respectively.

Figure 5.6 (a) and **(b)** show the simulated long-arm and short-arm transmission spectra of pixels 1-16 respectively. For the long-arm transmissions, due to the perfect geometrical shapes and dimensions in each model, the simulated peak wavelength of spectra of each pixel set 1-4, 5-8, 9-12 and 13-16 appeared at 640 nm, 654 nm, 656 nm and 670 nm as shown in **Figure 5.6 (a1)**, **(a2)**, **(a3)** and **(a4)** respectively, which confirm that only long-arm length determines the LA transmission with a fixed array period, and the resonance is independent of the short-arm length. In addition, for structures with identical dimensions, for example, pixel 1, 5, 9 and 13, transmission intensity decreases from 28% of pixel 1 to <14% of pixel 13. For the short-arm transmissions, when only increasing short-arm length (with fixed array period), each pixel set 1-4, 5-8, 9-12 and 13-16 showed significant transmission red-shifting of: 150 nm, 130 nm, 124 nm and 97 nm (as shown in **Figure 5.6 (b1)**, **(b2)**, **(b3)** and **(b4)** respectively). Moreover, when only increasing array period but keeping structural dimensions identical, a red-shifting tendency in transmission curves can be observed as well. Taking pixels 3 and 15 as examples, a 90 nm increment in array period results in a 40 nm red-shift in resonant peak and the corresponding transmission intensity drops from 18% in pixel 3 to <8% in pixel 15. Besides, with increasing short-arm length,

transmission intensity has increased ~5 times (from 5% of pixel 1 to 25% of pixel 4).

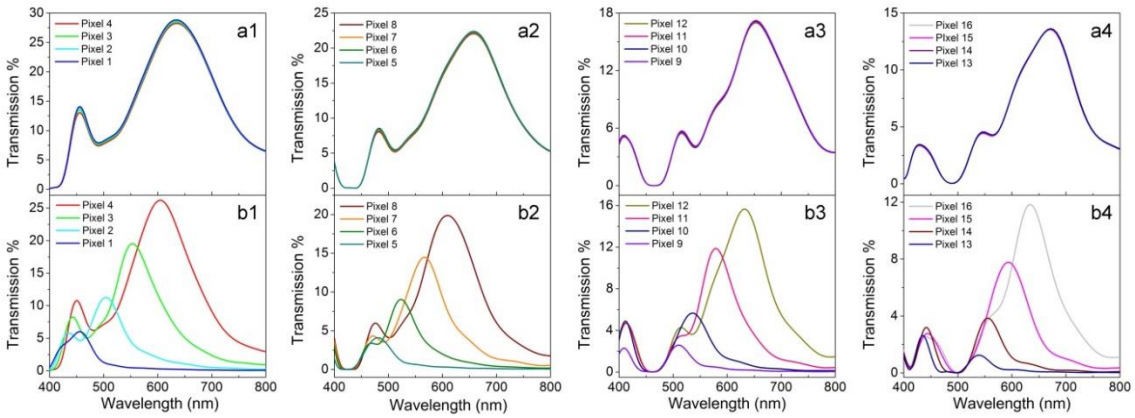

Figure 5.6, Simulated optical transmission spectra of each pixel. (**a1**) and (**b1**) Transmission spectra of pixels 1-4 through the apertures' long-arms and short-arms respectively. (**a2**) and (**b2**) Transmission spectra of pixels 5-8 through the apertures' long-arms and short-arms respectively. (**a3**) and (**b3**) Transmission spectra of pixels 9-12 through the apertures' long-arms and short-arms respectively. (**a4**) and (**b4**) Transmission spectra of pixels 13-16 through the apertures' long-arms and short-arms respectively.

Figure 5.7 contains a representative example of these simulations for geometry identical to pixel 6 showing the measured and simulated transmission spectra, as well as the electric field distributions at the glass/Al interface, the centre and the Al/SiO_2 interface of the cross-shaped aperture, at peak resonance wavelength of each polarisation state. The simulated transmission spectra in **Figure 5.7 (a)i** and **(b)i** show a good agreement with the experimental results at both polarisation states. For the condition that incident polarisation was perpendicular to the long-arm, nearly all the resonant fields are distributed along the long-arm, as shown in **Figure 5.7 (a)ii**-**(a)iv**. This means the incident light is able to propagate through it. Similarly, for the condition that incident polarisation was perpendicular to the short-arm, the resonant fields are confined along the short-arm, along with the optical transmission through the short-arm, as shown in **Figure 5.7 (b)ii**-**(b)iv**. However, very strong fields distributed at glass/Al and Al/SiO_2 interfaces and a few fields are inside the aperture as can be seen in both polarisation states. These also demonstrated that the excited surface plasmon resonances were confined at the two interfaces.

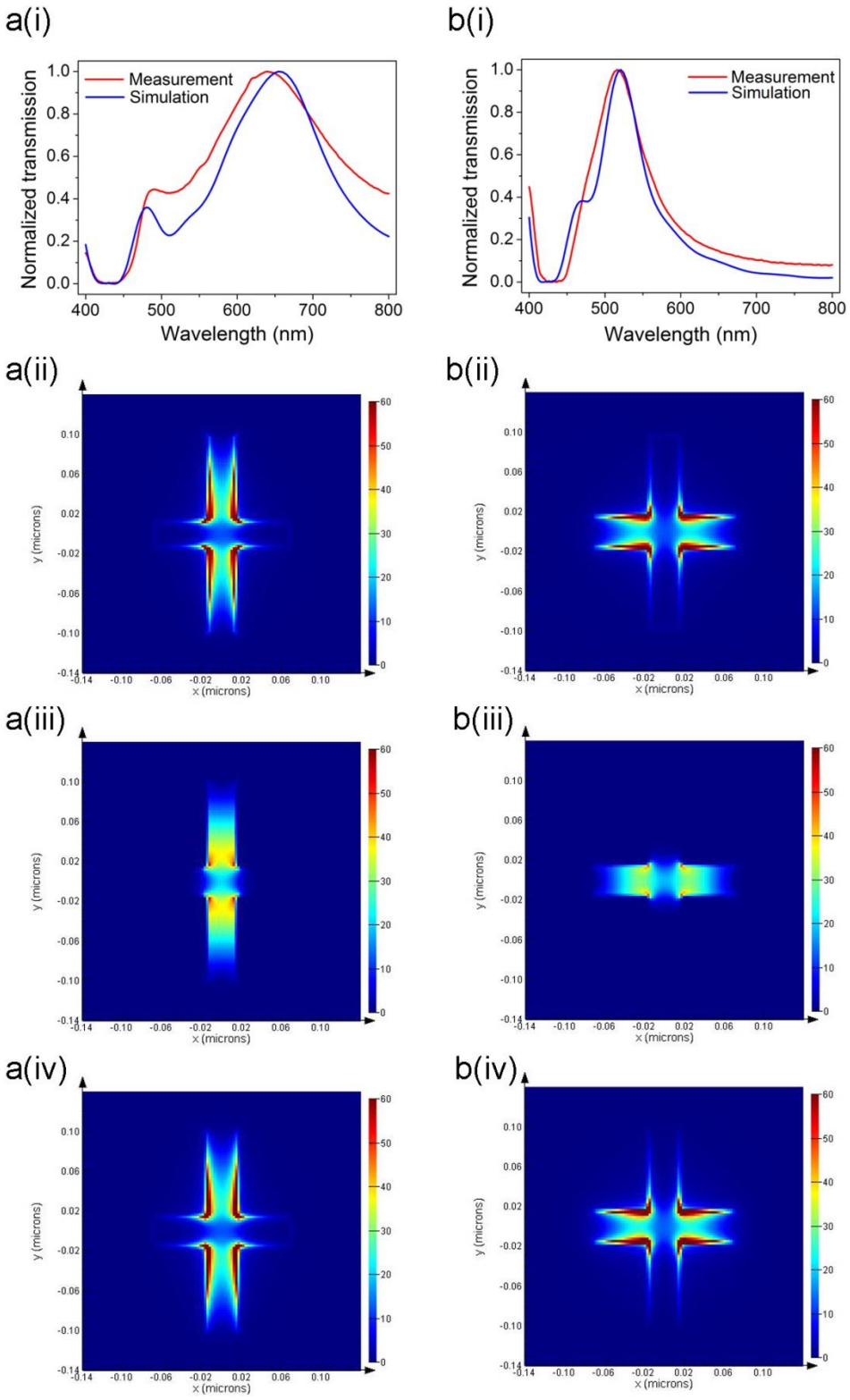

Figure 5.7, Numerical simulations of the plasmonic responses of Pixel 6. (**a(i)**) Simulated and measured transmission spectra under the x-polarisation. (**b(i)**) Simulated and measured transmission spectra under the y-polarisation. (**a(ii)**-**(iv)**) Resonant electric-field distributions at the glass/Al interface, the centre and the Al/SiO_2 interface under the x-polarisation. (**b(ii)**-**(iv)**) Resonant electric-field distributions at the glass/Al interface, the centre and the Al/SiO_2 interface under the y-polarisation.

5.4.2 Dispersion relationships of dual-colour nano pixels

From the discussion in previous chapters, it has already known that the structural resonance is dependent on apertures' dimensions. The changes in array period alter the interference condition. The changes in aperture size result in the variation of the wavelength of the surface plasmon resonance, and the waveguide mode inside the aperture. Therefore, the resonance tunable feature can be studied through an analysis of the dispersive property. In this section, the nano-pixel's dispersion relationship relating the peak wavelength and FWHM to structural dimensions will be discussed according to the measured spectra,. These include: the dispersion relationships between transmission peaks and short-arm lengths at the y-polarisation state; the dispersion relationships between transmission peaks and array periods at both x- and y- polarisation states; and the dispersion relationships between FWHMs and array periods at both x- and y- polarisation states.

Figure 5.8 shows the dispersion relationships of short-arm transmission peaks and short-arm lengths at 4 different array periods (250 nm, 280 nm, 310 nm and 340 nm) corresponding to pixels set 1-4, 5-8, 9-12 and 13-16. As can be seen, for pixel set 1-4 with fixed array period 250 nm (shown in the orange line), when the short-arm length increased from 120 nm to 180 nm, the transmission maxima red-shifted from 460 nm of pixel 1, to 497 nm of pixel 2, to 536 nm of pixel 3, and to 608 nm of pixel 4. Similar red-shifting tendency due to the 60 nm increment in short-arm length can be observed in other pixels sets. For pixel 5-8 (period fixed as 280 nm, shown in the blue line), the red-shift was 140 nm from the from 485 nm of pixel 5 to 625 nm of pixel 8; for pixel 9-12 (period fixed as 310 nm, shown in the dark-red line), the red-shift was 123 nm from the from 511 nm of pixel 9 to 634 nm of pixel 12; for pixel 13-16 (period fixed as 340 nm, shown in the magenta line), the red-shift was 104 nm from 544 nm of pixel 13 to 648 nm of pixel 16.

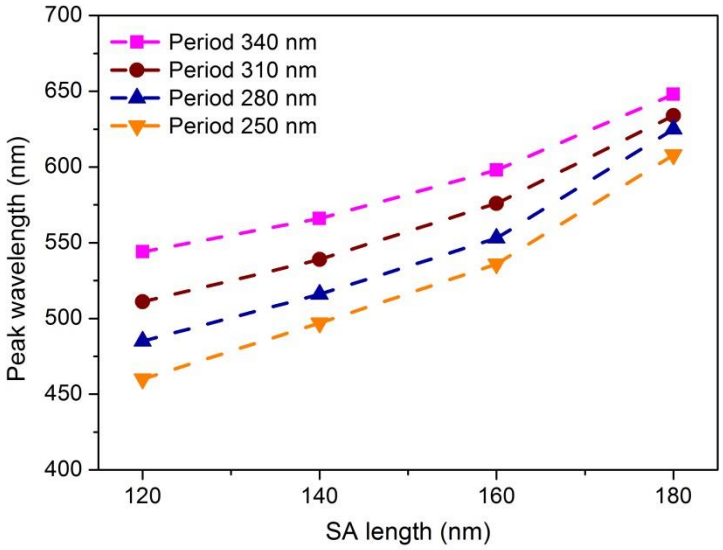

Figure 5.8, Dispersion relationships of transmission maxima and short-arm lengths under the y-polarisation state. The orange markers indicate the data points of pixel set 1-4. The blue markers indicate the data points of pixel set 5-8.The brown markers indicate the data points of pixel set 9-12. The magenta markers indicate the data points of pixel set 13-16.

Figure 5.9 (a) and **(b)** show the dispersion relationships of transmission peaks and array periods at x- and y- polarisation states respectively. At x-polarisation (**Fig.5.9 (a)**), for the pixels with short-arm length 120 nm, 140 nm, and 160 nm, when array period is increased from 280 nm to 340 nm, the red-shift was 7 nm, 19 nm and 30 nm respectively. However, larger more obvious red-shifts in peak wavelength were observed at y-polarisation (**Fig.5.9 (b)**). For the pixels with SA 120 nm (pixel 1, 5, 9 and 13), a 90 nm increment in period lead to 84 nm red-shifting in transmission, in which the peak position of each pixel was at 460 nm, 485 nm, 511 nm and 544 nm respectively. For the pixels with SA 140 nm (pixel 2, 6, 10 and 14), the same increment in period lead to 69 nm red-shifting in transmission (in which the peak position of each pixel was at 497 nm, 516 nm, 539 nm and 566 nm respectively). Similarly, the red-shift for the pixels with SA 160 nm (pixel 3, 7, 11 and 15) and SA 180 nm (pixel 4, 8, 12 and 16) was 62 nm and 40 nm respectively.

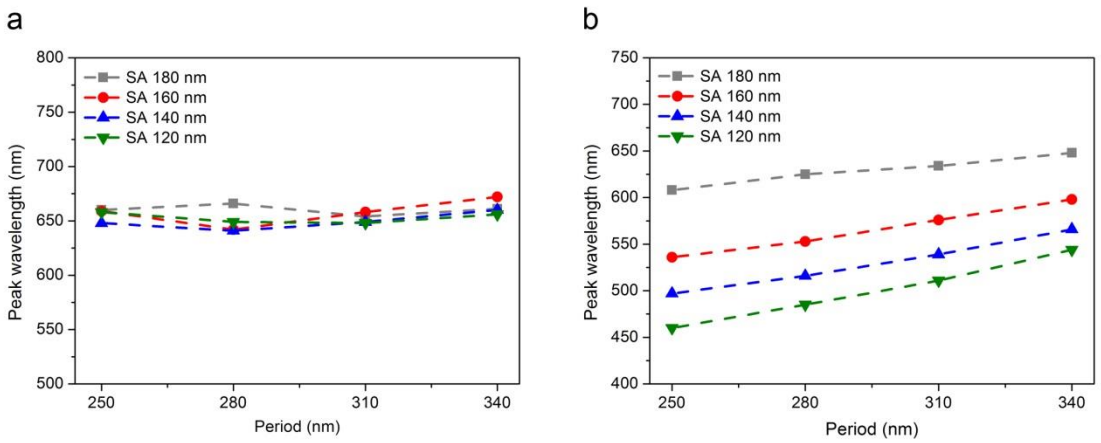

Figure 5.9, Dispersion relationships of transmission peaks and array periods under different polarisation states. (a) x-polarisation state. (b) y-polarisation state. The green markers indicate the data points of pixels with SA 120 nm. The blue markers indicate the data points of pixels with SA 140 nm. The red markers indicate the data points of pixels with SA 160 nm. The grey markers indicate the data points of pixels with SA 180 nm.

Figure 5.10 (a) and **(b)** show the dispersion relationships of spectra FWHMs and array period at x- and y- polarisation states respectively. Generally, the spectra become narrower as the array period increases. Specifically, at x- polarisation (**Fig.5.10 (a)**), when the array period increased from 250 nm to 340 nm, the average FWHM of the pixels decreases from 373 nm, to 238 nm, to 176 nm and to 120 nm corresponding to the 4 different array periods (250 nm, 280nm, 310 nm and 340 nm respectively). At y-polarisation (**Fig.5.10 (b)**), when the array period increases by 90 nm, for the pixels with a SA length of 120 nm, FWHM undergoes a slight drop from 53 nm, to 47 nm, and further to 41 nm and down to 40 nm corresponding to pixels 1, 5, 9 and 13. The decrease in FWHM was just 13 nm. However, a 31 nm decrease occurred for the pixels with SA length 140 nm (dropping from 98 nm, to 85 nm, and further to 66 nm and down to 57 nm corresponding to pixels 2, 6, 10 and 14). The decrease in FWHM was 54 nm for the pixels with SA length 160 nm (FWHM drops from 135 nm, to 118 nm, and further to 93 nm and down to 81 nm corresponding to pixels 3, 7, 11 and 15). For the pixels with SA length 180 nm, FWHM dropped from 145 nm, to 131 nm, and further to 111 nm and down to 97 nm corresponding to pixels 4, 8, 12 and 16, which had a 48 nm decrease.

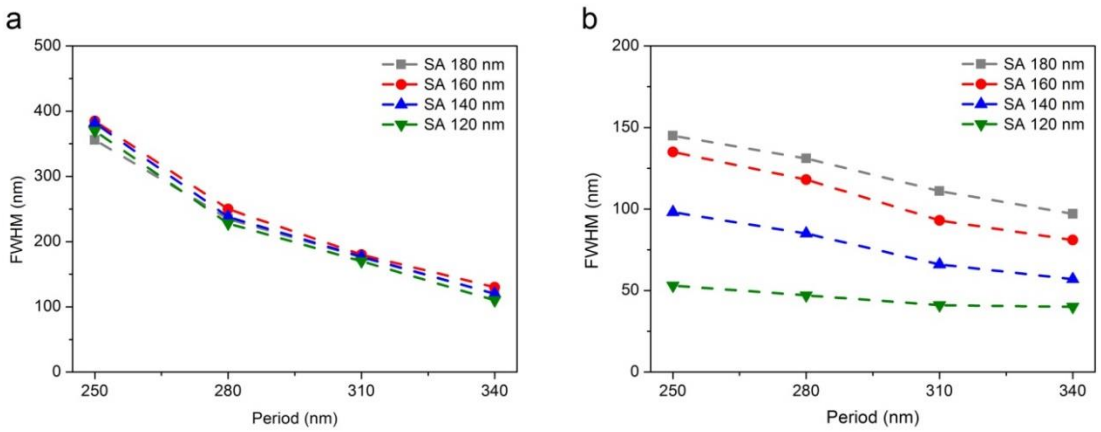

Figure 5.10, Dispersion relationships of spectra FWHM and array periods under different polarisation states. (**a**) x-polarisation state. (**b**) y-polarisation state. The green markers indicate the data points of pixels with SA 120 nm. The blue markers indicate the data points of pixels with SA 140 nm. The red markers indicate the data points of pixels with SA 160 nm. The grey markers indicate the data points of pixels with SA 180 nm.

Through the discussions above, optical resonances and spectra FWHMs of the nano pixels can be manipulated by varying structural dimensions such as arm-lengths and array period. For the long-arm transmission, with increasing array period, the transmissions tend to red-shift. For the short-arm transmission, with increases in either the SA length or array period, the transmissions tend to red-shift. The spectra became narrower when the array period was increased for both the long-arm and short-arm transmissions. Once again, due to the independent effects of long-arm and short-arm lengths on polarisation dependent optical transmission, these nano pixels can produce two colours whereas single wavelength filters can only produce one colour. Besides this, these dispersion relationships give guidance in structural design for generating specific colours.

5.4.3 Micro-imaging of polarisation depended chromatic patterns

In order to demonstrate the practical applications of micro-printed dual-colour displays that can be achieved by using these proposed dual-colour nano pixels, several microscopic patterns comprising of single nano pixel or pixel combinations were produced. These include five Glasgow University logos, one cartoon pattern, two butterflies and two Marilyn Monroe head portraits. These

have been designed and fabricated for the testing of image switching and shifting.

Figure 5.11 shows one set of the optical images of the university logo and the corresponding SEM images. The pairs of photos (b1) and (b2) are of the pattern but captured in different polarisations, this also applies to (c1) and (c2), and (d1) and (d2). Each pattern size was the same with the width at 95 μm and the height at 48 μm. The dimensions of the cross-shaped apertures in each pattern were the same but the apertures were patterned in two orthogonal orientations in different areas. The long-arms were orientated along the x-axis for the background and along the y-axis for the lettering. Logo (b), (c) and (d) each consist of pixel 1, 9 and 13 respectively. The optical transmissions of these three logos at the LA polarisation state are shown in **Figure 5.11 (b1)**, **(c1)** and **(d1)**, and at the SA polarisation state are shown in **Figure 5.11 (b2)**, **(c2)** and **(d2)**. **Figure 5.11 (a1)** shows the SEM images of the overall profile of logo (b) and **Figure 5.11 (a2)** shows the enlarged view of top right part of the letter U, showing the details of the pixel orientation arrangement. The boundary of the lettering and of the background can be clearly identified by the orientations of long-arm in each area. Both pixels had the same LA length 200 nm and SA length 120 nm, but the corresponding array period of pixel 1, 9 and 13 was 250 nm, 310 nm and 340 nm respectively. The result of this arrangement, as can be easily seen, is that when the polarisation of incident light was changed from along the x-axis (x-polarisation) to along the y-axis (y-polarisation), the colour of the background and the lettering flipped. In detail, as shown in **Figure 5.11 (b1)**-**(d1)**, when these logos were illuminated by x-polarised white light, the colour of lettering and background for logo (b) was light-yellow and blue, for logo (c) was orange and green, and for logo (d) was red and dark-green, after tuning the incident light to SA polarisation state, each logo exhibited a colour reversal between background and lettering (shown in **Figure 5.11 (b2)**-**(d2)**) when it was illuminated by y-polarised light.

Figure 5.11, The SEM and optical images of the microscopic logo patterns of the University of Glasgow 'printed' in nano scale resolution to achieve colour flipping. (a1) The SEM image of logo (b). (a2) Enlarged SEM image showing the top right part of letter U. (b1) Optical transmission image of logo (b) with the incident white light polarised along the x-axis. (b2) Optical transmission image of logo (b) with the incident light polarised along the y-axis. (c1) Optical transmission image of logo (c) with the incident white light polarised along the x-axis. (c2) Optical transmission image of logo (c) with the incident white light polarised along the y-axis. (d1) Optical transmission image of logo (d) with the incident white light polarised along the x-axis. (d2) Optical transmission image of logo (d) with the incident white light polarised along the y-axis. The directions of x and y are indicated in the figure.

Except for creating images that can change their colours, these nano pixels can also be used to create images which display different information at different polarisation states. This is shown by optical images of two university logo patterns under x- and y- polarised white light illumination in **Figure 5.12**, where the size is 95 μm in width and 48 μm in height. Each of these logo patterns consisted of two different pixels, but all the pixels were arranged in the same orientation with the long-arms paralleled to y-axis. Pixel 5 and 7 (these two pixel configurations had the same array period of 280 nm) were used to build the lettering and background areas of logo (a), and pixel 9 and 10 (these two pixel configurations had the same array period of 310 nm) were used for making lettering and background areas of logo (b). These pixels were chosen because the colour they produced when the plasmon propagated through their long-arms was identical, thus making the useful information to disappear in surrounding area; whereas the colours produced when light propagated through their short-arms were different, enabling information to be conveyed through the contrast in the colours. **Figure 5.12 (a1)** and **(b1)** shows the logo images illuminated by x-polarised white light, and as can be seen, image (a) and (b) each displayed a monochromatic colour (light-yellow and orange respectively) where nothing can be recognized, while for the y-polarised incident light, as shown in **Figure 5.12 (a2)** and **(b2)**, each image showed two colours where the lettering appeared distinct from the background. In image (a2), the lettering and background area are dark-blue and greyish-green respectively, and in image (b2) the lettering and background area are two greens.

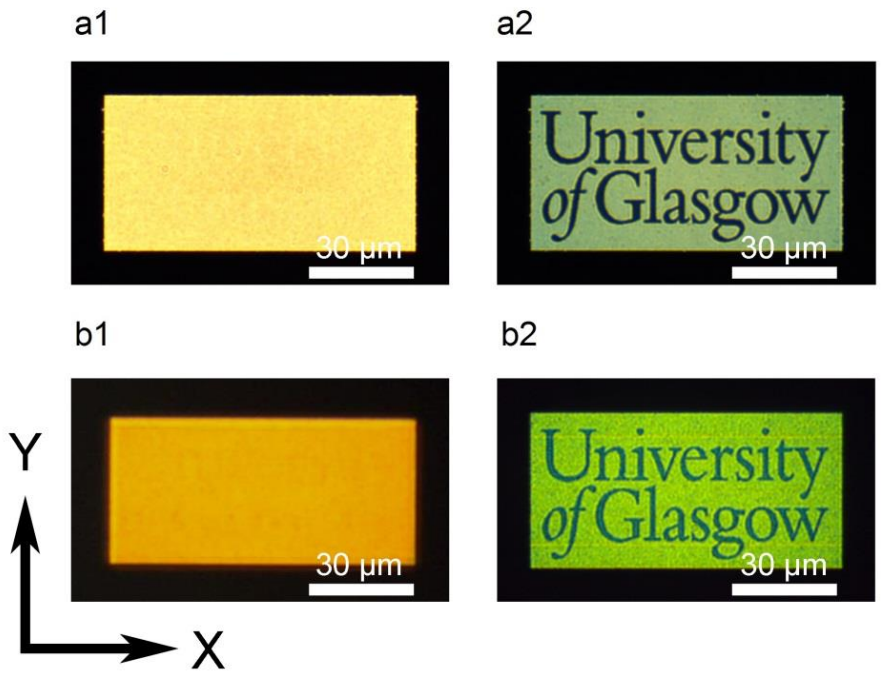

Figure 5.12, Two microscopic logo patterns of the University of Glasgow 'printed' in nano scale resolution to display different information at different polarisation states. (a1) Optical transmission image of logo (a) with the incident white light polarised along the x-axis. (a2) Optical transmission image of logo (a) with the incident white light polarised along the y-axis. (b1) Optical transmission image of logo (b) with the incident white light polarised along the x-axis. (b2) Optical transmission image of logo (b) with the incident white light polarised along the y-axis. The directions of x and y are indicated in the figure.

As well as selectively displaying, these dual-colour nano pixels can also be employed to achieve image shifting at different polarisations. A microscopic smiling-sad facial expression cartoon pattern was designed and fabricated to test for image shifting. **Figure 5.13** shows the designed cartoon pattern (**Fig.5.13 (a1)**) and the corresponding optical transmission images (**Fig.5.13 (a2)** and **(a3)**) illuminated by different polarised incident light. As shown in **Figure 5.13 (a1)**, the smiling eyes and mouth are labelled as area 1, the sad eyes and mouth are labelled as area 2 and the background is labelled as area 3. The areas of the eyes and the mouth consist of pixel 1 and pixel 3 respectively. For the smiling eyes and mouth regions (area 1), the pixels' long-arms were orientated along the y-axis while for the sad eyes and mouth regions (area 2), the pixels' long-arms were orientated along the x-axis. A symmetrical cross-shaped apertures (LA=SA=200 nm, period 250 nm) were applied for making the background area. Such pixel arrangements resulted in a repeated 2-frame image shifting with

flipping the polariser, and the corresponding optical images of x- and y-polarisation states which are shown in **Figure 5.13 (a2)** and **(a3)**. For the x-polarisation state, light transmitted through the long-arms of pixels in area 1 (smiling eyes and mouth) and the background area, resulting in the colour from region 1 and 3 being an identical light-yellow colour. This is due to the same LA length and array period therein. However, for the pixels in sad eyes and mouth areas, the light transmitted through their short-arms, thus producing blue and green colours in their respective areas, and these colours can be easily distinguished from the light-yellow colour of the background. Therefore, only a sad facial expression appeared. Since the pixels in eyes and mouth of area 1 and 2 are only different in their orientations (orthogonal with each other), when the incident polarisation changes 90^{o}, the colours from the smiling eyes and mouth (area 1) and the sad eyes and mouth (area 2) flips, thus a smiling facial expression was produced.

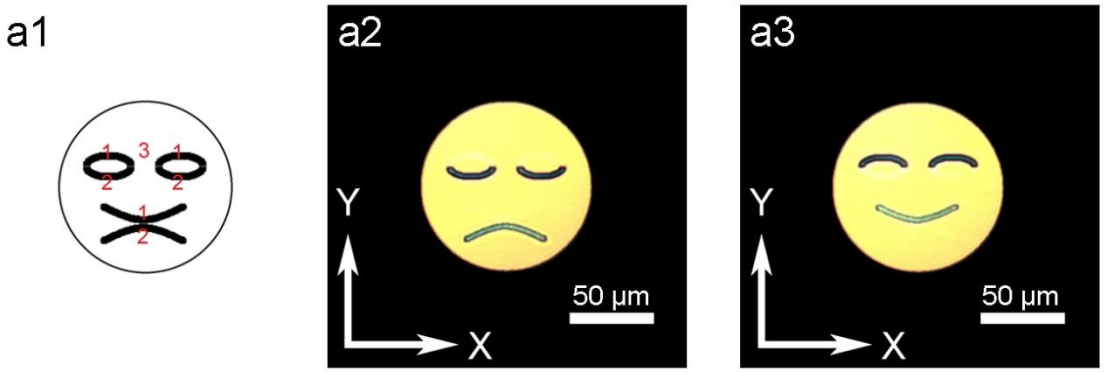

Figure 5.13, Design and microscopic optical images of smiling-sad cartoon pattern 'printed' in nano scale resolution. (**a1**) Design of cartoon pattern, red label 1 indicated the smiling eyes/mouth, red label 2 indicated the sad eyes/mouth and red label 3 indicated the face. (**a2**) Optical transmission image with the incident white light polarised along the x-axis. (**a2**) Optical transmission image with the incident white light polarised along the y-axis. The diameter of the fabricated facial pattern was 100 µm, and the width of eyes and mouth were both 4 µm. The directions of x and y are indicated in the figure.

The demonstrations above have successfully shown that these dual-colour nano pixels can be used in achieving colour flipping or image switching, for patterns with pre-designed or simple geometrical shapes such as university logos and smiling-sad cartoons. However, some more complicated shapes, for example,

butterfly patterns and the Marilyn Monroe head portraits were designed and fabricated for showing that these nano pixels can also be used widely.

Figure 5.14 shows the layout designs and optical transmission images of two butterfly patterns. For the butterfly (a), pattern design is shown in **Figure 5.14 (a1)**, and as can be seen, the left and right wings were divided into 4 symmetrical parts labelled 1-4. The pixels arrangements in these four areas were as follows: pixel 9 with its long-arm along the y-axis (area 1); pixel 14 with its long-arm along the x-axis (area 2); pixel 10 with its long-arm along the x-axis (area 3); and pixel 7 with its long-arm along the y-axis (area 4), and the body was labelled as 5 in which symmetrical cross-shaped apertures (LA=SA=200 nm, period 340 nm) were used. The consequence of this design was that when the pattern was back illuminated by x-polarised white light, the four parts of the wings appeared as orange, olive green, green and cream respectively going from the top to the bottom, as shown in **Figure 5.14 (a2)**. After rotating the polariser 90^{o} to the y-polarisation state, the colours in the corresponding parts of the wings turned to bluish-green, red, orange and yellowish-green, as shown in **Figure 5.14 (a3)**. Due to the fact that the cross-shapes used in the body part were symmetrical, the colour stayed the same regardless of incident polarisation. The size of the fabricated butterfly (a) was 130 μm in wingspan and 82 μm in height.

For the butterfly (b), pattern design is shown in **Figure 5.14 (b1)**. For this pattern, some curved and spotted decorations (which were labelled as 1 and 2) were inserted into the two wings, and the rest of the wings and the butterfly body were labelled as 3 and 4 respectively. The pixel arrangements in these areas were as follows: pixel 9 with its long-arm along the x-axis was used in area 1; pixel 10 with its long-arm along the x-axis was used in area 2; pixel 3 with its long-arm along the y-axis was used in area 3, and a symmetrical cross configuration (LA=SA=200 nm, period 340 nm) was used in area 4. Due to the same long-arm orientation (parallel with y-axis) of pixels in area 1 and 2, when the incident white light was x-polarised, light transmitted through the long-arms of the pixels in area 1 and 2, thus producing an identical orange colour for the decorations. While the transmission of light in area 3 was from the pixels' short-arms, therefore, the rest of wings appeared as a blue colour. When the incident

light was changed to y-polarisation, the light transmitted through the short-arms of the pixels in decoration parts of the wings (area 1 and 2), and through the long-arms of the pixels in the rest of the wings (area 3), therefore, two greens appeared in areas 1 and 2 due to the different SA length of the pixels therein, and a light-yellow colour was generated in area 3. The body only produced an identical red colour due to the symmetrical geometrical configurations of the pixels used in area 4. The corresponding optical transmission images of butterfly (b) at x-and y- polarisation states are shown in **Figure 5.14 (b2)** and **Figure 5.14 (b3)**. The size of the fabricated butterfly (a) was 110 μm in wingspan and 67 μm in height.

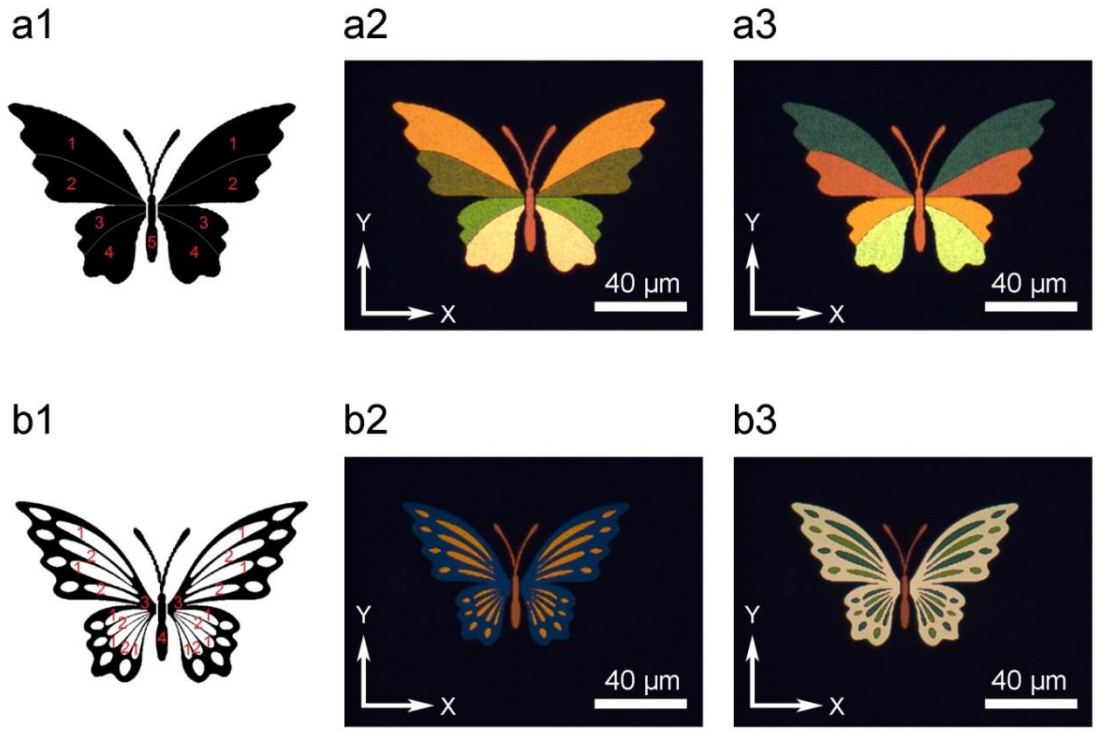

Figure 5.14, Designs and microscopic optical images of butterfly patterns 'printed' in nano scale resolution. (**a1**) Design pattern of butterfly (a), pixels 9, 14, 10 and 7 were used in the areas red labelled 1-4 respectively; a symmetrical cross producing the red colour was used in area 5. (**a2**) Optical transmission image of the butterfly (a) with the incident white light polarised along the x-axis. (**a3**) Optical transmission image of butterfly (a) with the incident white light polarised along the y-axis. (**b1**) Design pattern of butterfly (b), pixels 9, 10 and 1 were used in the areas red labelled 1-3 respectively; a symmetrical cross producing the red colour was used in area 5. (**b2**) Optical transmission image of butterfly (b) with the incident white light polarised along the x-axis. (**b3**) Optical transmission image of butterfly (b) with the incident white light polarised along the y-axis. The directions of x and y are indicated in the figure.

Figure 5.15 shows two sets of microscopic optical transmission images of the Marilyn Monroe head portrait at x- and y- polarised incident white light. These portrait patterns were fabricated to be 87 μm in width and 90 μm in height. For Marilyn portrait (a), the background and the eyebrow parts consisted of pixel 6 with the long-arm orientated along the y-axis; the hair part consisted of pixel 10 with the long-arm orientated along the x-axis; the face and the mouth parts consisted of pixel 13 with the long-arm orientated along the y-axis and x-axis respectively. As a consequence, when incident white light was x-polarised, the light was transmitted through the long-arms of the pixels in the background and eyebrows (pixel 6), the short-arms of the pixels in hair (pixel 10), the long-arms of pixels in the face (pixel 13), and the short-arms of pixels in the mouth (pixel 13), therefore, the colours in such corresponding areas were light-yellow, green, red and dark-green respectively, as can be seen in **Figure 5.15 (a1)**. However, when the incident light was changed to the y-polarisation state, as shown in **Figure 5.15 (a2)** the colour in each area changed to light-blue, orange, dark-green and red (corresponding to the background and eyebrow, the hair, the face, and the mouth respectively). For the design of the Marilyn portrait (b), pixel 9 with long-arm orientated along the y-axis was used for the background; pixel 13 with the long-arm orientated along the x-axis was used for the hair; pixel 10 with the long-arm orientated along the x-axis was used for the face; and pixel 3 with the long-arm orientated along the y-axis was used for the mouth. The result of these pixel arrangements is that when the incident white light was changed from the x-polarised state to the y-polarised state, the background and eyebrows changed from an orange colour to bluish-green, the hair changed from dark-green to red; the face changed from green to red; and the mouth changed from light-yellow to light-cyan.

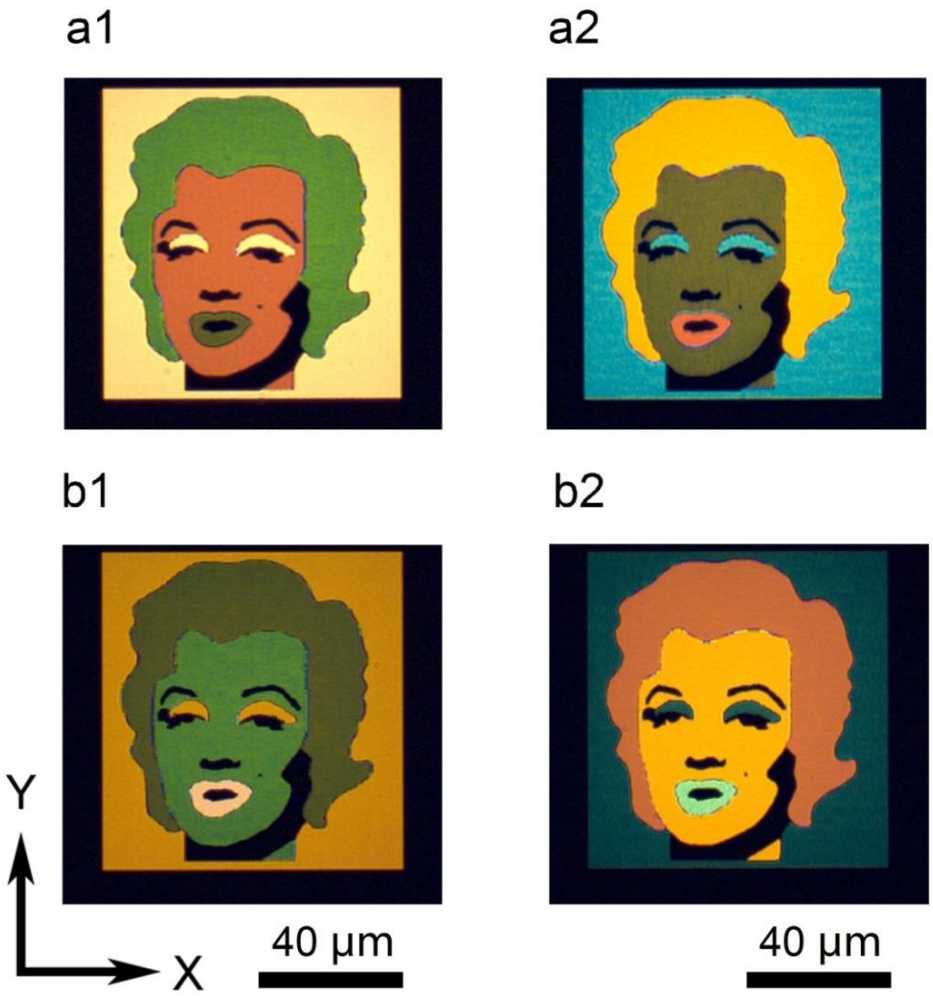

Figure 5.15, Microscopic optical images of the Marilyn Monroe head portrait 'printed' in nano scale resolution. (**a1**) Optical transmission image of portrait pattern (a) with incident white light polarised along the x-axis. (**a2**) Optical transmission image of portrait pattern (a) with incident white light polarised along the y-axis. (**b1**) Optical transmission image of portrait pattern (b) with incident white light polarised along the x-axis. (**b2**) Optical transmission image of portrait pattern (b) with incident white light polarised along the y-axis. The directions of x and y are indicated in the figure.

5.4.4 Minimum pixel size to produce colour

The previous section (**5.4.3**) has demonstrated that these dual-colour nano pixels can be used for making various microscopic chromatic patterns, even with complicated geometrical shapes. In order to achieve the higher and higher demands for high resolution displaying or imaging, such as in the applications of high-definition TVs, digital cameras and so on, the dimensions of the pixels should be made as small as possible yet while retaining the capability for effective colour filtering. However, the minimum size of the chromatic patterns shown before was about 2-3 µm (the spots on the wings of the butterfly (b)),

therefore, it is necessary to explore what is the minimal or critical dimensions of one pixel that are still able to produce colours effectively.

To investigate the smallest pixels for colour generation, 20 pixel arrays consisting of the same cross-shaped aperture (pixel 10 with LA 200 nm, SA 140 nm, P 310 nm was chosen) but increasing in array size were fabricated. These were captured by a microscope under the x- and y- polarisation states. The orientations of the long-arms were arranged along the y-axis and the orientations of the short-arms were arranged along the x-axis.

Figure 5.16 (a) and **(b)** shows the optical transmission images of these pixel arrays at long-arm transmission and short-arm transmission, which were captured by x-polarised and y-polarised light respectively. The 1x1 pixel array (1 cross aperture) is located in the leftmost position of these pixels arrays as indicated by the white arrow, the green arrow indicates the 2x2 pixel array (4 cross apertures), the blue arrow indicates the 3x3 pixel array (9 cross apertures), and the red arrow indicates the 4x4 pixel array (16 cross apertures), sequentially, the pixel finally increased to the 20x20 array (400 cross apertures) which is located in the rightmost of these pixel arrays as indicated by the grey arrow. Because there is only one cross structure contained in the 1x1 pixel, the minimal size is 0.2 μm in the y-axis (LA length) and 0.14 μm in the x-axis (SA length). This pixel appeared as a very faint and tiny point which can be seen in the long-arm transmission, but the colour was difficult to discern. However, this pixel became invisible and was unable to generate any colour at short-arm transmission. With increasing array size, the 2x2 pixel array (0.45 μm in length/height) and 3x3 pixel array (0.76 μm in length/height) can produce two discernible colours at both long-arm and short-arm transmissions, but the pixel tended to be a round shape rather than the actual square shape. While, for the 4x4 pixel array (1 μm in length/height) both the colour and geometrical shape can be fully presented at the two polarisation states. Therefore, the smallest size of dual-colour nano pixels where the colour and shape can be identified in an ordinary microscope is the 1 μm (4x4 pixel array).

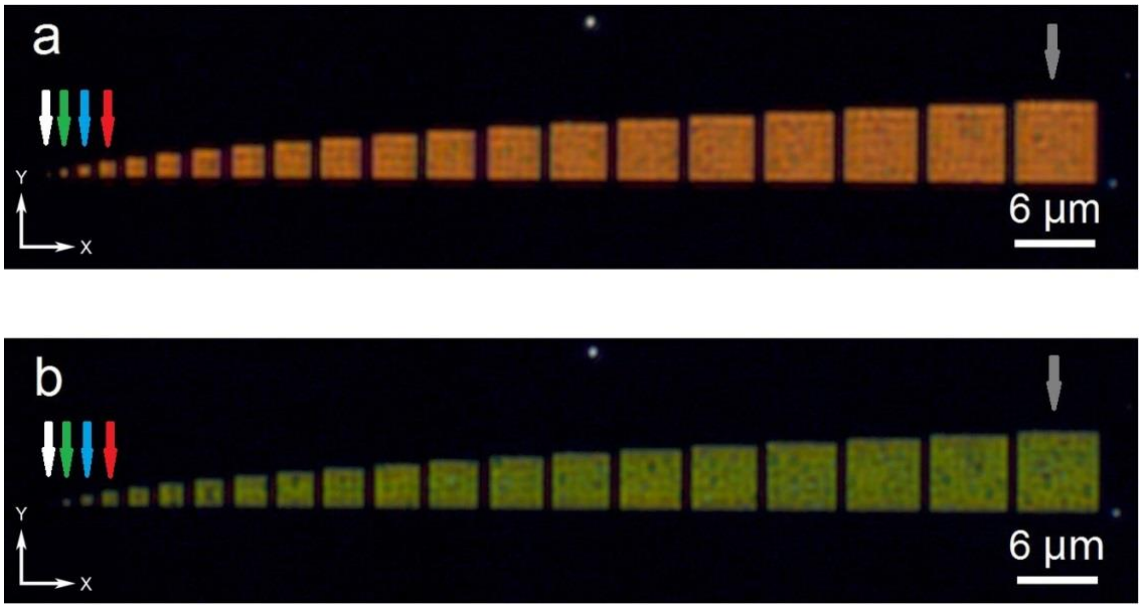

Figure 5.16, Microscopic optical images of a series of pixel arrays. The size of these pixels increased from a 1x1 pixel array to a 20x20 pixel array. (**a**) The long-arm transmission image where the incident white light was polarised along the x-axis. (**b**) The short-arm transmission image where the incident white light was polarised along the y-axis. The 1x1 pixel, 2x2 pixel, 3x3 pixel, 4x4 pixel, and 20x20 pixel arrays were indicated by the white arrow, green arrow, blue array, red arrow, and grey arrow respectively.

5.4.5 Colour mixing at nanoscale

So far, the manipulation of the pixels' colours was achieved by varying their geometrical sizes such as arm-lengths and array periods. To further investigate the optical properties of these dual-colour nano pixels, it is possible to tune the transmissions by creating arrays comprising of multiple pixel geometries in different ratios to achieve colour mixing. Pixel 5 (LA 200 nm, SA 120 nm, period 280 nm) and pixel 8 (LA 200 nm, SA 180 nm, period 280 nm) were chosen as two basic pixels for making mixed pixel arrays with different mixing ratios. The reasons for choosing these two pixels were: (1) there was a large colour contrast between pixel 5 (blue) and pixel 8 (yellow), therefore, the new colour might be expected to be different from the original two colours, (2) the array period of these two pixels was the same, therefore, the mixed pixels arrays also kept the same period as the original pixels, only with different combinations of the cross apertures. Apart from pixel 5 (array A) and pixel 8 (array G), another five mixed pixel arrays were fabricated. These were: pixel B with 3:1 Blue-Yellow mixing ratio, pixel C with 2:1 Blue-Yellow mixing ratio, pixel D with 1:1 Blue-Yellow

mixing ratio, pixel E with 1:2 Blue-Yellow mixing ratio, and pixel F with 1:3 Blue-Yellow mixing ratio. **Figure 5.17** shows the short-arm transmissions of these corresponding five mixed pixel arrays (B-F) together with the two basic pixel arrays (A and G). As can be seen, with increasing the proportion of the yellow producing arrangement, the transmitted colour as perceived shifted from blue (pixel 5) to yellow (pixel 8) through a gradient of distinct colours.

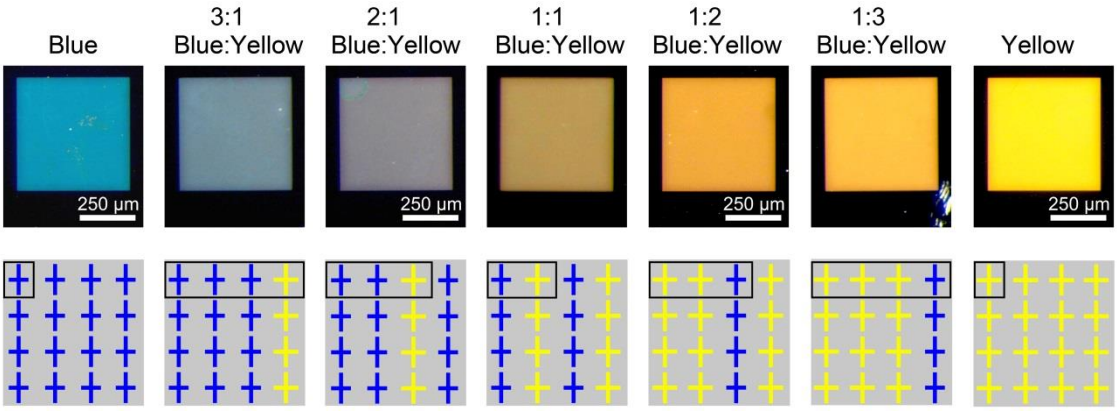

Figure 5.17, Microscopic optical images of mixed pixel arrays. (**A**) pixel 5, pure Blue with no mixing, (**B**) mixed pixel array B, 3:1, Blue: Yellow mixing ratio, (**C**) mixed pixel array C, 2:1, Blue: Yellow mixing ratio, (**D**) mixed pixel array D, 1:1, Blue: Yellow mixing ratio, (**E**) mixed pixel array E, 1:2, Blue: Yellow mixing ratio, (**F**) mixed pixel array F, 1:3, Blue: Yellow, (**G**) pixel 8, pure Yellow with no mixing. The diagrams under each optical image show the colour mixing scheme and the crosses in the black rectangular indicate the repeating unit. The blue cross and the yellow cross represent apertures in the pixel 5 (pure blue) and the pixel 8 (pure yellow) respectively.

Figure 5.18 shows the measured short-arm transmission spectra of pixels A-G. For pixel A (pure blue colour), there is only one peak which can be observed at about 488 nm with 5.8% transmission, and for pixel G (pure yellow colour), there is also only one peak, at about 612 nm with 13% transmission. However, with more yellow pixels involved in making the mixed pixel arrays progressing from pixel B to F, the corresponding blue transmission peak decreases and yellow transmission peak increases. As shown in the spectra of pixel arrays B and C, although the transmission intensities decreased to about 3.5%, the overall transmissions were still dominated by the blue colour. When the blue-yellow mixing ratio became 1:1 as in pixel D, a third peak at 559 nm with 5.7% transmission appeared in the spectrum. This peak was located between the blue (peak at 488 nm) and yellow (peak at 612 nm) colours which correspond to the

transmissions of two basic pixels (pixel A and G). When the proportion of yellow colour continued to increase and overwhelmed that of the blue colour, very broad yellow transmissions tended to dominate the pixel colour. And pixels E and F had peaks at 612 nm with the intensity about 6.6% and 7% respectively and the 559 nm peak disappeared from those spectra.

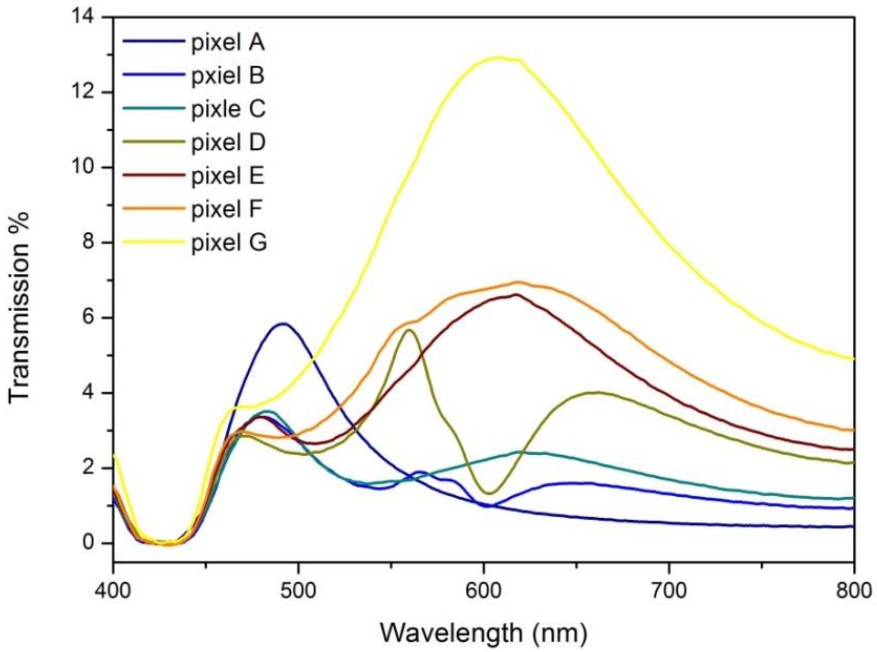

Figure 5.18, Experimentally measured short-arm transmission spectra of pixels A-G. The measured range was from 400 nm to 800 nm.

5.4.6 CIE1931 chromaticity diagram for the pixels

In order to obtain the human physiological perception of these dual-colour pixels rather than the physical characterization in the electromagnetic spectrum, the plots of CIE1931 chromaticity diagram for some of these dual-colour pixels are presented. **Figure 5.19 (a)** gives the chromaticity coordinates of three typical pixels in the colour palette. This included pixel 1 at short-arm transmission, pixel 6 at short-arm transmission and pixel 15 at long-arm transmission. As can be seen, the short-arm transmitted colours of pixel 1 and 6 located in the blue and green region respectively. However, for the long-arm transmission of pixel 15, the colour was not in the standard red region, this was due to another small transmission peak appeared at the short wavelength range (shown in **Fig.5.5 (b4)**). The colour triangle in this figure shows chromaticity tunable range of these dual-colour pixels. **Figure 5.19 (b)** gives the chromaticity coordinates of

the colour mixing pixels A-G. As shown in the figure, the coordinate of pixel A was close to the blue region and the coordinate of pixel G was in the yellow region. With increasing the ratio of yellow, the coordinate of mixed pixel (B-F) moves toward the yellow region, this gradual colour change can also be verified by the measured spectra which were shown in **Fig. 5.18**.

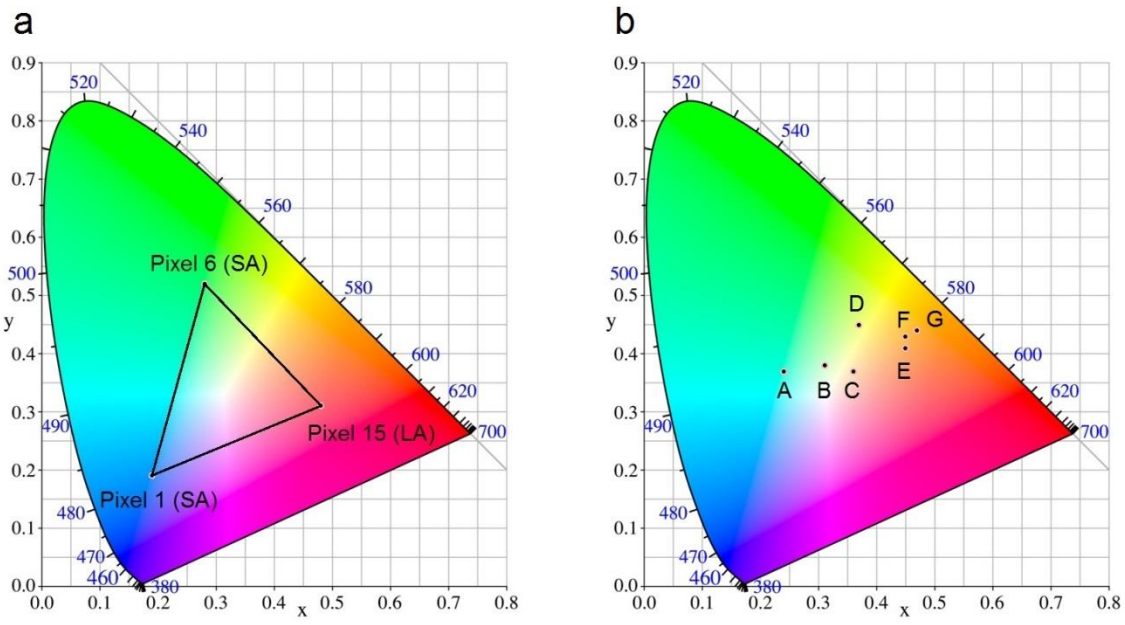

Figure 5.19, CIE1931 chromaticity diagram of pixels. (**a**) Three typical CIE1931 colour coordinates of dual-colour pixels, which were pixel 1 at short-arm transmission, pixel 6 at short-arm transmission and pixel 15 at long-arm transmission. (**b**) CIE1931 colour coordinates of colour mixed arrays A-G.

5.5 Conclusion

A dual-colour filtering scheme using cross-shaped aperture arrays in aluminium thin film has been proposed and demonstrated. Due to the asymmetric nature of the cross-shaped apertures, one single structure is able to excite two distinct surface plasmon resonances according to the incident polarisation. The resonance of one arm of the cross-aperture does not affect that of the other, thus producing two colours. The pixels' colours can be tuned through varying the geometrical dimensions of the cross-apertures and array period. A colour palette consisting of pixels with different combinations of short-arm length and array period was fabricated and characterised. Increasing either the arm-length or array period resulted in a red-shift in transmission, which can be verified through the measured results of transmission spectra. A series of microscopic

patterns were made by using these dual-colour nano pixels to achieve colour exchanging or images switching. The colours of these pixels were quantified in the CIE1931 chromaticity diagram as well.

Chapter 6 – Future work

Abstract

This chapter discusses the future prospects of a new type of plasmonic colour pixels and its possible application in achieving a 4-frame animation display. Each frame can be selected by a different combination of wavelength and polarisation of incident light. However, this part of work is only at the conceptual stage and further improvements are still needed.

6.1 Introduction

The experimental investigations shown in this thesis have demonstrated the unique optical properties of metallic nanovoid structures and their applications in molecular sensing and colour filtering. For the applications of colour pixels as shown in **Chapter 5**, one Al void cross-shaped pixel is able to exhibit two colours according to the incident polarisation, thus achieving 2-frame image switching. In order to push current research forward, the provision of a multi-frame (e.g. 4-frame) display is desirable, but this is impossible to achieve by changing polarisation alone. In this chapter, two void slot arrays with different dimensions and resonant wavelengths have been proposed as basic colour elements for the 4-frame animation display. Each void slot array only allows light transmission when both the incident polarisation and wavelength meet certain requirements. The light transmission will only occur when the incident polarisation is perpendicular to the slot and the incident wavelength lies in the transmission band of the slot. Such incident light can be generated by adding a polariser and a colour filter between the white light source and the sample.

6.2 Materials

The materials used in this Chapter refer to Section 2.2 in Chapter two.

6.3 Methods

6.3.1 Fabrication of Al void slot arrays

Figure 6.1 shows the fabrication process for Al void slot arrays by using one-step electron-beam lithography and reactive ion etching (RIE). Pyrex glass substrate was firstly modified with a 100 nm aluminium thin-film. (For procedures of cleaning and metallization refer to **Sections 2.3.3.1**and **2.3.3.2** respectively) The sample was then spin coated with a diluted ZEP520A positive e-beam resist (2 parts ZEP with 1 part anisole) at 3000 rpm spinning speed, to yield a resist thickness of ~250 nm, (**Fig.6.1.1**) Slot patterns were generated in the resist layer after e-beam exposure and development, (**Fig.6.1.2**). The exposure dose was 1000 μC/cm^2 and VRU was set to 6. (For procedures of resist coating, e-beam lithography and resist development refer to **Sections 2.3.3.4**, **2.3.3.5** and **2.3.3.6** respectively.) Then the sample was plasma etched by using $SiCl_4$ gas, thus transferring the slot patterns from the resist layer to the Al layer. After etching, the remaining resist was removed by rinsing the sample at 50°C in Microposit remover 1165 for 30 minutes (**Fig.6.1.3**).

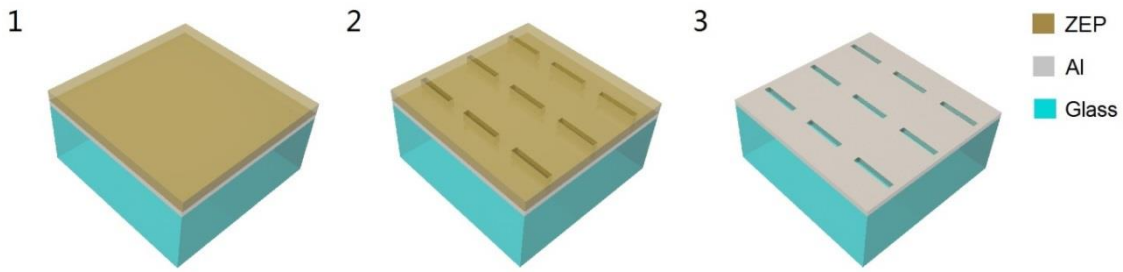

Figure 6.1, Fabrication of Al void slot arrays. (**1**) Sample preparation and resist coating. (**2**) Void slots were generated on the resist layer after ebeam exposure and development. (**3**) Void slots were transferred from the resist layer to Al thin-film by plasma reactive ion etching.

6.3.2 Animation pattern design

Four animation patterns including concentric-rings, concentric-squares, concentric-pentagons and a pendulum were designed in L-Edit (version 15) and fabricated for the demonstrations of the 4-frame animation. Each animation pattern contained 4 separate elements which corresponded to its 4 frames. The

void slots of correct dimensions and orientations were filled into each element, and the procedures for creating such patterns were similar to the dual-colour pattern design as shown in **Section 5.3.4** and the details of the animation patterns are presented in **Section 6.4.2**.

6.3.3 Animation capture by optical microscope

The 4-frame animations were captured by a ZEISS AXIO Imager A1 optical microscope. However, unlike the method used for capturing polarisation dependent images as shown in **Section 5.3.5**, the linear polariser was replaced by a filter wheel. One polariser and one filter were stacked together to change the white light to a polarised and single-coloured incident light. **Figure 6.2a** shows the schematic of an optical microscope for animation capturing and **Figure 6.2b** shows the cross-section view (upper) and top view (lower) of the filter wheel with polarisers and filters. Each polariser with the correct polarised direction was installed in one aperture (as shown in the figure, the arrows indicate the direction of polarisation) and one filter was placed on top of such a polariser. All the polarisers were fixed in positions and orientations, but the sequences of the filters can be changed to produce different animations. Aperture I was the first polariser and filter used and this was placed directly on top of the incident light. The filter-wheel was then rotated manually following the sequence from position I to position IV. It took ~2 seconds to move from one filter to the next. The objective lens chosen was 50X with NA 0.5. A CCD camera was used to take the animations and its frame rate was set to 1/2 Hz in accordance with the frequency of filter rotation. The capture time for each frame was 50 ms.

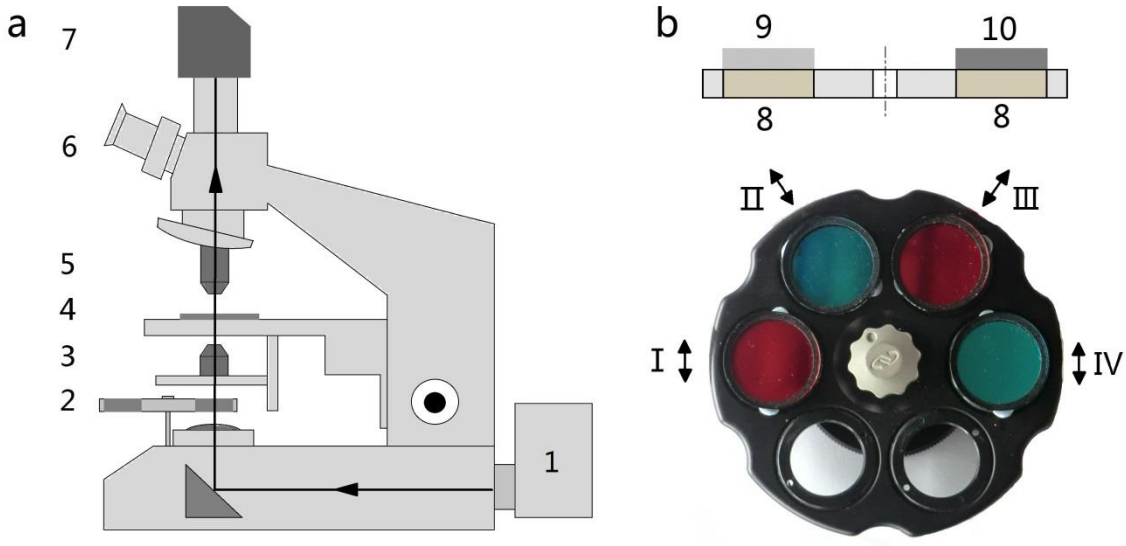

Figure 6.2, Optical system used for the animation capture. (**a**) Schematic of microscope, (1) Incident white light source. (2) Filter wheel. (3) Condenser lens. (4) Test sample clamped on the moveable stage. (5) Objective lens. (6) Eyepiece. (7) A CCD camera attached on top of the microscope. The black arrow line indicates the optical path of the incident and transmission light. (**b**) Schematic of the filter wheel from cross-section view (upper) and real image of the filter wheel from top view (lower). (8) Linear polariser. (9) Laser-line filter, CWL 635 nm-FWHM 10 nm. (10) Laser-line filter, CWL 488 nm-FWHM 10 nm. The position of each polariser-filter set is labelled by the Roman numeral from I to IV and the arrow beside each aperture indicates the polarisation direction. Only the filters can be seen in the top view of the filter wheel and the polariser was installed underneath each filter.

6.4 Results and discussion

6.4.1 Optical characterisation

By using the fabrication method presented above, two Al void slot arrays with a square-lattice were fabricated. **Figure 6.3** shows the SEM images of two such arrays in a 100 nm aluminium thin-film. The geometrical dimensions for array A were 200 nm in slot length, 32 nm in slot width and 310 nm in array period, and geometrical dimensions for array B were 300 nm in slot length, 32 nm in slot width and 410 nm in array period. As can be seen, the slot orientations of these two test arrays were kept the same.

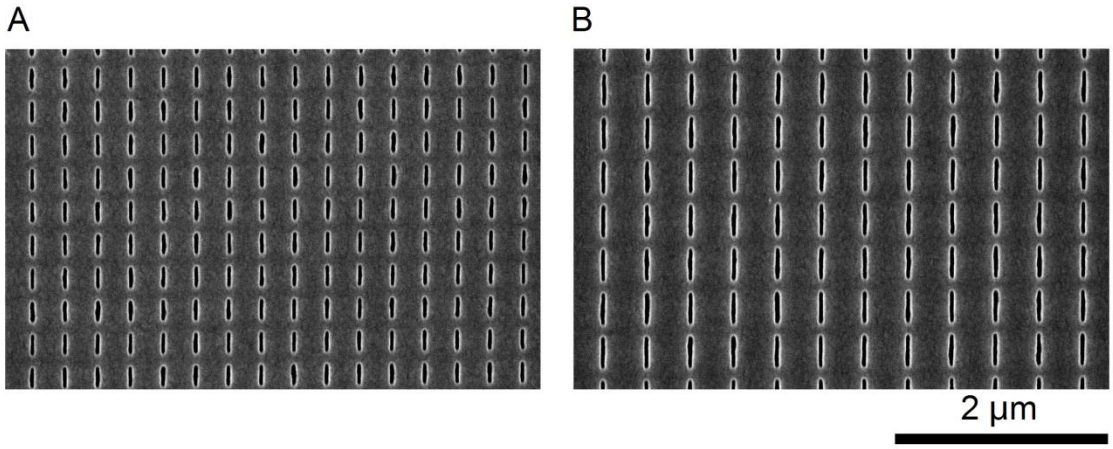

Figure 6.3, SEM images of Al void slot arrays A and B. The slots in array A had the length of 200 nm and period of 310 nm. The slots in array B had the length of 300 nm and period of 410 nm. The slot width of both arrays was 30 nm.

Figure 6.4 shows the optical images of arrays A and B, and the images in each column were captured under different incident conditions. For all the columns, the top ones represent the optical transmission images of array A and the bottom ones represent the optical transmission images of array B. The images in **Figure 6.4 (a)** were captured under polarised white light illumination. The incident polarisation was perpendicular to the slots, thus allowing light transmission through both arrays. Such a condition was termed as "polarisation on". The transmission bands of arrays A and B lie in red and blue range respectively. The images in **Figure 6.4 (b)** were captured under polarised white light illumination as well, but the incident polarisation was parallel to the slots, thus prohibiting light transmission. Such a condition was termed as "polarisation off". However, some shadows appeared which were probably due to the imperfection in structural shape, thus causing the weak transmissions. The images in **Figure 6.4 (c)** were captured under red light illumination in the "polarisation on" condition. A filter (CWL 635 nm, FWHM 10 nm) was used to generate the red incident light. Although the incident polarisation satisfied the condition for light transmission, the red incident light can be only transmitted through array A and was blocked by array B, because of the different transmission bands of these two arrays. **Figure 6.4 (d)** shows the optical images under red light illumination in the "polarisation off" condition, therefore, both arrays were "turned off", and no colours were transmitted. **Figure 6.4 (e)** and **Figure 6.4 (f)** show the optical images under blue light illumination (a CWL 488 nm-FWHM 10 nm filter was used to generate blue incident light) in the

polarisation “on” and “off” conditions respectively. In similar fashion as to when red incident light was used and array A allowed red transmission in the “polarisation on” condition, so too, when blue incident light was used, array B allowed transmission in the “polarisation on” condition. However, a faint shadow can be seen in array A at this time. This is largely due to the transmission overlap between these two arrays at “blue” range.

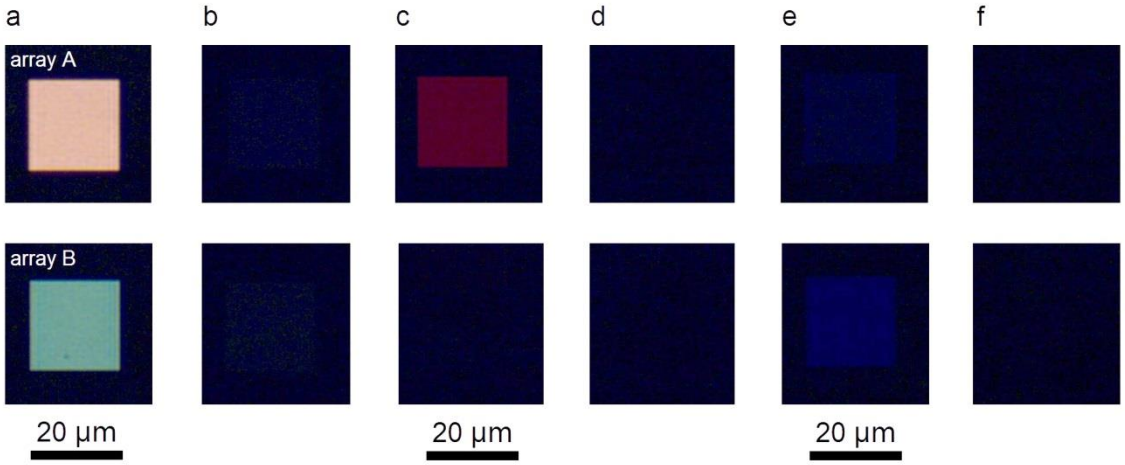

Figure 6.4, Optical transmission images of test arrays A and B. (**a**) Incident white light was polarised perpendicular to the slots and no filters were added. (**b**) Incident white light was polarised parallel to the slots and no filters were added. (**c**) Incident red light was polarised perpendicular to the slots. (**d**) Incident red light was polarised parallel to the slots. (**e**) Incident blue light was polarised perpendicular to the slots. (**f**) Incident blue light was polarised parallel to the slots. The size of both arrays was 20 µm in width.

6.4.2 Animations in 4-frame

The optical characterisations shown above have demonstrated that the light transmission through such “Reddish” slots (array A) and “Bluish” slots (array B) can be selectively turned “on” and “off” with proper control of incident polarisation and wavelength. Two incident wavelengths (CWL: 635 nm or 488 nm) and two polarisation states (perpendicular or parallel to the slot) result in four combinations, leading to four incident conditions. By appropriate animation design, each incident condition can be applied to display one single frame and block out the other three frames, thus achieving 4-frame animation by changing the incident condition in a programmed sequence.

Figure 6.5 shows the four animation patterns and the corresponding optical images of each frame. Taking animation **a** as an example, the design was shown in **Figure 6.5 (a)**. The numbers marked in the design indicate each frame. The first frame is a 50 μm diameter circle which is comprised of the "reddish" slots (array A) with the slot orientation along the y-axis. The second frame is a 18 μm width ring (inner diameter 92 μm, outer diameter 128 μm) which is comprised of the "bluish" slots (array B) with the slot orientation along the x-axis. The third frame is a 18 μm width ring (inner diameter 169 μm, outer diameter 205 μm) which is comprised of the "reddish" slots (array A) with the slot orientation along the x-axis. The fourth frame is of the outermost ring with a ring width of 18 μm (inner diameter 245 μm, outer diameter 281 μm) and which is comprised of the "bluish" slots (array B) with the slot orientation along the x-axis. The distance between two adjacent elements is 20 μm. Correspondingly, the incident condition for the 1st frame is red incident light polarised along the x-axis; for the 2nd frame it is blue incident light polarised along the y-axis; for the 3rd frame it is red incident light polarised along the x-axis; and for the 4th frame it is blue incident light polarised along the y-axis. **Figures 6.5 (a1)** - **(a4)** show the optical images of frames 1- 4. However, as mentioned before, because of the weak transmission of the "reddish" slot at the "blue" range, the shadow of frame 3 can be seen in the optical image of frame 2 (**Fig.6.5 (a2)**), and the shadow of frame 1 can be seen in the optical image of frame 4 (**Fig.6.5 (a4)**).

Similarly, the pattern of the concentric-squares (animation B), concentric-pentagons (animation C), and the pendulum (animation D) are shown in **Figures 6.5 (b)**, **6.5 (c)**, and **6.5 (d)** respectively. For each pattern, the dimensions and orientations of the nano slots in each frame and the corresponding incident light conditions were the same as that of animation **a**. The corresponding optical images of each frame are shown in **Figures 6.5 (b1)** – **(b4)**, **6.5 (c1)** – **(c4)**, and **6.5 (d1)** – **(d4)**. For the animation pattern **d**, the width of the pendulum arm is 18 μm and the diameters of the two circles are 45 μm and 70 μm.

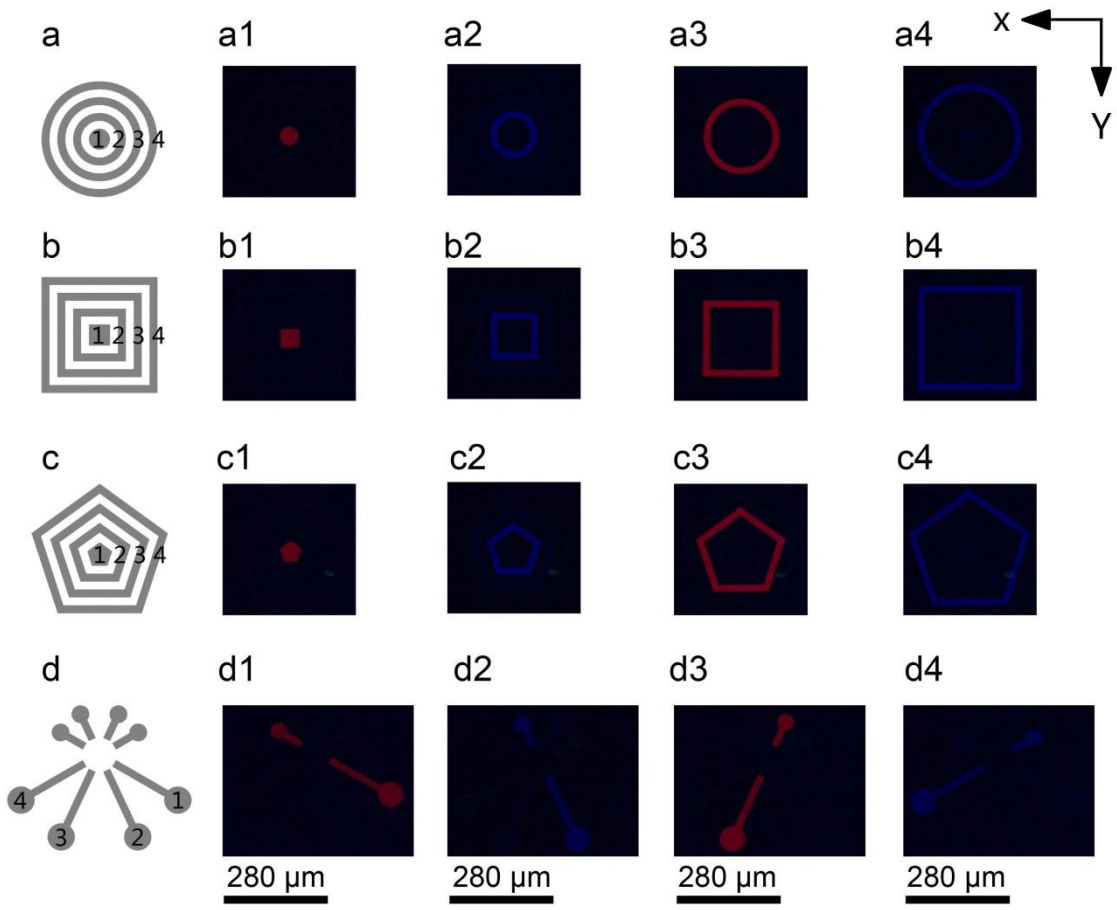

Figure 6.5, Four animation patterns and their corresponding optical images. (**a**) Animation pattern **a**-concentric rings. (**a1**)-(**a4**) Optical images of frames 1-4 of animation **a**. (**b**) Animation pattern **b**-concentric squares. (**b1**)-(**b4**) Optical images of frames 1-4 of animation **b**. (**c**) Animation pattern **c**-concentric-pentagons. (**c1**)-(**c4**) Optical images of frames 1-4 of animation **c**. (**d**) Animation pattern **d**-pendulum. (**d1**)-(**d4**) Optical images of frames 1-4 of animation **d**. The orientations of x- and y- axes are shown in the top right.

6.5 Conclusion

The void nanoslot structure exhibits high selectivity of wavelength and polarisation. In order to get optical transmission through the slot, two conditions must be satisfied, the first one is that the incident wavelength lies in the transmission band of the slot, and the second is that the incident polarisation keep perpendicular to the slot. By appropriate choosing of the incident conditions a 4-frame animation can be achieved. This chapter shows the fabrication of void nanoslot arrays by using electron beam lithography and reactive ion etching. Two void nanoslot arrays as basic “reddish” and “bluish” pixel elements were fabricated and characterised, and the optical images of

several animations based on these basic pixel elements were presented. Nevertheless, it has to be pointed out that the demonstrations of 4-frame animations are still at an initial stage, with the optical transmissions of such nanoslots still being impure. Further improvements can concentrate on increasing the quality-factor and the transmission efficiency of the pixels.

References

1. Maier, S.A., *Plasmonics: fundamentals and applications*. 2007: Springer Science & Business Media.
2. Etchegoin, P.G., E. Le Ru, and M. Meyer, *An analytic model for the optical properties of gold.* The Journal of chemical physics, 2006. **125**(16): p. 164705.
3. Cooper, J.W., *Interaction of maxima in the absorption of soft x rays.* Physical Review Letters, 1964. **13**(25): p. 762.
4. Lindquist, N.C., et al., *Engineering metallic nanostructures for plasmonics and nanophotonics.* Reports on progress in physics. Physical Society (Great Britain), 2012. **75**(3): p. 036501.
5. Jackson, J.D. and J.D. Jackson, *Classical electrodynamics*. Vol. 3. 1962: Wiley New York etc.
6. Stratton, J.A., *Electromagnetic theory*. 2007: John Wiley & Sons.
7. Murray, W.A. and W.L. Barnes, *Plasmonic materials.* Advanced materials, 2007. **19**(22): p. 3771-3782.
8. Petryayeva, E. and U.J. Krull, *Localized surface plasmon resonance: Nanostructures, bioassays and biosensing—A review.* Analytica chimica acta, 2011. **706**(1): p. 8-24.
9. Homola, J., S.S. Yee, and G. Gauglitz, *Surface plasmon resonance sensors: review.* Sensors and Actuators B: Chemical, 1999. **54**(1): p. 3-15.
10. Homola, J., *Present and future of surface plasmon resonance biosensors.* Analytical and bioanalytical chemistry, 2003. **377**(3): p. 528-539.
11. Kelly, K.L., et al., *The Optical Properties of Metal Nanoparticles: The Influence of Size, Shape, and Dielectric Environment.* The Journal of Physical Chemistry B, 2003. **107**(3): p. 668-677.
12. Hutter, E. and J.H. Fendler, *Exploitation of localized surface plasmon resonance.* Advanced Materials, 2004. **16**(19): p. 1685-1706.
13. Haes, A.J. and R.P. Van Duyne, *A nanoscale optical biosensor: sensitivity and selectivity of an approach based on the localized surface plasmon resonance spectroscopy of triangular silver nanoparticles.* Journal of the American Chemical Society, 2002. **124**(35): p. 10596-10604.
14. Bakker, R.M., et al., *Enhanced localized fluorescence in plasmonic nanoantennae.* Applied Physics Letters, 2008. **92**(4): p. 043101.
15. Mayer, K.M. and J.H. Hafner, *Localized Surface Plasmon Resonance Sensors.* Chemical Reviews, 2011. **111**(6): p. 3828-3857.
16. Weiner, J., *The physics of light transmission through subwavelength apertures and aperture arrays.* Reports on Progress in Physics, 2009. **72**(6): p. 064401.
17. Hoa, X., A. Kirk, and M. Tabrizian, *Towards integrated and sensitive surface plasmon resonance biosensors: a review of recent progress.* Biosensors and Bioelectronics, 2007. **23**(2): p. 151-160.
18. Alleyne, C.J., et al., *Enhanced SPR sensitivity using periodic metallic structures.* Optics Express, 2007. **15**(13): p. 8163-8169.
19. Otto, A., *Excitation of nonradiative surface plasma waves in silver by the method of frustrated total reflection.* Zeitschrift für Physik, 1968. **216**(4): p. 398-410.
20. Graedel, T., *Corrosion mechanisms for silver exposed to the atmosphere.* Journal of the Electrochemical Society, 1992. **139**(7): p. 1963-1970.

21. Huang, T. and X.-H.N. Xu, *Synthesis and characterization of tunable rainbow colored colloidal silver nanoparticles using single-nanoparticle plasmonic microscopy and spectroscopy.* Journal of Materials Chemistry, 2010. **20**(44): p. 9867-9876.
22. Liebermann, T. and W. Knoll, *Surface-plasmon field-enhanced fluorescence spectroscopy.* Colloids and Surfaces A: Physicochemical and Engineering Aspects, 2000. **171**(1): p. 115-130.
23. Ray, K., M.H. Chowdhury, and J.R. Lakowicz, *Aluminum nanostructured films as substrates for enhanced fluorescence in the ultraviolet-blue spectral region.* Analytical chemistry, 2007. **79**(17): p. 6480-6487.
24. Dörfer, T., M. Schmitt, and J. Popp, *Deep-UV surface-enhanced Raman scattering.* Journal of Raman Spectroscopy, 2007. **38**(11): p. 1379-1382.
25. Chan, G.H., et al., *Localized surface plasmon resonance spectroscopy of triangular aluminum nanoparticles.* The Journal of Physical Chemistry C, 2008. **112**(36): p. 13958-13963.
26. Abb, M., et al., *All-optical control of a single plasmonic nanoantenna-ITO hybrid.* Nano letters, 2011. **11**(6): p. 2457-2463.
27. Li, S.Q., et al., *Infrared plasmonics with indium-tin-oxide nanorod arrays.* ACS nano, 2011. **5**(11): p. 9161-9170.
28. Naik, G.V., et al., *Demonstration of Al: ZnO as a plasmonic component for near-infrared metamaterials.* Proceedings of the National Academy of Sciences, 2012. **109**(23): p. 8834-8838.
29. West, P.R., et al., *Searching for better plasmonic materials.* Laser & Photonics Reviews, 2010. **4**(6): p. 795-808.
30. Naik, G.V., et al., *Titanium nitride as a plasmonic material for visible and near-infrared wavelengths.* Optical Materials Express, 2012. **2**(4): p. 478-489.
31. Boltasseva, A. and H.A. Atwater, *Low-loss plasmonic metamaterials.* Science, 2011.
32. Yan, H., et al., *Tunable infrared plasmonic devices using graphene/insulator stacks.* Nature Nanotechnology, 2012. **7**(5): p. 330-334.
33. Grigorenko, A., M. Polini, and K. Novoselov, *Graphene plasmonics.* Nature photonics, 2012. **6**(11): p. 749-758.
34. Bethe, H., *Theory of diffraction by small holes.* Physical Review, 1944. **66**(7-8): p. 163.
35. Ebbesen, T.W., et al., *Extraordinary optical transmission through sub-wavelength hole arrays.* Nature, 1998. **391**(6668): p. 667-669.
36. Liu, H. and P. Lalanne, *Microscopic theory of the extraordinary optical transmission.* Nature, 2008. **452**(7188): p. 728-731.
37. Pacifici, D., et al., *Universal optical transmission features in periodic and quasiperiodic hole arrays.* Optics Express, 2008. **16**(12): p. 9222-9238.
38. Rodrigo, S.G., *Extraordinary optical transmission*, in *Optical Properties of Nanostructured Metallic Systems*. 2012, Springer. p. 37-75.
39. Stéphane, C., *Nanostructure arrays in free-space: optical properties and applications.* Reports on Progress in Physics, 2014. **77**(12): p. 126402.
40. Martin-Moreno, L., et al., *Theory of extraordinary optical transmission through subwavelength hole arrays.* Physical review letters, 2001. **86**(6): p. 1114.
41. Genet, C. and T. Ebbesen, *Light in tiny holes.* Nature, 2007. **445**(7123): p. 39-46.

42. Koerkamp, K.K., et al., *Strong influence of hole shape on extraordinary transmission through periodic arrays of subwavelength holes.* Physical Review Letters, 2004. **92**(18): p. 183901.
43. Bonod, N., et al., *Resonant optical transmission through thin metallic films with and without holes.* Optics Express, 2003. **11**(5): p. 482-490.
44. Cao, Q. and P. Lalanne, *Negative role of surface plasmons in the transmission of metallic gratings with very narrow slits.* Physical Review Letters, 2002. **88**(5): p. 057403.
45. Barnes, W.L., et al., *Surface plasmon polaritons and their role in the enhanced transmission of light through periodic arrays of subwavelength holes in a metal film.* Physical review letters, 2004. **92**(10): p. 107401.
46. Rodrigo, S.G., et al., *Extraordinary optical transmission through hole arrays in optically thin metal films.* Optics letters, 2009. **34**(1): p. 4-6.
47. Khanikaev, A.B., et al., *One-way extraordinary optical transmission and nonreciprocal spoof plasmons.* Physical review letters, 2010. **105**(12): p. 126804.
48. Poujet, Y., J. Salvi, and F.I. Baida, *90% Extraordinary optical transmission in the visible range through annular aperture metallic arrays.* Optics letters, 2007. **32**(20): p. 2942-2944.
49. Baida, F. and D. Van Labeke, *Light transmission by subwavelength annular aperture arrays in metallic films.* Optics communications, 2002. **209**(1): p. 17-22.
50. Baida, F. and D. Van Labeke, *Three-dimensional structures for enhanced transmission through a metallic film: Annular aperture arrays.* Physical Review B, 2003. **67**(15): p. 155314.
51. Orbons, S.M., et al., *Extraordinary optical transmission with coaxial apertures.* Applied physics letters, 2007. **90**(25): p. 251107.
52. Baida, F.I., et al., *Subwavelength metallic coaxial waveguides in the optical range: Role of the plasmonic modes.* Physical Review B, 2006. **74**(20): p. 205419.
53. Haftel, M.I., C. Schlockermann, and G. Blumberg, *Role of cylindrical surface plasmons in enhanced transmission.* Applied physics letters, 2006. **88**(19): p. 193104.
54. Orbons, S., et al., *Dual resonance mechanisms facilitating enhanced optical transmission in coaxial waveguide arrays.* Optics letters, 2008. **33**(8): p. 821-823.
55. Ren, X.-F., et al., *Polarization properties of subwavelength hole arrays consisting of rectangular holes.* Applied Physics B, 2008. **91**(3-4): p. 601-604.
56. DiMaio, J.R. and J. Ballato, *Polarization-dependent transmission through subwavelength anisotropic aperture arrays.* Optics Express, 2006. **14**(6): p. 2380-2384.
57. Mary, A., et al., *Theory of light transmission through an array of rectangular holes.* Physical Review B, 2007. **76**(19): p. 195414.
58. Elliott, J., et al., *Polarization control of optical transmission of a periodic array of elliptical nanoholes in a metal film.* Optics letters, 2004. **29**(12): p. 1414-1416.
59. Gordon, R., et al., *Strong polarization in the optical transmission through elliptical nanohole arrays.* Physical review letters, 2004. **92**(3): p. 037401.
60. Strelniker, Y.M., *Theory of optical transmission through elliptical nanohole arrays.* Physical Review B, 2007. **76**(8): p. 085409.

61. Thio, T., et al., *Enhanced light transmission through a single subwavelength aperture*. Optics Letters, 2001. **26**(24): p. 1972-1974.
62. Li, Z.-B., et al., *Enhanced light transmission through a single subwavelength aperture in layered films consisting of metal and dielectric*. Optics Express, 2005. **13**(22): p. 9071-9077.
63. Garcia-Vidal, F., et al., *Multiple paths to enhance optical transmission through a single subwavelength slit*. Physical Review Letters, 2003. **90**(21): p. 213901.
64. Lezec, H.J., et al., *Beaming light from a subwavelength aperture*. Science, 2002. **297**(5582): p. 820-822.
65. Martin-Moreno, L., et al., *Theory of highly directional emission from a single subwavelength aperture surrounded by surface corrugations*. Physical Review Letters, 2003. **90**(16): p. 167401.
66. Turner, A., I. Karube, and G.S. Wilson, *Biosensors: fundamentals and applications*. 1987.
67. Banica, F.-G., *Chemical sensors and biosensors: fundamentals and applications*. 2012: John Wiley & Sons.
68. Lesuffleur, A., et al., *Periodic nanohole arrays with shape-enhanced plasmon resonance as real-time biosensors*. Applied Physics Letters, 2007. **90**(24): p. 243110.
69. Pang, L., et al., *Spectral sensitivity of two-dimensional nanohole array surface plasmon polariton resonance sensor*. Applied Physics Letters, 2007. **91**(12): p. 123112.
70. Yanik, A.A., et al., *Seeing protein monolayers with naked eye through plasmonic Fano resonances*. Proceedings of the National Academy of Sciences, 2011. **108**(29): p. 11784-11789.
71. Eftekhari, F., et al., *Nanoholes as nanochannels: flow-through plasmonic sensing*. Analytical chemistry, 2009. **81**(11): p. 4308-4311.
72. Brolo, A.G., et al., *Enhanced fluorescence from arrays of nanoholes in a gold film*. Journal of the American Chemical Society, 2005. **127**(42): p. 14936-14941.
73. Rigneault, H., et al., *Enhancement of single-molecule fluorescence detection in subwavelength apertures*. Physical review letters, 2005. **95**(11): p. 117401.
74. Cui, X., et al., *Enhanced fluorescence microscopic imaging by plasmonic nanostructures: from a 1D grating to a 2D nanohole array*. Advanced Functional Materials, 2010. **20**(6): p. 945-950.
75. Wenger, J., et al., *Single molecule fluorescence in rectangular nano-apertures*. Optics express, 2005. **13**(18): p. 7035-7044.
76. Yu, Q. and G. Golden, *Probing the protein orientation on charged self-assembled monolayers on gold nanohole arrays by SERS*. Langmuir, 2007. **23**(17): p. 8659-8662.
77. Yang, Z.-L., et al., *Tunable SERS from aluminium nanohole arrays in the ultraviolet region*. Chem. Commun., 2011. **47**(13): p. 3909-3911.
78. Anema, J.R., et al., *Enhanced Raman scattering from nanoholes in a copper film*. The Journal of Physical Chemistry C, 2008. **112**(44): p. 17051-17055.
79. Masson, J.-F., M.-P. Murray-Méthot, and L.S. Live, *Nanohole arrays in chemical analysis: manufacturing methods and applications*. Analyst, 2010. **135**(7): p. 1483-1489.

80. Chen, Q. and D.R. Cumming, *High transmission and low color cross-talk plasmonic color filters using triangular-lattice hole arrays in aluminum films*. Optics express, 2010. **18**(13): p. 14056-14062.
81. Liu, Y.J., et al., *Light-Driven Plasmonic Color Filters by Overlaying Photoresponsive Liquid Crystals on Gold Annular Aperture Arrays*. Advanced Materials, 2012. **24**(23): p. OP131-OP135.
82. Do, Y.S., et al., *Plasmonic Color Filter and its Fabrication for Large-Area Applications*. Advanced Optical Materials, 2013. **1**(2): p. 133-138.
83. Lee, J., et al., *Shape resonance omni-directional terahertz filters with near-unity transmittance*. Optics express, 2006. **14**(3): p. 1253-1259.
84. Lu, X., J. Han, and W. Zhang, *Resonant terahertz reflection of periodic arrays of subwavelength metallic rectangles*. Applied Physics Letters, 2008. **92**(12): p. 121103.
85. Taubner, T., et al., *Near-field microscopy through a SiC superlens*. Science, 2006. **313**(5793): p. 1595-1595.
86. Raman, C.V., *A new radiation*. Proceedings of the Indian Academy of Sciences - Section A, 1953. **37**(3): p. 333-341.
87. *Eine neue Erscheinung bei der Lichtzerstreuung in Krystallen*. Naturwissenschaften, 1928. **16**(28): p. 557-558.
88. Rasetti, F., *Raman effect in gases*. Nature, 1929. **123**: p. 3093.
89. Harris, D.C. and M.D. Bertolucci, *Symmetry and spectroscopy: an introduction to vibrational and electronic spectroscopy*. 1978: Courier Corporation.
90. Fleischmann, M., P.J. Hendra, and A. McQuillan, *Raman spectra of pyridine adsorbed at a silver electrode*. Chemical Physics Letters, 1974. **26**(2): p. 163-166.
91. Blackie, E.J., E.C.L. Ru, and P.G. Etchegoin, *Single-molecule surface-enhanced Raman spectroscopy of nonresonant molecules*. Journal of the American Chemical Society, 2009. **131**(40): p. 14466-14472.
92. Nie, S. and S.R. Emory, *Probing single molecules and single nanoparticles by surface-enhanced Raman scattering*. science, 1997. **275**(5303): p. 1102-1106.
93. Kneipp, K., et al., *Single molecule detection using surface-enhanced Raman scattering (SERS)*. Physical review letters, 1997. **78**(9): p. 1667.
94. Xu, H., et al., *Spectroscopy of single hemoglobin molecules by surface enhanced Raman scattering*. Physical review letters, 1999. **83**(21): p. 4357.
95. Le Ru, E., et al., *Surface enhanced Raman scattering enhancement factors: a comprehensive study*. The Journal of Physical Chemistry C, 2007. **111**(37): p. 13794-13803.
96. Yan, B., et al., *Engineered SERS substrates with multiscale signal enhancement: nanoparticle cluster arrays*. Acs Nano, 2009. **3**(5): p. 1190-1202.
97. Yamada, H., et al., *Charge-transfer band and SERS mechanism for the pyridine-Ag system*. Surface science, 1987. **182**(1): p. 269-286.
98. Gao, P., et al., *Surface-enhanced Raman scattering at gold electrodes: dependence on electrochemical pretreatment conditions and comparisons with silver*. Journal of electroanalytical chemistry and interfacial electrochemistry, 1987. **233**(1): p. 211-222.
99. Stewart, S. and P. Fredericks, *Surface-enhanced Raman spectroscopy of amino acids adsorbed on an electrochemically prepared silver surface*.

Spectrochimica Acta Part A: Molecular and Biomolecular Spectroscopy, 1999. **55**(7): p. 1641-1660.
100. Kudelski, A., *Raman studies of rhodamine 6G and crystal violet submonolayers on electrochemically roughened silver substrates: Do dye molecules adsorb preferentially on highly SERS-active sites?* Chemical Physics Letters, 2005. **414**(4): p. 271-275.
101. Wu, D.-Y., et al., *Electrochemical surface-enhanced Raman spectroscopy of nanostructures.* Chemical Society Reviews, 2008. **37**(5): p. 1025-1041.
102. Felidj, N., et al., *Optimized surface-enhanced Raman scattering on gold nanoparticle arrays.* Applied Physics Letters, 2003. **82**(18): p. 3095-3097.
103. Wang, H.H., et al., *Highly raman-enhancing substrates based on silver nanoparticle arrays with tunable sub-10 nm gaps.* Advanced Materials, 2006. **18**(4): p. 491-495.
104. Gopinath, A., et al., *Deterministic aperiodic arrays of metal nanoparticles for surface-enhanced Raman scattering (SERS).* Optics Express, 2009. **17**(5): p. 3741-3753.
105. Brolo, A.G., et al., *Nanohole-enhanced Raman scattering.* Nano Letters, 2004. **4**(10): p. 2015-2018.
106. Lesuffleur, A., et al., *Apex-enhanced Raman spectroscopy using double-hole arrays in a gold film.* The Journal of Physical Chemistry C, 2007. **111**(6): p. 2347-2350.
107. Tian, Z.-Q., et al., *SERS from transition metals and excited by ultraviolet light*, in *Surface-Enhanced Raman Scattering*. 2006, Springer. p. 125-146.
108. Ren, B., et al., *Surface-enhanced Raman scattering in the ultraviolet spectral region: UV-SERS on rhodium and ruthenium electrodes.* Journal of the American Chemical Society, 2003. **125**(32): p. 9598-9599.
109. Huang, Z., et al., *Improved SERS performance from Au nanopillar arrays by abridging the pillar tip spacing by Ag sputtering.* Advanced Materials, 2010. **22**(37): p. 4136-4139.
110. Ruan, C., et al., *Controlled fabrication of nanopillar arrays as active substrates for surface-enhanced Raman spectroscopy.* Langmuir, 2007. **23**(10): p. 5757-5760.
111. Schmidt, M.S., J. Hübner, and A. Boisen, *Large area fabrication of leaning silicon nanopillars for surface enhanced Raman spectroscopy.* Advanced Materials, 2012. **24**(10): p. OP11-OP18.
112. He, Y., et al., *Silicon nanowires-based highly-efficient SERS-active platform for ultrasensitive DNA detection.* Nano Today, 2011. **6**(2): p. 122-130.
113. Yoon, I., et al., *Single nanowire on a film as an efficient SERS-active platform.* Journal of the American Chemical Society, 2008. **131**(2): p. 758-762.
114. Wei, W., et al., *Surprisingly Long-Range Surface-Enhanced Raman Scattering (SERS) on Au-Ni Multisegmented Nanowires.* Angewandte Chemie International Edition, 2009. **48**(23): p. 4210-4212.
115. Yu, X., et al., *Tuning chemical enhancement of SERS by controlling the chemical reduction of graphene oxide nanosheets.* ACS nano, 2011. **5**(2): p. 952-958.
116. Zhang, Z., et al., *A facile one-pot method to high-quality Ag-graphene composite nanosheets for efficient surface-enhanced Raman scattering.* Chemical Communications, 2011. **47**(22): p. 6440-6442.

117. Liu, Z., et al., *Graphene oxide based surface-enhanced Raman scattering probes for cancer cell imaging*. Physical Chemistry Chemical Physics, 2013. **15**(8): p. 2961-2966.
118. Yee, K., *based on FDTD calculations, Numerical solution of initial boundary value problemas involving Maxwell's equations in isotropic media*. IEEE Trans. on Antennas and Propagation, 1966. **17**: p. 585-589.
119. Taflove, A. and S.C. Hagness, *Computational electrodynamics*. 2005: Artech house.
120. Sullivan, D.M., *Electromagnetic simulation using the FDTD method*. 2013: John Wiley & Sons.
121. Solutions, L., *FDTD Solutions Manual Release 7.5*. Vancouver, BC, 2011.
122. Johnson, P.B. and R.-W. Christy, *Optical constants of the noble metals*. Physical Review B, 1972. **6**(12): p. 4370.
123. Palik, E.D., *Handbook of optical constants of solids*. Vol. 3. 1998: Academic press.
124. Pease, R., *Electron beam lithography*. Contemporary Physics, 1981. **22**(3): p. 265-290.
125. Herriott, D.R., *Electron beam lithography*. Journal of Vacuum Science & Technology, 1982. **20**(3): p. 781-785.
126. Brewer, G., *Electron-beam technology in microelectronic fabrication*. 2012: Elsevier.
127. Brodie, I. and J.J. Muray, *The physics of micro/nano-fabrication*. 2013: Springer Science & Business Media.
128. Haller, I., M. Hatzakis, and R. Srinivasan, *High-resolution positive resists for electron-beam exposure*. IBM Journal of Research and Development, 1968. **12**(3): p. 251-256.
129. Geyer, W., et al., *Electron-induced crosslinking of aromatic self-assembled monolayers: Negative resists for nanolithography*. Applied Physics Letters, 1999. **75**(16): p. 2401-2403.
130. Mohammad, M., et al., *Fundamentals of Electron Beam Exposure and Development*, in *Nanofabrication*, M. Stepanova and S. Dew, Editors. 2012, Springer Vienna. p. 11-41.
131. Oehrlein, G.S., *Reactive-Ion Etching*. Physics Today, 2008. **39**(10): p. 26-33.
132. Madou, M.J., *Fundamentals of microfabrication: the science of miniaturization*. 2002: CRC press.
133. Kastenmeier, B., et al., *Chemical dry etching of silicon nitride and silicon dioxide using CF4/O2/N2 gas mixtures*. Journal of Vacuum Science & Technology A, 1996. **14**(5): p. 2802-2813.
134. Furuhata, N., et al., *Cl 2 chemical dry etching of GaAs under high vacuum conditions—crystallographic etching and its mechanism*. Journal of electronic materials, 1990. **19**(2): p. 201-208.
135. Kern, W., *Thin film processes II*. Vol. 2. 2012: Academic press.
136. Chance, B., *Rapid and sensitive spectrophotometry. III. A double beam apparatus*. Review of Scientific Instruments, 1951. **22**(8): p. 634-638.
137. Andersen, M. and R. Muggli, *Microscopical techniques in the use of the molecular optics laser examiner Raman microprobe*. Analytical Chemistry, 1981. **53**(12): p. 1772-1777.
138. Bowley, H.J., et al., *Practical raman spectroscopy*. 2012: Springer Science & Business Media.
139. *www.dowcorning.com/content/publishedlit/11-1547e-01.pdf*.
140. *www.zeonchemicals.com/pdfs/ZEP520A.pdf*.

141. Ulman, A., *Formation and structure of self-assembled monolayers.* Chemical reviews, 1996. **96**(4): p. 1533-1554.
142. Bain, C.D. and G.M. Whitesides, *Molecular-level control over surface order in self-assembled monolayer films of thiols on gold.* Science, 1988. **240**(4848): p. 62-63.
143. Li, W.-D. and S.Y. Chou, *Solar-blind deep-UV band-pass filter (250-350 nm) consisting of a metal nano-grid fabricated by nanoimprint lithography.* Optics express, 2010. **18**(2): p. 931-937.
144. Nishijima, Y., et al., *Selective enhancement of infrared absorption with metal hole arrays.* Optical Materials Express, 2012. **2**(10): p. 1367-1377.
145. van Hulst, N.F., *Plasmonics: sorting colours.* Nature Photonics, 2008. **2**(3): p. 139-140.
146. Menezes, J.W., et al., *Large-Area fabrication of periodic arrays of nanoholes in metal films and their application in biosensing and plasmonic-Enhanced photovoltaics.* Advanced Functional Materials, 2010. **20**(22): p. 3918-3924.
147. Atwater, H.A. and A. Polman, *Plasmonics for improved photovoltaic devices.* Nature materials, 2010. **9**(3): p. 205-213.
148. Han, S.E. and G. Chen, *Optical absorption enhancement in silicon nanohole arrays for solar photovoltaics.* Nano letters, 2010. **10**(3): p. 1012-1015.
149. Henzie, J., M.H. Lee, and T.W. Odom, *Multiscale patterning of plasmonic metamaterials.* Nature nanotechnology, 2007. **2**(9): p. 549-554.
150. Luk'yanchuk, B., et al., *The Fano resonance in plasmonic nanostructures and metamaterials.* Nature materials, 2010. **9**(9): p. 707-715.
151. Zhang, S., et al., *Experimental demonstration of near-infrared negative-index metamaterials.* Physical review letters, 2005. **95**(13): p. 137404.
152. Yu, Q., et al., *Inverted size-dependence of surface-enhanced Raman scattering on gold nanohole and nanodisk arrays.* Nano letters, 2008. **8**(7): p. 1923-1928.
153. Reilly, T.H., et al., *Quantitative evaluation of plasmon enhanced Raman scattering from nanoaperture arrays.* Journal of Physical Chemistry C, 2007. **111**(4): p. 1689-1694.
154. Bahns, J.T., et al., *High-Fidelity Nano-Hole-Enhanced Raman Spectroscopy.* The Journal of Physical Chemistry C, 2009. **113**(26): p. 11190-11197.
155. Li, Z., A.W. Clark, and J.M. Cooper, *Annular nanoplasmonic void arrays as tunable surface enhanced Raman spectroscopy substrates.* Applied Physics Letters, 2014. **105**(3): p. 033115.
156. Najiminaini, M., et al., *Experimental and numerical analysis on the optical resonance transmission properties of nano-hole arrays.* Optics express, 2010. **18**(21): p. 22255-22270.
157. Murray-Méthot, M.-P., M. Ratel, and J.-F. Masson, *Optical properties of Au, Ag, and bimetallic Au on Ag nanohole arrays.* The Journal of Physical Chemistry C, 2010. **114**(18): p. 8268-8275.
158. Moskovits, M., *Surface-enhanced Raman spectroscopy: a brief retrospective.* Journal of Raman Spectroscopy, 2005. **36**(6-7): p. 485-496.
159. Li, J.F., et al., *Shell-isolated nanoparticle-enhanced Raman spectroscopy.* nature, 2010. **464**(7287): p. 392-395.
160. Wustholz, K.L., et al., *Structure− activity relationships in gold nanoparticle dimers and trimers for surface-enhanced Raman*

spectroscopy. Journal of the American Chemical Society, 2010. **132**(31): p. 10903-10910.
161. Wang, H., C.S. Levin, and N.J. Halas, *Nanosphere arrays with controlled sub-10-nm gaps as surface-enhanced Raman spectroscopy substrates*. Journal of the American Chemical Society, 2005. **127**(43): p. 14992-14993.
162. Orendorff, C.J., et al., *Surface-enhanced Raman spectroscopy of self-assembled monolayers: sandwich architecture and nanoparticle shape dependence*. Analytical chemistry, 2005. **77**(10): p. 3261-3266.
163. Chen, T., et al., *Hotspot-induced transformation of surface-enhanced Raman scattering fingerprints*. Acs Nano, 2010. **4**(6): p. 3087-3094.
164. Clark, A.W., et al., *Plasmonic split-ring resonators as dichroic nanophotonic DNA biosensors*. Journal of the American Chemical Society, 2009. **131**(48): p. 17615-17619.
165. Cubukcu, E., et al., *Split ring resonator sensors for infrared detection of single molecular monolayers*. Applied Physics Letters, 2009. **95**(4): p. 043113.
166. Lahiri, B., et al., *Asymmetric split ring resonators for optical sensing of organic materials*. Optics express, 2009. **17**(2): p. 1107-1115.
167. Hatab, N.A., et al., *Free-standing optical gold bowtie nanoantenna with variable gap size for enhanced Raman spectroscopy*. Nano letters, 2010. **10**(12): p. 4952-4955.
168. Grand, J., et al., *Role of localized surface plasmons in surface-enhanced Raman scattering of shape-controlled metallic particles in regular arrays*. Physical Review B, 2005. **72**(3): p. 033407.
169. Lissberger, P. and W. Wilcock, *Properties of all-dielectric interference filters. II. Filters in parallel beams of light incident obliquely and in convergent beams*. JOSA, 1959. **49**(2): p. 126-128.
170. Brault, A.T., W.A. Light, and T.W. Martin, *Method for making a solid-state color imaging device having an integral color filter and the device*. 1978, Google Patents.
171. Koo, H.-S., M. Chen, and P.-C. Pan, *LCD-based color filter films fabricated by a pigment-based colorant photo resist inks and printing technology*. Thin solid films, 2006. **515**(3): p. 896-901.
172. Do Kim, Y., et al., *The synthesis and application of thermally stable dyes for ink-jet printed LCD color filters*. Dyes and pigments, 2009. **81**(1): p. 45-52.
173. Swanson, S.A., et al., *Stable and efficient fluorescent red and green dyes for external and internal conversion of blue OLED emission*. Chemistry of materials, 2003. **15**(12): p. 2305-2312.
174. Sabnis, R.W., *Color filter technology for liquid crystal displays*. Displays, 1999. **20**(3): p. 119-129.
175. Parulski, K., *Color filters and processing alternatives for one-chip cameras*. Electron Devices, IEEE Transactions on, 1985. **32**(8): p. 1381-1389.
176. Smith, S., et al. *A single-chip 306/spl times/244-pixel CMOS NTSC video camera*. in *Solid-State Circuits Conference, 1998. Digest of Technical Papers. 1998 IEEE International*. 1998. IEEE.
177. Kumar, K., et al., *Printing colour at the optical diffraction limit*. Nature Nanotechnology, 2012. **7**(9): p. 557-561.
178. Inoue, D., et al., *Polarization independent visible color filter comprising an aluminum film with surface-plasmon enhanced transmission through a*

subwavelength array of holes. Applied Physics Letters, 2011. **98**(9): p. 093113.
179. Yokogawa, S., S.P. Burgos, and H.A. Atwater, *Plasmonic color filters for CMOS image sensor applications*. Nano Letters, 2012. **12**(8): p. 4349-4354.
180. Alfalou, A. and C. Brosseau, *Dual encryption scheme of images using polarized light*. Optics letters, 2010. **35**(13): p. 2185-2187.
181. Tyo, J.S., et al., *Review of passive imaging polarimetry for remote sensing applications*. Applied optics, 2006. **45**(22): p. 5453-5469.
182. Laux, E., et al., *Plasmonic photon sorters for spectral and polarimetric imaging*. Nature Photonics, 2008. **2**(3): p. 161-164.
183. Li, Z., A.W. Clark, and J.M. Cooper, *Dual Color Plasmonic Pixels Create a Polarization Controlled Nano Color Palette*. ACS Nano, 2015.
184. Olson, J., et al., *Vivid, full-color aluminum plasmonic pixels*. Proceedings of the National Academy of Sciences, 2014. **111**(40): p. 14348-14353.
185. Shrestha, V.R., et al., *Aluminum plasmonics based highly transmissive polarization-independent subtractive color filters exploiting a nanopatch array*. Nano letters, 2014. **14**(11): p. 6672-6678.
186. Ellenbogen, T., K. Seo, and K.B. Crozier, *Chromatic plasmonic polarizers for active visible color filtering and polarimetry*. Nano letters, 2012. **12**(2): p. 1026-1031.
187. Xie, Y., et al., *Transmission of light through slit apertures in metallic films*. Optics express, 2004. **12**(25): p. 6106-6121.